Experimentally probing the effect of electronic structure on the thermoelectric properties of molecular junctions

by

Won Ho Jeong

A dissertation submitted in partial fulfillment
of the requirements for the degree of
Doctor of Philosophy
(Mechanical Engineering)
in the University of Michigan
2014

Doctoral Committee:

Associate Professor Pramod Sangi Reddy, Chair
Associate Professor Vikram Gavini
Professor Edgar Meyhofer
Assistant Professor Anish Tuteja

Dedication

To

Those who devoted themselves to Korean Independence and Democracy

And

My loving family (wife Jiyeon, daughter Ashley, brother Ilho and parents)

Acknowledgements

During last 6 years, I have gone through many things. Achieving the final goal of this research was really painful: it requires for me to spend a huge amount of time and effort, and I have experienced myriad trial and errors until realizing a desired platform. But, I am pleased that in the long run I completed my PhD degree with making some progress. I have many people to show my sincere appreciation. Without them, it might not be possible for this thesis to come out.

First of all, I thank to my advisor, Prof. Pramod Reddy. When I initially joined his group in January 2009, I was a novice in the field of molecular thermoelectrics. I studied liquid rocket injectors during my master degree, and I worked for Hyundai Motor Company afterward. Regardless of my background, he recruited me among others and has kept supporting me intellectually and financially. He is a great mentor as well as careful experimentalist with a strong theoretical base, thus I found myself having been upgraded during my PhD degree.

I thank to my dissertation committee members, Prof. Meyhofer, Prof. Gavini and Prof. Tuteja. They helped me to improve my thesis and have approved of all my work, thus I have been encouraged by them. It was my pleasure that they were my dissertation committee members. Specifically, I appreciate Prof. Gavini helping me initially join Prof. Reddy's group.

I thank to my collaborators, Dr. Kyeongtae Kim and Dr. Youngsang Kim. Without their special expertise and effort, the final goal of this research might not be accomplished before I graduate. I believe that their landing to our laboratory was a game-changing moment to me.

I thank to my laboratory members, Aaron, Seid, Woochul, Bai, Yashar, Dakotah, Anthony, Longji and Ahmet. My laboratory life was pleasant, and I have learned many things by interacting with them.

I also thank to one of my closest friends in Ann Arbor, Insu Lee and his family. They are always on my family's side and have kindly helped me and my family whenever we have a hard time.

Last but not least, I thank to my loving family, wife Jiyeon, daughter Ashley, brother Ilho and parents. They always show me their endless trust and love. Specifically, I appreciate Jiyeon continuously supporting me during my PhD degree. She has gone through a hard time with me for last 6 years. I largely attributed the completion of my PhD degree to her.

As a closing remark, I'd like to tell those who are disappointed with themselves at this point "It ain't over 'til it's over (by Yogi Berra, a former New York Yankees' legendary catcher)." Although you strongly feel you are trailing by 10–0 now, that is not the whole story. I believe that every person has a game-changing moment in her/his life. Focus more, grab the chance and keep going. The final result will be different. Why? It ain't over 'til it's over.

Table of Contents

List of figures

List of tables

List of appendices

Abstract

Experimentally probing the effect of electronic structure on the thermoelectric properties of molecular junctions

by

Won Ho Jeong

Chair: Pramod Sangi Reddy

Direct conversion of heat into electricity via thermoelectric effects is extremely attractive as it has significant potential for waste heat recovery and for improving the efficiency of various heat engines that are widely used. It has been suggested that ideal thermoelectric energy conversion reaching the Carnot limit can be achieved if charge transmission characteristics of materials at the chemical potential are well approximated by a Dirac-delta function. Achieving such charge transmission characteristics is extremely difficult in bulk inorganic materials but is readily possible in zero-dimensional molecular junctions.

To better understand thermoelectric properties of molecular junctions, I developed (in collaboration with others) novel tools for studying thermal and thermoelectric phenomena at the nanoscale. Specifically, I first established ultra-high vacuum scanning thermal microscopy (UHV-SThM) that is capable of quantitatively mapping temperature fields with ~15 mK temperature resolution and ~10 nm spatial resolution. In this technique, a custom nanofabricated atomic force microscopy (AFM) probe, with a nanoscale Au-Cr thermocouple integrated into the probe tip, is used to study temperature information of

nanoscale devices. Operation in an UHV environment eliminates parasitic heat transfer between the tip and the sample enabling quantitative measurements of temperature fields on metallic and dielectric surfaces with excellent spatial resolution.

By leveraging UHV-SThM, I performed quantitative studies of heat dissipation (Joule heating) in gold nanowires during electromigration. The experimental results unambiguously illustrated that electromigration begins at temperatures significantly lower than the melting temperature of gold. Further, it was shown that during electromigration voids predominantly accumulate at the cathode resulting in asymmetric temperature distributions, which provides novel insights into the microscopic details of hot spot evolution during electromigration.

Finally, I investigated electrostatic control of the thermoelectric properties of molecular junctions, which is key to extremely efficient thermoelectric energy conversion. This was accomplished by carefully designing and nanofabricating three-terminal devices that feature temperature gradients exceeding 10^9 K/m across nanogaps. Using these devices I studied thermoelectric effects in Au-biphenyl-4,4'-dithiol-Au and Au-fullerene-Au junctions and demonstrated that the Seebeck coefficient and electrical conductance of molecular junctions can be simultaneously increased by electrostatic control of charge transmission characteristics—for the first time ever. In particular, the studies of fullerene junctions show that thermoelectric properties can be dramatically enhanced when the dominant transport orbital is located close to the chemical potential illustrating the intimate relationship between the thermoelectric properties and charge transmission characteristics of molecular junctions. The novel three-terminal devices developed in this work are expected to enable systematic exploration of predictions that promise extremely efficient molecular-scale thermoelectric energy conversion.

Chapter 1

Introduction

1.1 Perspective

The goal of my research is to experimentally probe the relationship between the electronic structure and the thermoelectric properties of metal-organic molecule-metal junctions (MMMJs). It is now well known that charge transport properties of MMMJs, created by trapping organic molecules between metal electrodes, are strongly dependent on the chemical composition of electrodes and the electronic structure of organic molecules [1-5]. This results in novel properties that are specific to MMMJs, which are unlike those of either the metal electrodes or the organic molecules. Recent computational studies [6-8] suggest that it is possible to simultaneously achieve a large Seebeck coefficient and electrical conductance by appropriately positioning the molecular orbitals of a MMMJ with respect to the chemical potential E_F. If such effects are indeed realized, creating very efficient thermoelectric devices based on MMMJs become feasible. However, this hypothesis remains experimentally unproven until now primarily due to the lack of an appropriate experimental platform to examine these novel phenomena expected to arise in MMMJs. The work described in this thesis bridges this gap by developing novel experimental tools to test these interesting predictions.

The work presented here builds upon recent advancements towards experimentally probing charge transport in MMMJs. These advances include: 1) techniques to create MMMJs and study charge transport in them [1, 3-5, 9-12], 2) the establishment of

temperature differentials across MMMJs to study thermoelectric effects as demonstrated by Reddy *et al.* [13]. In this work, I developed a novel experimental platform that enables the tuning of the electronic structure of MMMJs along with studying their thermoelectric properties. This experimental platform enables—for the first time ever—direct probing of the dependence of the thermoelectric properties of MMMJs on their electronic structure. Using this platform along with other tools developed by me and collaborators [14], I performed challenging and important investigations to examine novel phenomena that arise in MMMJs. Such experimental studies will eventually enable not only the creation of novel cost-efficient organic molecule based thermoelectric devices but also technologies such as organic photovoltaics, organic electronics and molecular electronics where inorganic-organic interfaces play a key role.

1.2 Past work on probing charge transport in molecular junctions

Nanowire and nanotube junctions are being studied extensively due to their potential for technological applications in thermoelectric energy conversion [15-21], nanoelectronics [22-25] and other areas [26-32]. Analogous to nanowire and nanotube junctions, MMMJs hold significant potential for a wide range of technological applications such as molecular electronics and novel energy conversion devices. For example, MMMJs have been suggested to be ideal candidates for creating very efficient thermoelectric devices [6, 7, 33, 34]. However, their potential has not been systematically investigated due to experimental challenges.

Direct conversion of heat into electricity via thermoelectric effects has been attractive since 1950s due to its significant potential for waste heat recovery. The efficiency of thermoelectric energy conversion is dependent on the transport properties of the materials that consist of a system. Specifically, it is directly proportional to the thermoelectric

figure of merit ZT defined as $ZT = S^2 G_{elec} T / G_{th}$, where S is the Seebeck coefficient, G_{elec} is the electrical conductance, G_{th} is the thermal conductance of the materials and T is the absolute temperature, respectively [35] (higher ZT implies more efficient thermoelectric energy conversion). Although $ZT > 3$ is required for thermoelectric devices to be competitive with other conventional technologies, the state-of-the-art commercial materials have $ZT \sim 1$ at room temperature [35, 36]. Therefore, many research groups have aggressively pursued to achieve efficient thermoelectric energy conversion, and most of recent progress has been achieved by nanostructuring inorganic materials [37-40].

Theoretical studies have suggested various approaches to achieve $ZT > 3$. Some of these studies have shown that a large value of $S^2 G_{elec}$ can be achieved if charge transport occurs through a material with a sharp peak and/or a sharp gradient in its electronic density of states around the chemical potential E_F [15, 41, 42]. For example, Hicks *et al.* [15, 43] have suggested that it would be possible to achieve very efficient ($ZT >> 3$) thermoelectric energy conversion by using hetero-structured thin-film materials or nanowires that are designed to have a sharp peak in their electronic density of states around the chemical potential E_F. However, a sharp electronic density of states is very difficult to realize in bulk inorganic materials because of the continuous band of energy levels. In contrast to bulk inorganic materials, the electronic structure of MMMJs is related to the discrete molecular energy levels (Figure 1.1). Further, these energy levels can be tuned to have a sharp electronic density of states near the chemical potential E_F [33] by an appropriate choice of the organic molecules and/or the metal electrodes or by application of a gate voltage. In fact, previous theoretical studies [33] suggest that it may be possible to create very efficient thermoelectric devices based on MMMJs.

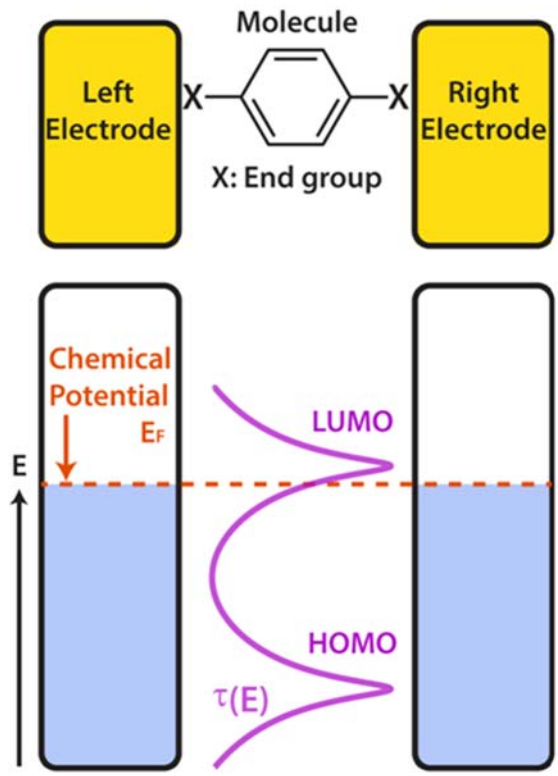

Figure 1.1: Schematic of the electronic structure of a MMMJ. The electronic structure of MMMJs shows distinct features of the discrete energy levels from that of bulk inorganic materials.

A more quantitative description of the electrical conductance and the Seebeck coefficient of molecular junctions can be obtained using the Landauer theory:

$$G_{\text{elec}} = \frac{2e^2}{h}\tau(E)\Big|_{E=E_F} \quad \text{and} \quad S = -\frac{\pi^2 k_B^2 T}{3|e|}\frac{\partial \ln(\tau(E))}{\partial E}\Big|_{E=E_F} \tag{1.1}$$

where $\tau(E)$ is the transmission that approximately represents the probability of an electron with energy E to be transmitted through a molecular junction, and e is the charge of an electron. Equation 1.1 implies that the electrical conductance G_{elec} and the Seebeck coefficient S depend on the magnitude and the derivative of the transmission at the chemical potential E_F, respectively. This fact is also described in Figure 1.2 that depicts the computed transmission and Seebeck coefficient for a Au-BDT-Au junction [8]. It can be seen from Figure 1.2 that when the chemical potential E_F is away from (shown by the

red line) the highest occupied molecular orbital (HOMO) and the lowest unoccupied molecular orbital (LUMO) levels, the magnitude and the derivative of the transmission at E_F are both small resulting in small values of G_{elec} and S. However, if the chemical potential E_F is close to (shown by the green line) the HOMO or the LUMO level, the magnitude and the derivative of the transmission at E_F can be simultaneously large resulting in large values of G_{elec} and S. Therefore, key to achieving a large value of S^2G_{elec} is to enhance both the magnitude and the derivative of the transmission at the chemical potential E_F. Since the transmission $\tau(E)$ is related to the available energy levels in MMMJs, a large magnitude of $\tau(E)$ implies a large electronic density of states at energy E. Further, a large derivative of $\tau(E)$ implies a rapid change in the electronic density of states at energy E. Therefore, key to obtaining a MMMJ with a large S^2G_{elec} is a sharp singularity in its electronic density of states in close proximity to the chemical potential E_F. If such a molecular junction, which has been predicted by computational studies [6, 7, 33], is experimentally realized it will lead to an extremely large value of S^2G_{elec}. Further, the thermal conductance of MMMJs is also expected to be very small due to a large mismatch in the vibrational spectra between the bulk metal electrodes (continuous vibrational density of states) and the organic molecules (discrete vibrational density of states) [44]. This mismatch leads to a small value of G_{th}, which is favorable for achieving a large value of ZT. If transport of charge and energy in MMMJs is understood and the ability to control charge and heat transport in these junctions is attained, it will be possible to create very efficient thermoelectric devices based on MMMJs. In this context an important question that naturally arises is: Can thermoelectric properties be tuned by actively controlling the electronic structure of MMMJs? Answering this important question is the main objective of this thesis.

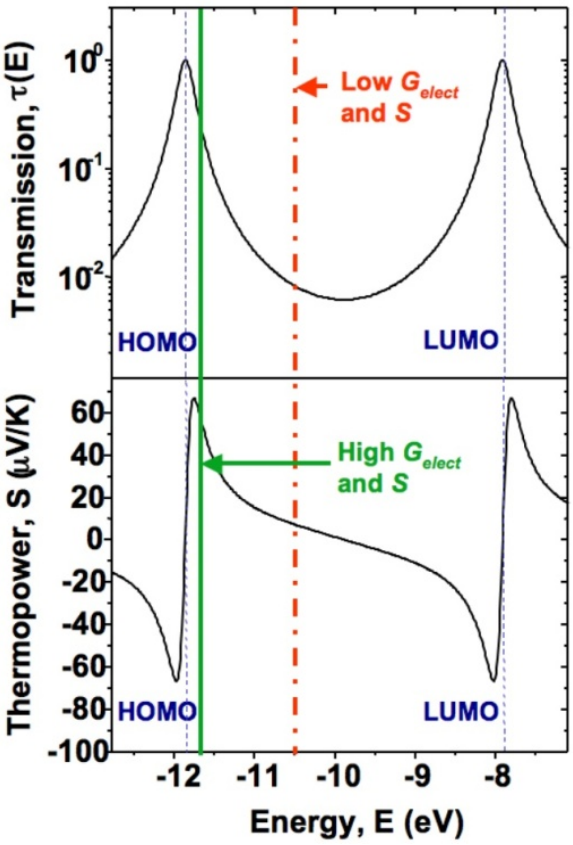

Figure 1.2: Computed transmission and Seebeck coefficient of a Au-BDT-Au junction plotted as a function of energy. The short dashed lines show the HOMO and the LUMO levels where the magnitude of the transmission is large. The red line represents the position of the chemical potential E_F in a scenario where E_F is far from the HOMO and the LUMO levels. The green line represents the position of E_F in a scenario where E_F is close to the HOMO level. (Figure reproduced with permission from Ref. 13.)

In recent years, multiple experimental platforms have been developed to create MMMJs, and pioneering experiments have been performed to understand charge and energy transport in molecular junctions. Some of these platforms are contact probe atomic force microscopy (CPAFM) [9, 45], scanning tunneling microscope break junction (STMBJ) [12, 46], mechanically controllable break junction (MCBJ) [10, 47] and electromigrated break junction (EBJ) [48-51].

Among these platforms, CPAFM, STMBJ and MCBJ enable two-terminal measurements of charge and energy transport in MMMJs. However, it is not possible to use any of these platforms to directly tune the energetic position of the molecular orbitals

of a MMMJ to study the relationship between the electronic structure of the molecular junction and its transport properties. In order to control the position of the molecular orbitals of a MMMJ, it is necessary to employ a device with a third terminal (a gate electrode) that is in close proximity to the molecular junction, such as that shown in Figure 1.3.

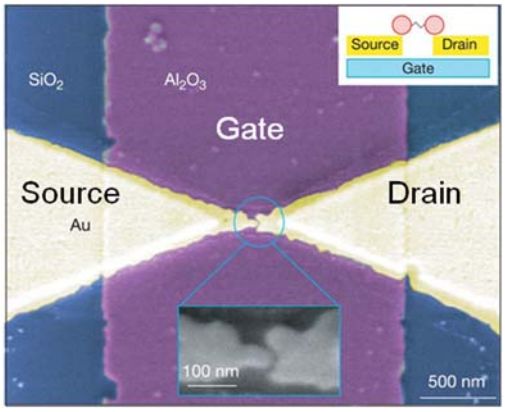

Figure 1.3: Molecular device with a third terminal (a gate electrode). One or a few molecules can be trapped between the source and drain electrodes, which are separated from the gate electrode via a thin Al_2O_3 layer. (Figure reproduced with permission from Ref. 1.)

Such a gate electrode can be used to control the electrostatic potential in a MMMJ by application of a gate voltage, which in turn determines the position of the molecular orbitals with respect to the chemical potential E_F. Figure 1.4 presents a schematic describing the effects of a gate voltage on the electronic structure of a MMMJ. It can be seen that application of a positive gate voltage shifts the LUMO level closer to the chemical potential E_F signifying the accumulation of negative charge in the MMMJ; whereas, application of a negative gate voltage displaces the HOMO level closer to E_F signifying the accumulation of positive charge in the molecular junction.

In fact, Song *et al.* [51] have recently demonstrated that the molecular orbitals of MMMJs can indeed be shifted in electromigrated break junctions (EBJs). In this

experimental platform, reproducible nanometer-sized gaps are created in metal nanowires, which are defined on a gate electrode coated with a thin dielectric film. The nanometer-sized gaps are created by taking advantage of carefully controlled electromigration: the motion of metal atoms due to the momentum transfer from conducting electrons under a large current density condition. When one or a few molecules are trapped stochastically in the nanometer-sized gaps, the electronic structure of a MMMJ can be directly controlled by applying a gate voltage. Although EBJs are a powerful experimental platform for probing charge transport characteristics of MMMJs, this platform cannot be directly used in the studies of thermoelectric effects in molecular junctions because such studies have the additional requirements such as application of temperature differentials across the nanometer-sized gaps. Towards this goal, I carefully designed (considering both thermal and electrical aspects) and nanofabricated a novel experimental platform, electromigrated break junctions with integrated heater (EBJIHs), which will be discussed in detail in later chapters, and successfully employed it to demonstrate the possibility of tuning the thermoelectric properties of molecular junctions.

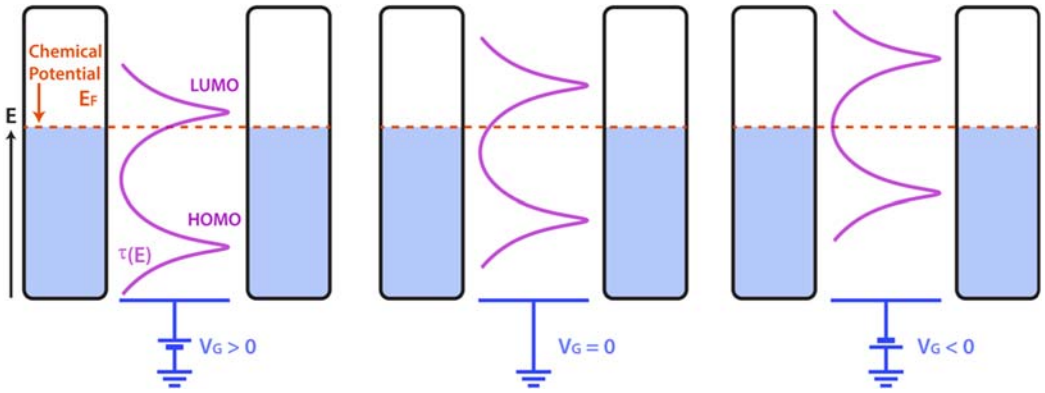

Figure 1.4: Schematic of the molecular orbitals gating. The electronic structure of a MMMJ is tuned by application of a gate voltage: a positive gate voltage ($V_G > 0$) shifts the LUMO level closer to the chemical potential E_F (left), while a negative gate voltage ($V_G < 0$) displaces it away from E_F (right).

1.3 Organization of this thesis

In this chapter I have briefly summarized the motivation for experimentally studying the relationship between the electronic structure and the thermoelectric properties of MMMJs. I have also briefly discussed past research in this and other related areas. The organization of the rest of this thesis is as follows:

Chapter 2 describes the nanofabrication process of EBJIHs and novel scanning thermal microscopy (SThM) probes. EBJIHs represent the main experimental platform used in my work to examine the thermopower gating hypothesis. Whereas, SThM probes are used for quantitatively investigating nanoscale thermal phenomena.

Chapter 3 describes ultra-high vacuum scanning thermal microscopy (UHV-SThM), a technique that I developed in collaboration with others and which was extensively leveraged to characterize the established temperature differentials across nanogaps in EBJIHs.

Chapter 4 describes my studies of thermal effects on electromigration of gold nanowires, which was studied by UHV-SThM. These studies lay the ground work for the creation of nanoscale gaps in EBJIHs.

Chapter 5 describes the experimental results of thermopower gating obtained using EBJIHs in two molecular systems—BPDT (biphenyl-4,4'-dithiol, HOMO-mediated off-resonant charge transport) and C_{60} (fullerene, LUMO-mediated resonant charge transport) molecular junctions.

Chapter 6 describes important questions that can be addressed in future work.

Chapter 2

Nanofabrication of scanning thermal microscopy probes and devices for molecular measurements

2.1 Introduction

In this chapter, I will present the detailed recipes of three nanoscale devices that I have nanofabricated in the last few years: EBJIHs, SThM probes and NTISTPs. I would like to emphasize that since reproducing these devices is not straightforward even in the case of working with the detailed recipes, refer first to Appendix A for precautions, which are critical to significantly reducing the failure rate.

2.2 EBJIHs

As mentioned in Chapter 1, EBJIHs (Electromigrated break junctions with integrated heater) represent a novel experimental platform for achieving the main objective of this thesis. The cross-sectional view and scanning electron microscope (SEM) image of a nanofabricated device are shown in Figure 2.1. The central goal in nanofabricating this device is to enable establishing very large temperature gradients (>10^9 K/m) across nanoscale gaps between the source and drain electrodes of a three-terminal device in spite of the presence of the underlying gate electrode, which provides a parasitic thermal

pathway that tends to annul temperature differentials across the nanometer-sized gaps. In order to conceive an appropriate design, I performed extensive finite element thermal modeling (will be discussed in Chapter 5) using COMSOL. Here, I provide a detailed recipe to minimize unnecessary trial and error in future nanofabrication of this device. The nanofabrication of EBJIHs involved multiple steps:

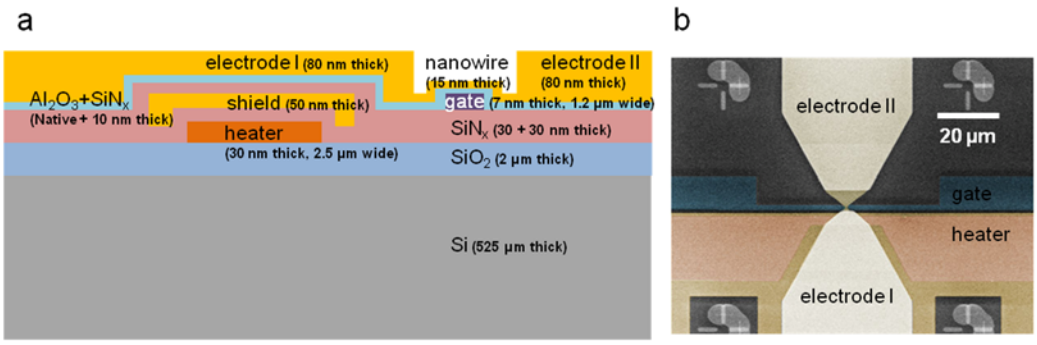

Figure 2.1: (a) Cross-sectional view (not drawn to scale and proportion) (b) SEM image of a nanofabricated EBJIH. The layers below the electrodes are created with materials having low thermal conductivity to prevent parasitic heat transfer between the electrodes. (Panels reproduced from the author's work of Ref. 52.)

1. A 2 μm thick low temperature oxide (LTO) is deposited on a silicon (Si) wafer. The thickness of the LTO layer (2 μm) is chosen to be much thicker than that of the usual case (500 nm) such as the insulating layer of a Si substrate. It is worth noting that the LTO layer, which has a low thermal conductivity (1 W/m·K), serves to thermally isolate the integrated heater from the underlying Si substrate, which is thermally much more conductive (150 W/m·K). A thickness of 2 μm was chosen as it is close to the maximum limit for performing e-beam lithography because thicker dielectric layer induces excessive charging, which hinders fine focusing.
2. HMDS spin-coating at 500 rpm for 7 seconds and at 3000 rpm for 35 seconds. It is preferred to pre-bake the wafer (at 115°C for 1 minute) before spinning to remove the moisture existing on the wafer.

3. LOR 5A spin-coating at 500 rpm for 7 seconds and at 3000 rpm for 35 seconds. Post-bake at 190°C for 7.5 minutes is required after spinning.
4. SPR220 (3.0) spin-coating at 500 rpm for 7 seconds and at 3000 rpm for 35 seconds. Post-bake at 115°C for 2.5 minutes is required after spinning.
5. The integrated heater (30 nm thick Au and 2.5 μm wide in the narrowest part, Figure 2.1b) is defined on LTO by photolithography. I used GCA AS200 AutoStepper with 0.35 seconds of exposure time (usually 0.3 – 0.4 seconds of exposure is reasonable for a Si substrate, while a 1 second exposure is necessary for a Pyrex substrate). Further, I adopted a localized heater design (instead of that having uniform width) in order to reduce parasitic heat transfer between the source and drain electrodes.
6. Soft-bake at 115°C for 2.5 minutes, then develop with AZ 726 (using CEE Developer) until all features are completely developed. I recommend checking under an optical microscope before proceeding further. Subsequently, oxygen (O_2) plasma cleaning for 2 minutes at 250 mW is performed to minimize under-developed PR residue.
7. 3/30 nm thick Cr/Au (integrated heater) is deposited by evaporation using EnerJet Evaporator.
8. Lift-off using Remover PG. I recommend leaving the sample in Remover PG for >12 hours although faster lift-off (~4 hours) is also possible. Further, lift-off using acetone does not work because LOR 5A is not resolved in acetone.
9. A short piranha (1:2 = H_2O_2:H_2SO_4) clean for 20 – 30 seconds to remove residues of HMDS, LOR and PR. Although the standard LNF recipe of a piranha clean is to use a 1:1 mixture of H_2O_2:H_2SO_4, I modified it to achieve better cleaning.
10. A 30 nm thick plasma enhanced chemical vapor deposition (PECVD) silicon nitride (SiN_x) is deposited using GSI PECVD on the entire wafer. It should be noted that performing PC/carrier clean recipe is required before every SiN_x deposition run. Since

the PECVD chamber is usually dirty, skipping this cleaning step can result in failure of the whole process.

11. In order to provide electrical access to the heater line, the SiN_x deposited on heater pads needs to be removed. Since this step does not include lift-off, it is not necessary to spin-coat HMDS and LOR 5A. Processes 4 – 6 described above (SPR220 (3.0) spin-coating, exposure, soft-bake, PR development and O_2 plasma cleaning) are used, then SiN_x is plasma etched for 15 seconds using LAM 9400. Subsequently, PR is completely stripped using acetone and a short piranha clean.
12. Processes 2 – 4 described above (HMDS, LOR 5A and SPR220 (3.0) spin-coating) are used.
13. The shield layer (50 nm thick Au) covering the integrated heater is defined by photolithography. This shield layer, which is subsequently electrically grounded, ensures that the excitation signal supplied to the heater does not capacitively couple to other electrodes and electronic components. Further, the design of the shield layer is chosen to enhance heat transfer from the heater to nanogaps (will be discussed in Chapter 5).
14. Process 6 described above (soft-bake, PR development and O_2 plasma cleaning) is used.
15. 3/50 nm thick Cr/Au (shield layer) is deposited by evaporation.
16. Processes 8 – 10 described above (lift-off, a short piranha clean and a 30 nm thick PECVD SiN_x deposition) are used.
17. Process 11 described above (the SiN_x on heater and shield pads is plasma etched for 15 seconds) is used.
18. Processes 2 – 4 described above (HMDS, LOR 5A and SPR220 (3.0) spin-coating) are used.

19. The Al gate (7 nm thick) is defined by photolithography. The gate electrode is chosen to be very thin so that its contribution to parasitic heat transfer between the source and drain electrodes is minimized.
20. Process 6 described above (soft-bake, PR development and O_2 plasma cleaning) is used.
21. 7 nm thick Al (gate electrode) is deposited by evaporation.
22. The Al gate is oxidized (by exposing to O_2 plasma for 10 minutes at 250 mW and to the cleanroom ambient for >12 hours), which is followed by a 10 nm thick PECVD SiN_x deposition. This SiN_x layer serves to reduce parasitic heat transfer. It is worth noting that from this point a short piranha clean cannot be used as H_2SO_4 attacks Al. In addition, Al can also be attacked by PRS 2000 and AZ 726 (this is another reason for the 10 nm thick PECVD SiN_x deposition to protect Al gate although additional dielectric layer sacrifices a gate coupling some extent), thus it is necessary to be very careful to keep the wafer clean.
23. The wafer is diced to 21 mm × 21 mm squares, which contains 9 chips (3 × 3) in each square. This step is for the effectiveness of subsequent e-beam lithography.
24. HMDS and MMA (8.5) MAA spin-coating at 500 rpm for 7 seconds and at 3000 rpm for 35 seconds. Post-bake at 180°C for 2.5 minutes is required after spinning.
25. 950K PMMA A4 (ER, e-beam resist) spin-coating at 500 rpm for 7 seconds and at 3000 rpm for 35 seconds. Post-bake at 180°C for 2.5 minutes is required after spinning.
26. Au nanowires (15 nm thick, 150 nm wide and 250 nm long) are defined by e-beam lithography using Raith-150 E-beam. It is worth noting that the writing speed of e-beam was selected to be <4 mm/s for a single line, and an area dose was chosen accordingly. The doses that I used here were 750 – 900 pC for a single line and 250 – 300 $\mu C/cm^2$ for an area.

27. ER is developed with a 1:3 mixture of MIBK and IPA for 1 minute, then the sample is rinsed with IPA for 30 seconds. Subsequently, the sample is rinsed with DI water thoroughly, and O_2 plasma cleaning for 2 minutes at 250 mW is performed.
28. 1/12 nm thick Ti/Au (nanowires) is deposited by evaporation.
29. Lift-off using acetone for >12 hours.
30. Clean with Remover PG for >20 minutes. Subsequently, the sample is rinsed with DI water thoroughly, and O_2 plasma cleaning for 5 minutes at 250 mW is performed.
31. Processes 2 – 4 described above (HMDS, LOR 5A and SPR220 (3.0) spin-coating) are used.
32. Au electrodes (80 nm thick) are defined by photolithography in order to ensure good electrical contact with Au nanowires and to provide electrical access to gate, heater and shield lines.
33. Process 6 described above (soft-bake, PR development and O_2 plasma cleaning) is used.
34. 3/80 nm thick Ti/Au (source and drain electrodes) is deposited by evaporation.
35. Processes 8 and 30 described above (lift-off, Remover PG and O_2 plasma cleaning) are used.
36. Dice to 7 mm × 7 mm chips. PR spin-coating (>5 μm) is required before this step to protect the sample during dicing.

2.3 SThM probes

The scanning thermal microscopy (SThM) technique used in this work leverages a modified atomic force microscopy (AFM) based probe that incorporates a nanoscale thermocouple into the probe tip. Specifically, I used these custom nanofabricated probes in conjunction with ultra-high vacuum scanning probe instrument to perform quantitative

measurements of temperature fields with nanometer resolution. This technique called ultra-high vacuum scanning thermal microscopy (UHV-SThM) [14] enables me to characterize temperature differentials across the nanometer-sized gaps in EBJIHs [52]. Further, I also utilized UHV-SThM for probing thermal effects during electromigration of Au nanowires [53] as it is a versatile tool for various nanoscale thermal studies. Here, I present a detailed recipe for nanofabrication of SThM probes. A brief nanofabrication process and SEM images of a nanofabricated SThM probe are shown in Figure 2.2. It is clearly seen that the diameter of the probe tip is ~100 nm, and the nanoscale thermocouple spans a spatial dimension of ~100 nm from the apex of the probe tip.

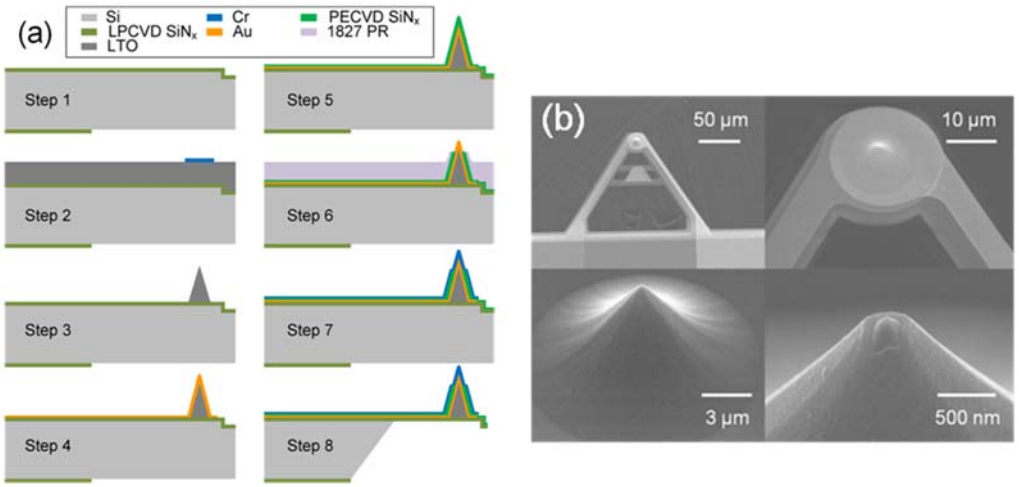

Figure 2.2: (a) Nanofabrication process of scanning thermal microscopy (SThM) probes: (Step 1) groove definition, LPCVD SiN_x deposition, backside patterning, (Step 2) LTO deposition, Cr cap patterning for the probe tip etching, (Step 3) LTO probe tip creation, (Step 4) Au line definition, (Step 5) PECVD SiN_x deposition as the insulating layer between two metal lines, (Step 6) thermocouple creation, (Step 7) Cr line definition and (Step 8) releasing of the probe cantilever. (b) SEM images show a nanofabricated SThM probe that has a Au-Cr thermocouple whose spatial dimensions are ~100 nm. (Panels reproduced from the author's work of Ref. 14.)

1. The nanofabrication process starts from a double side polished Si wafer, which is chosen for achieving a better KOH etching result in the final step.

2. SPR220 (3.0) spin-coating at 500 rpm for 7 seconds and at 3000 rpm for 35 seconds. Post-bake at 115°C for 2.5 minutes is required after spinning.
3. A 1.6 μm deep groove is defined by photolithography using MA/BA-6 Mask/Bond Aligner with 7 seconds of exposure time. It is noticeable that this groove increases the stiffness of the probe cantilever and prevents large deflections of the cantilever due to laser heating when the probe is operating in UHV: such deflections are expected due to differences in the thermal expansion coefficient of the materials of which the cantilever is made (will be discussed in Chapter 3).
4. Soft-bake at 115°C for 2.5 minutes, then develop with AZ 726 until all features are completely developed. Subsequently, O_2 plasma cleaning for 1 minute at 100 mW is performed.
5. The Si wafer is plasma etched for 25 seconds using STS Pegasus 4 (DRIE recipe 1). Subsequently, PR is completely stripped using acetone and a short piranha clean.
6. A 500 nm thick low-stress low pressure chemical vapor deposition (LPCVD) SiN_x is deposited (using S2T4 furnace) on both sides of the wafer. It should be noted that every furnace run requires pre-furnace clean (PFC) before the step.
7. SPR220 (3.0) spin-coating on the back side (the opposite side that the groove was patterned) of the wafer at 500 rpm for 7 seconds and at 3000 rpm for 35 seconds. Post-bake at 115°C for 2.5 minutes is required after spinning.
8. The SiN_x on the back side of the wafer is patterned by photolithography. This back side pattern facilitates the probe cantilever release by KOH etching in the final step.
9. Process 4 described above (soft-bake, PR development and O_2 plasma cleaning) is used.
10. The back side SiN_x is plasma etched for 4 minutes using LAM 9400. Subsequently, PR is completely stripped using acetone and a short piranha clean. Until here, step 1 in Figure 2.2a is accomplished.

11. PFC clean
12. A 8 μm thick LTO is deposited on both sides of the wafer (using S1T2 furnace; the deposition takes 24 hours, and re-initiating the furnace after every 6 hour period is needed.) and is annealed at 1000°C for 1 hour (using S5T4 furnace) in order to reduce the internal stress of low-stress SiN_x and LTO layers: the LTO layer will eventually be patterned to create the probe tip.
13. 150 nm thick Cr (Cr cap layer) is deposited on top of LTO by sputtering using Lab 18_02 Sputter. After this step if cracks emerge over the entire wafer, the quality of LTO is not suitable for the tip etching. In that case, I recommend removing Cr and LTO then redoing from the process 11 described above.
14. SPR220 (3.0) spin-coating at 500 rpm for 7 seconds and at 3000 rpm for 35 seconds. Post-bake at 115°C for 2.5 minutes is required after spinning.
15. The Cr layer is patterned by photolithography.
16. Process 4 described above (soft-bake, PR development and O_2 plasma cleaning) is used.
17. The Cr layer is etched using Cr-14 etchant, which is designed to facilitate HF etching of LTO to create the probe tip. Until here, step 2 in Figure 2.2a is accomplished.
18. The LTO probe tip is created by buffered HF (1:5 = HF:NH_4F) etching, which takes ~100 minutes. In order to obtain a very sharp tip, the etching status is frequently monitored under an optical microscope (the monitoring intervals are adjusted by the indicator information as shown in Figure 2.3). I recommend checking the tip sharpness under SEM before proceeding further. In addition, it should be noted that you need to be extremely careful during this step because HF is one of the most hazardous chemical. Subsequently, PR is completely stripped using acetone and a short piranha clean. Step 3 in Figure 2.2a is accomplished.
19. 5/90 nm thick Cr/Au (the first metal layer) is deposited by sputtering.

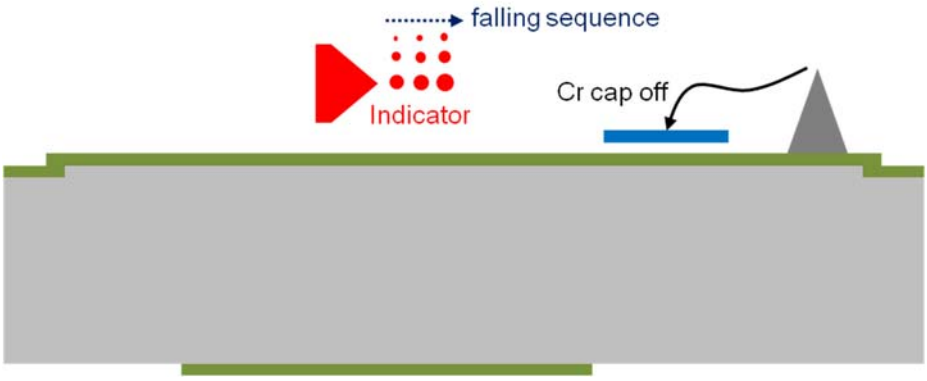

Figure 2.3: Schematic of the indicator for monitoring the tip etching status. As etching proceeds, the Cr cap on the indicator sequentially falls off, which indicates the right timing of stopping this process.

20. AZ 9260 spin-coating at 500 rpm for 7 seconds and at 2000 rpm for 35 seconds. Post-bake at 110°C for 2.5 minutes is required after spinning. From this point, thick PR (AZ 9260) is used instead of thin PR (SPR220 (3.0)) to protect the probe tip during photolithography.
21. The Au line is defined by photolithography using MA/BA-6 Mask/Bond Aligner with 45 seconds of exposure time. This Au line is the first metal layer of SThM probes.
22. AZ 9260 is developed with a 1:3 mixture of AZ 400K and DI water until all features are developed. Subsequently, the wafer is rinsed with DI water thoroughly, and O_2 plasma cleaning for 30 seconds at 100 mW is performed.
23. The Au line is patterned by Au-Cr-Au etching. It should be noted that Au etching is a very fast process, and the second Au etching step is required to ensure that the entire Au line is placed on the Cr adhesion layer. Subsequently, PR is completely stripped using acetone and a short piranha clean. Until here, step 4 in Figure 2.2a is accomplished.
24. A 70 nm thick PECVD SiN_x is deposited using GSI PECVD. As I mentioned above, performing PC/carrier clean recipe is required before every SiN_x deposition run. This

SiN_x layer is for electrically insulating two metal lines of SThM probes. Until here, step 5 in Figure 2.2a is accomplished.

25. SC 1827 spin-coating at 500 rpm for 7 seconds and at 1200 rpm for 35 seconds. Post-bake at 115°C for 2 minutes and hard-bake at 125°C for 20 minutes are required after spinning to ensure that PR is not burnt during the following plasma etching. The thickness of PR after spinning and baking is ~6 μm, and SC 1827 slightly covers the 8 μm tall probe tip due to its viscosity, which can be exploited for the nanoscale thermocouple creation at the apex of the probe tip.
26. PR and PECVD SiN_x are slowly plasma etched (using LAM 9400) until a very small portion of the Au layer is extruded. I recommend checking the etching status under an optical microscope and NanoMan AFM before proceeding further. Subsequently, PR is completely stripped using acetone and a short piranha clean. Until here, step 6 in Figure 2.2a is accomplished.
27. 90 nm thick Cr (the second metal layer) is deposited by sputtering.
28. Processes 20 – 22 described above (AZ 9260 spin-coating, exposure, PR development and O_2 plasma cleaning) are used.
29. The Cr line is patterned by etching (using Cr-14 etchant). I recommend checking the etching status under an optical microscope before proceeding further. This Cr line is the second metal layer of SThM probes and is deposited to create the nanoscale Au-Cr thermocouple at the end of the probe tip. Subsequently, PR is completely stripped using acetone and a short piranha clean. Until here, step 6 in Figure 2.2a is accomplished.
30. In order to provide electrical access to the Au line, the SiN_x deposited on Au line pads needs to be removed. Processes 20 – 22 described above (AZ 9260 spin-coating, exposure, PR development and O_2 plasma cleaning) are used, then SiN_x is plasma

etched for 2 minutes using LAM 9400. It is preferable to check the etching status under an optical microscope before proceeding further.

31. 100 nm thick Au is deposited by evaporation using EnerJet Evaporator on Au and Cr line pads to ensure good electrical contact.
32. Lift-off using acetone for >12 hours and a short piranha clean. Until here, step 7 in Figure 2.2a is accomplished.
33. In order to facilitate the probe cantilever release by KOH etching in the final step, the front side of the wafer is patterned by using processes 20 – 22 described above (AZ 9260 spin-coating, exposure, PR development and O_2 plasma cleaning). Subsequently, the wafer is soft-baked at 90°C for 20 minutes to ensure the protection of the probe tip during the following plasma etching.
34. The front side SiN_x is plasma etched for 5 minutes using LAM 9400. Subsequently, PR is completely stripped using acetone and a short piranha clean.
35. A 100 nm thick PECVD SiN_x is deposited to give a time delay between the front side and the back side KOH etching.
36. SThM probes are released by KOH etching.

2.4 Nanoscale thermocouple integrated scanning tunneling probes (NTISTPs)

NTISTPs are the scanning tunneling microscope (STM) version of SThM probes. I designed and nanofabricated these novel probes, which were leveraged to investigate heat dissipation in atomic scale junctions (Au-BDNC-Au, Au-BDA-Au and Au-Au) [54]. The nanofabrication process of NTISTPs is very similar to that of SThM probes. A brief description of nanofabrication process and SEM images of a nanofabricated NTISTP are shown in Figure 2.4. It is to be noted that nanofabricated NTISTPs are designed to be

much stiffer than SThM probes so as to enable stable trapping of atomic scale junctions (Au-Au or Au-molecule-Au).

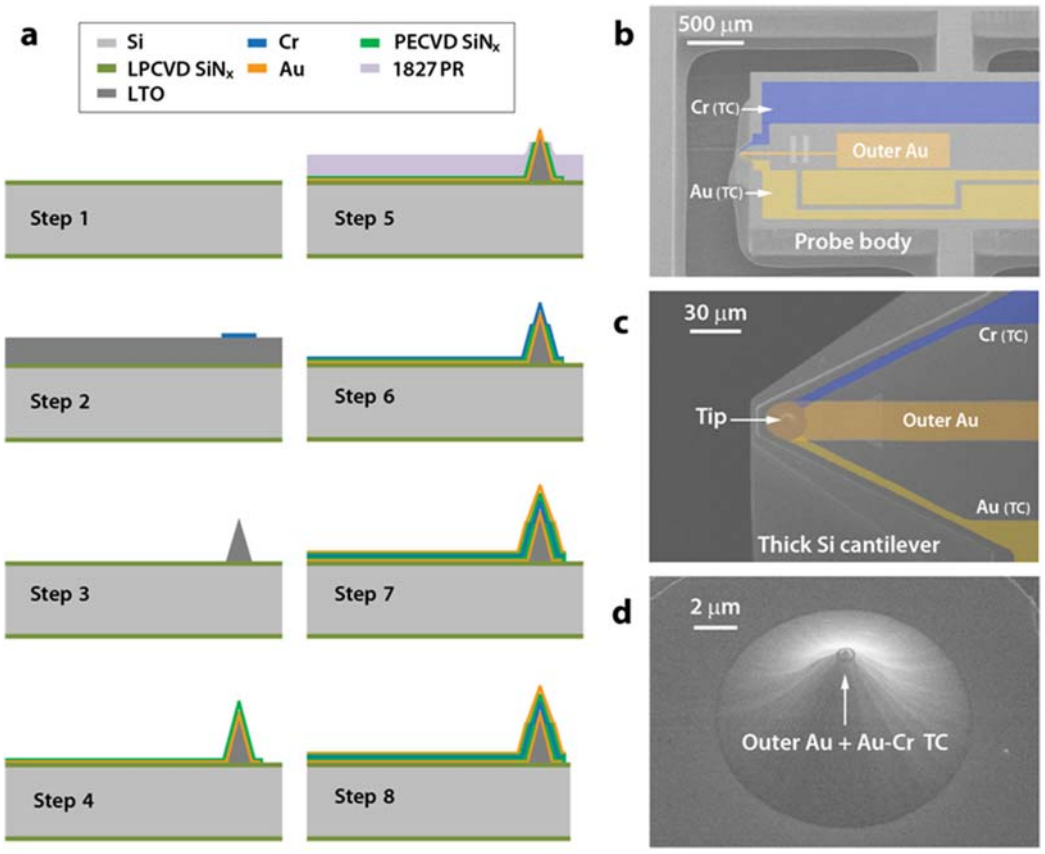

Figure 2.4: Nanofabrication of NTISTPs. (a) Brief nanofabrication steps involved in the creation of NTISTPs are shown. (b, c) SEM images of a nanofabricated probe. The false coloring identifies the metal layers (Au and Cr) that comprise the nanoscale thermocouple and the outermost Au layer that is used to create atomic scale junctions. (d) SEM image of the probe tip of a nanofabricated NTISTP. (Panels reproduced from the author's work of Ref. 54.)

1. The nanofabrication process starts from a Si wafer. The use of a double side polished Si wafer is not necessary because NTISTPs are released by deep reactive ion etching (DRIE) instead of KOH etching in the final step.
2. PFC clean
3. A 500 nm thick low-stress LPCVD SiN_x is deposited (using S2T4 furnace) on both sides of the wafer. Until here, step 1 in Figure 2.4a is accomplished.

4. A 8 μm thick LTO is deposited on both sides of the wafer (using S1T2 furnace; the deposition takes 24 hours, and re-initiating the furnace after every 6 hour period is needed.) and is annealed at 1000°C for 1 hour (using S5T4 furnace) in order to reduce the internal stress of low-stress SiN_x and LTO layers: the LTO layer will eventually be patterned to create the probe tip.
5. 150 nm thick Cr (Cr cap layer) is deposited on top of LTO by sputtering using Lab 18_02 Sputter. After Cr deposition if cracks emerge over the entire wafer, the quality of LTO is not suitable for the tip etching. In that case, I recommend removing Cr and LTO then redoing the process from PFC clean followed by LTO deposition.
6. SPR220 (3.0) spin-coating at 500 rpm for 7 seconds and at 3000 rpm for 35 seconds. Post-bake at 115°C for 2.5 minutes is required after spinning.
7. The Cr layer is patterned by photolithography using MA/BA-6 Mask/Bond Aligner with 7 seconds of exposure time.
8. Soft-bake at 115°C for 2.5 minutes, then develop with AZ 726 until all features are completely developed. Subsequently, O_2 plasma cleaning for 1 minute at 100 mW is performed.
9. The Cr layer is etched using Cr-14 etchant, which is designed to facilitate HF etching of LTO to create the probe tip. Until here, step 2 in Figure 2.4a is accomplished.
10. The LTO probe tip is created by buffered HF (1:5 = $HF:NH_4F$) etching, which takes ~100 minutes. In order to obtain a very sharp tip, the etching status is frequently monitored under an optical microscope (the monitoring intervals are adjusted by the indicator information as shown in Figure 2.3). I recommend checking the tip sharpness under SEM before proceeding further. In addition, it should be noted that you need to be extremely careful during this step because HF is one of the most hazardous chemical. Subsequently, PR is completely stripped using acetone and a short piranha clean. Step 3 in Figure 2.4a is accomplished.

11. 5/90 nm thick Cr/Au (the first metal layer) is deposited by sputtering.
12. AZ 9260 spin-coating at 500 rpm for 7 seconds and at 2000 rpm for 35 seconds. Post-bake at 110°C for 2.5 minutes is required after spinning. From this point, thick PR (AZ 9260) is used instead of thin PR (SPR220 (3.0)) to protect the probe tip during photolithography.
13. The Au line is defined by photolithography using MA/BA-6 Mask/Bond Aligner with 45 seconds of exposure time. This Au line is the first metal layer of NTISTPs.
14. AZ 9260 is developed with a 1:3 mixture of AZ 400K and DI water until all features are developed. Subsequently, the wafer is rinsed with DI water thoroughly, and O_2 plasma cleaning for 30 seconds at 100 mW is performed.
15. The Au line is patterned by Au-Cr-Au etching. It should be noted that Au etching is a very fast process, and the second Au etching step is required to ensure that the entire Au line is placed on the Cr adhesion layer. Subsequently, PR is completely stripped using acetone and a short piranha clean.
16. A 70 nm thick PECVD SiN_x is deposited using GSI PECVD. As I mentioned above, performing PC/carrier clean recipe is required before every SiN_x deposition run. This SiN_x layer is for electrically insulating two metal lines of NTISTPs. Step 4 in Figure 2.4a is accomplished.
17. SC 1827 spin-coating at 500 rpm for 7 seconds and at 1200 rpm for 35 seconds. Post-bake at 115°C for 2 minutes and hard-bake at 125°C for 20 minutes is required after spinning to ensure that PR is not burnt during the following plasma etching. The thickness of PR after spinning and baking is ~6 μm, and SC 1827 slightly covers the 8 μm tall probe tip due to its viscosity, which can be exploited for the nanoscale thermocouple creation at the apex of the probe tip.
18. PR and PECVD SiN_x is slowly plasma etched (using LAM 9400) until a very small portion of the Au layer is extruded. I recommend checking the etching status under an

optical microscope and NanoMan AFM before proceeding further. Subsequently, PR is completely stripped using acetone and a short piranha clean. Until here, step 5 in Figure 2.4a is accomplished.

19. 90 nm thick Cr (the second metal layer) is deposited by sputtering.
20. Processes 12 – 14 described above (AZ 9260 spin-coating, exposure, PR development and O_2 plasma cleaning) are used.
21. The Cr line is patterned by etching using Cr-14 etchant. I recommend checking the etching status under an optical microscope before proceeding further. This Cr line is the second metal layer of NTISTPs and is deposited to create the nanoscale Au-Cr thermocouple at the end of the probe tip. Subsequently, PR is completely stripped using acetone and a short piranha clean. Until here, step 6 in Figure 2.4a is accomplished.
22. In order to provide electrical access to the Au line, the SiN_x deposited on Au line pads needs to be removed. Processes 12 – 14 described above (AZ 9260 spin-coating, exposure, PR development and O_2 plasma cleaning) are used, then SiN_x is plasma etched for 2 minutes using LAM 9400. It is preferable to check the etching status under an optical microscope before proceeding further.
23. 100 nm thick Au is deposited by evaporation using EnerJet Evaporator on Au and Cr line pads to ensure good electrical contact.
24. Lift-off using acetone for >12 hours and a short piranha clean.
25. A 70 nm thick PECVD SiN_x is deposited to insulate the nanoscale thermocouple from the third metal layer for creating atomic scale junctions.
26. 5/90 nm thick Cr/Au (the outermost electrode) is deposited by sputtering.
27. Processes 12 – 14 described above (AZ 9260 spin-coating, exposure, PR development and O_2 plasma cleaning) are used.

28. The third metal (Au) layer is defined by Au-Cr-Au etching. This Au layer represents the outermost electrode of NTISTPs and is critical for creating Au-Au atomic contacts or Au-molecule-Au junctions. Subsequently, PR is completely stripped using acetone and a short piranha clean. Until here, step 7 in Figure 2.4a is accomplished.
29. The front side of the wafer is patterned by using processes 12 – 14 described above (AZ 9260 spin-coating, exposure, PR development and O_2 plasma cleaning). Subsequently, the wafer is soft-baked at 90°C for 20 minutes to ensure the protection of the probe tip during the following plasma etching.
30. The front side SiN_x is plasma etched for 6 minutes using LAM 9400. Subsequently, PR is completely stripped using acetone and a short piranha clean.
31. The front side of the wafer is patterned again by using processes 12 – 14 described above (AZ 9260 spin-coating, exposure, PR development and O_2 plasma cleaning). Subsequently, the wafer is soft-baked at 90°C for 1 hour to ensure that PR is not burnt during the following DRIE. This soft-bake process is very essential not to be failed at the very last step.
32. NTISTPs are released by DRIE (plasma etching through all the wafer) using STS Pegasus 4 (DRIE recipe 2).

Chapter 3

Ultra-high vacuum scanning thermal microscopy (UHV-SThM)

3.1 Nanometer resolution quantitative thermometry

In order to characterize temperature differentials across the nanometer-sized gaps in EBJIHs, I developed (in collaboration with others) nanoscale resolution quantitative thermometry, which has very high spatial and temperature resolutions [14]. This technique is called ultra-high vacuum scanning thermal microscopy (UHV-SThM) as it consists of a thermocouple integrated into an atomic force microscopy (AFM) probe tip and is operated in UHV environment. In this chapter, I will describe in detail UHV-SThM and its capabilities.

Nanometer resolution thermometry is critical for investigating energy dissipation in a variety of electronic and photonic devices [55, 56]. It also plays an important role in fundamental studies of energy transport in nanoscale devices [57-62]. The potential for wide applicability and the importance of nanometer resolution thermometry have spurred the development of various experimental techniques that can be used to obtain the information regarding temperature fields with nanometer to micrometer spatial resolution [55, 61, 63-66]. Among these techniques, SThM has succeeded in achieving high spatial resolution (<100 nm) on dielectric and metallic surfaces.

Although impressive progress has been made in the field of SThM, obtaining quantitative information regarding temperature fields using SThM has still remained elusive. Further, achieving high spatial resolution of ~10 nm or lower has also not been possible despite the need for such spatial resolution in detailed thermal studies on nanoscale devices. These apparent limitations of conventional SThM arise due to its operation in the ambient where quantitative local measurements of temperature fields are impeded by parasitic heat transfer between the tip and the sample via conduction through both air and the liquid meniscus that exists at the tip-sample interface [67]. Further, the spatial resolution of SThM in the ambient has been limited to ~50 nm due to the large tip-sample contact size that arises from the existing liquid meniscus [67]. Recently, a significant advance in SThM has been achieved through performing additional scans and using a mathematical model, which deconvolutes the effects of parasitic heat transfer [65]. This improvement partially overcomes the challenge of obtaining quantitative information of temperature fields; however, the liquid meniscus existing at the tip-sample interface still limits the spatial resolution to ~50 nm.

I recently developed (in collaboration with others) UHV-SThM, which overcomes some of the major limitations of conventional SThM and unambiguously demonstrates quantitative measurements of temperature fields with excellent temperature (~15 mK) and spatial (~10 nm) resolutions [14]. The improvement in spatial resolution was possible due to the elimination of the liquid meniscus in UHV. Further, quantitative local temperature measurements without any deconvolution algorithm were accomplished as heat transfer is completely dominated by the solid-solid contact (the diameter of ~10 nm) between the tip and the sample. A detailed description of UHV-SThM and its capabilities will be presented next.

3.2 Evaluation of the stiffness of SThM probes

The nanofabrication process of SThM probes has already been presented in Chapter 2. It should be noted that a groove was incorporated into the probe cantilever to make it stiffer (the effective stiffness is 4.0 ± 0.2 N/m) to prevent excessive deflections, which results from laser heating, while the probe operates in UHV. The effective stiffness of the probe cantilever was evaluated through two methods that are described below. This information is essential to estimate the probe contact force, which largely affects the probe sensitivity (will be discussed in section 3.4).

To numerically estimate the stiffness of the cantilver, I performed a finite element method (FEM) simulation using COMSOL. In this simulation, I included the effects of the geometry (the incorporated groove) and the various layers of SiN_x, Au and Cr that consist of the probe cantilever. Instead of directly calculating the effective stiffness of an as-fabricated V-shaped cantilever, I simplified the calculation by separating the probe cantilever into two beams and computing the stiffness of each individual beam. The first beam consists of the grooved 140 μm long, 500 nm thick SiN_x cantilever with thin-films of Au (90 nm) and SiN_x (70 nm) on the cantilever. The second beam consists of the grooved SiN_x cantilever on which thin-films of SiN_x (70 nm) and Cr (90 nm) are present. The effective stiffness of the V-shaped cantilever is well approximated by the sum of the stiffness of each beam. The values of Young's modulus and Poisson's ratio assumed in these calculations are as follows: SiN_x (289 GPa, 0.20) [68], Au (78 GPa, 0.44) [69] and Cr (279 GPa, 0.21) [69] respectively. Further, to estimate the effective stiffness of the cantilever the following boundary conditions were applied in each case: a 1 μN force was applied to one end of the SiN_x cantilever while the other end of the cantilever was fixed. From the computed deflections, the effective stiffness of the grooved cantilever was

estimated to be 4.2 N/m as represented in Figure 3.1. The value of the effective stiffness is 20 times larger than that of a similar cantilever (0.2 N/m) on which there is no groove.

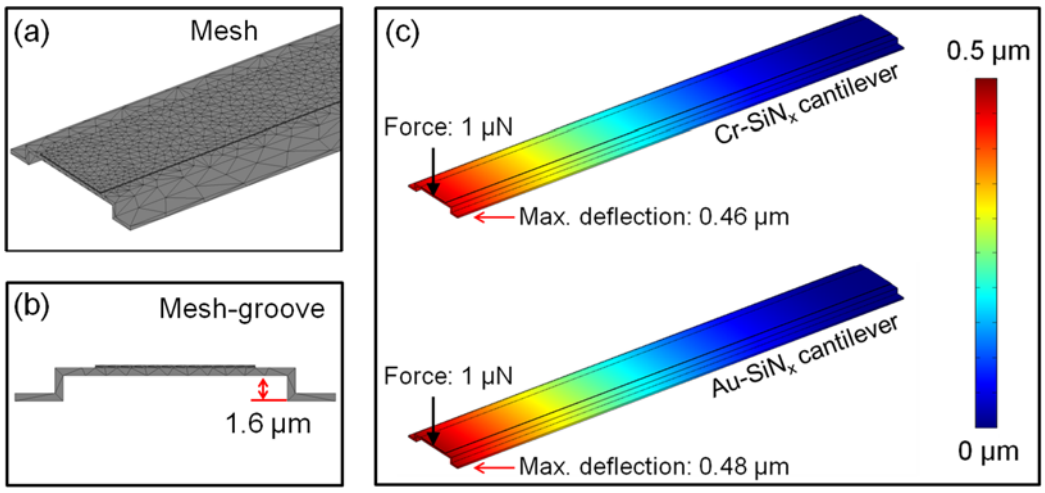

Figure 3.1: Calculated deflections of two beams consisting of either Au/SiN_x or SiN_x/Cr layers on a grooved SiN_x cantilever. (a, b) depict calculated geometry of the grooved cantilever. (c) shows deflections of two beams upon application of a 1 μN force. (Panels reproduced from the author's work of Ref. 14.)

In a second approach, the stiffness of SThM probes was estimated experimentally by taking advantage of the predictions of the equipartition theorem. Such an approach was indeed used in past work by others [70] and was found to yield accurate results. Briefly, the mean square displacement ($\langle x^2 \rangle$) of the end of the probe tip can be related to the temperature of a reservoir (at a temperature T) with which it is in thermal equilibrium via the following expression,

$$\frac{1}{2}k_B T = \frac{1}{2}c\left\langle x^2 \right\rangle \tag{3.1}$$

where k_B is the Boltzmann's constant, T is the absolute temperature, c is the stiffness of SThM probes, and x is the displacement of the probe tip due to fluctuations at equilibrium [71], respectively. This result is strictly valid only when the probe is in thermal equilibrium with a reservoir. Here, the diode laser (the wavelength of ~635 nm) used in

measuring cantilever deflections has an incident power of ~1 mW and causes substantial heating raising the temperature of the probe to ~466 K (measured by the nanoscale thermocouple integrated into the probe tip). Whereas, the thermal reservoir with which the cantilever is in-contact is at a temperature of ~298 K. Since the source of the thermally driven fluctuations of the cantilever is the thermal reservoir with which the probe is in-contact, the appropriate temperature to use in Equation 3.1 is the temperature of the reservoir (~298 K) [72].

To estimate the thermally driven mean square deflections ($<x^2>$) of the cantilever, x was first recorded using a photo diode when the probe tip is not in-contact with any surface. The power spectral density (PSD) of thermally driven oscillations was obtained from these data and is shown in Figure 3.2. The PSD features a peak at ~73 kHz corresponding to the resonant frequency of the cantilever. Since the dominant contributions of thermally driven fluctuations are at and around the resonant frequency, the PSD was integrated in a 5 kHz band of frequencies centered at ~73 kHz. From this, the mean square displacement of SThM probes was estimated to be $\sim 1.04 \times 10^{-21}$ m^2. Finally, this estimated $<x^2>$ was substituted in Equation 3.1 to estimate the stiffness to be ~4.0 N/m. The numerical and experimental estimates of the stiffness of the SThM cantilever are in good agreement with each other. Therefore, the stiffness value of 4.0 ± 0.2 N/m is assumed in this work.

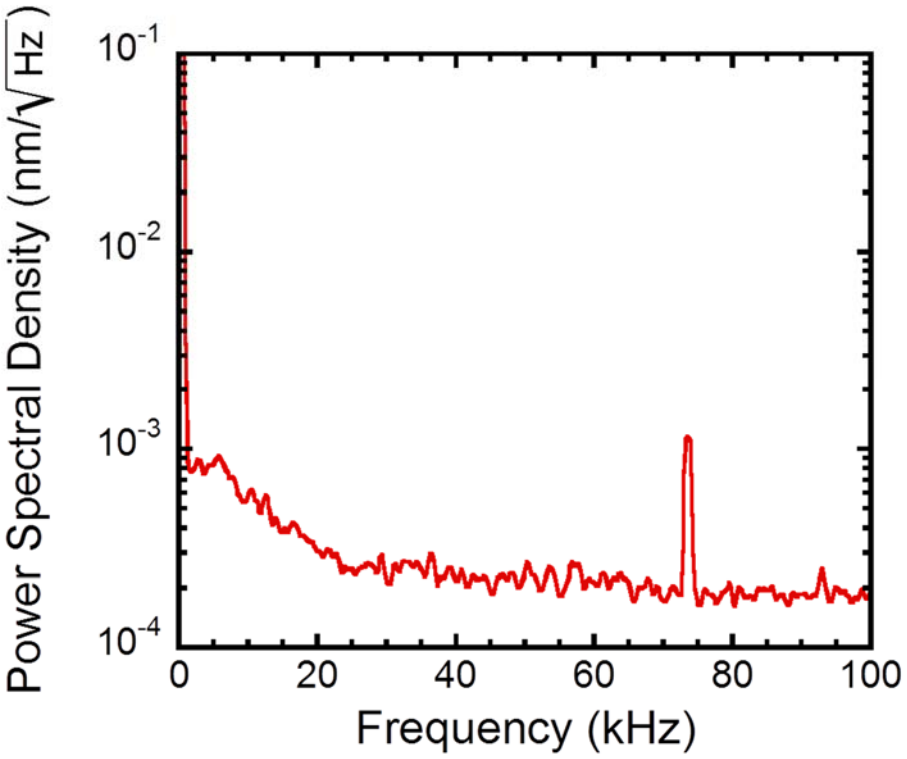

Figure 3.2: Measured power spectral density of a SThM probe when it is out-of-contact with any surface. (Figure reproduced from the author's work of Ref. 14.)

3.3 Measurement of the effective Seebeck coefficient of the Au-Cr thermocouple

The temperature sensor embedded in the probes of UHV-SThM is a nanoscale thermocouple. Therefore, the measured signals are thermoelectric voltages. To leverage this technique for quantitative thermometry it is required to calibrate the probes to relate thermoelectric voltages to temperature changes. In order to estimate the effective Seebeck coefficient ($S_{\text{Au-Cr}}$) of the Au-Cr thermocouple integrated into SThM probes, I pursued an approach similar to that adapted by others previously [67]. A SThM probe was mounted onto a substrate that has an electrical heater as shown in the inset of Figure 3.3. Good thermal contact between the substrate and the tip was achieved by attaching the tip to the substrate via a thermally conducting epoxy. Further, two thermocouples were attached to

the substrate and the cantilever as shown in the inset of Figure 3.3. The temperature of the substrate was then increased in steps using the electrical heater, while the temperature of the substrate (T_S) and the cantilever (T_C) were recorded from two thermocouples attached to the substrate and the cantilever. Thermoelectric voltages generated at the Au-Cr thermocouple (V_{TE}) was also recorded as the substrate temperature was increased as represented in Figure 3.3. Given the excellent thermal contact between the tip and the substrate, the probe tip temperature (T_{tip}) can be assumed to be the same as the substrate temperature ($T_S = T_{tip}$). Therefore, the measured thermoelectric voltages (V_{TE}) can be directly related to the Seebeck coefficient of the Au-Cr thermocouple by $V_{TE} = S_{Au\text{-}Cr} \times (T_S - T_C)$. From the data shown in Figure 3.3, $S_{Au\text{-}Cr}$ is estimated to be 16.28 ± 0.15 μV/K. This measured Seebeck coefficient of the probe is in good agreement with that of similar probes nanofabricated by others in previous studies [65, 67].

3.4 Characterization of the probe sensitivity in UHV

The sensitivity of SThM probes can be defined as the temprature rise of the probe tip per unit temperature rise of the sample. In general, the temperature rise of SThM probes is not the same as that of the sample with which it is in-contact. This temperature difference in the tip and the sample is due to the large thermal contact resistance between the tip and the sample. Further, it is expected that the sensitivity of SThM probes depends on various factors including the materials consisting of the tip and the sample and the force applied on the probe cantilever, which determines the contact diameter between the tip and the sample.

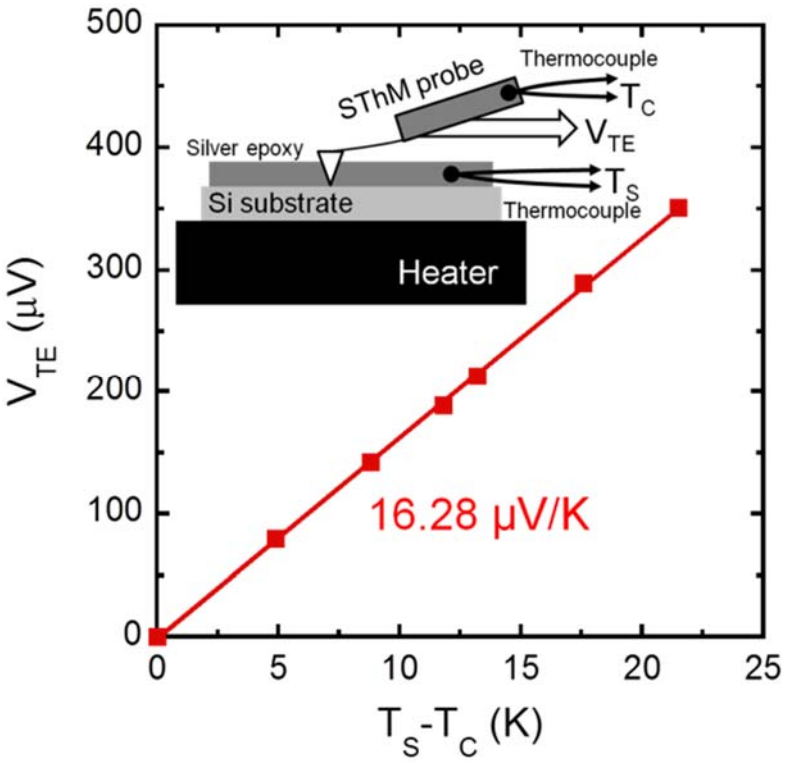

Figure 3.3: Measured thermoelectric voltages (V_{TE}) of the Au-Cr thermocouple as a function of temperature difference (T_S – T_C) between the substrate and the probe cantilever. The temperature of the probe tip (T_{tip}) and the substrate (T_S) are assumed to be the same due to the excellent thermal contact between the tip and the substrate. The inset shows the measurement setup used in this characterization. (Figure reproduced from the author's work of Ref. 14.)

In the past work by Shi *et al.* [67], it was shown that the sensitivity of SThM probes, operating in the ambient, depends on the size of the region that was being heated. Specifically, it was shown that when a SThM probe was placed in-contact with a 5 μm wide platinum (Pt) line, which was electrically heated, the measured sensitivity was ~0.5 K/K. Whereas, when the same probe was placed in-contact with a heated 350 nm wide Pt line, the sensitivity was reduced dramatically to ~0.05 K/K. This large variation in the probe sensitivity arises due to parasitic heat conduction between the tip and the sample through air and makes it impossible to directly perform quantitative temperature measurements using SThM probes operating in the ambient.

In order to measure the sensitivity of SThM probes nanofabricated by me and to unambiguously demonstrate the invariance of the probe sensitivity in UHV, three different Pt lines that are 50 nm thick and 200 nm, 1 μm and 5 μm wide respectively were employed. All Pt lines were deposited on a 600 nm thick SiO_2 layer that was thermally grown on a Si wafer. For the 5 μm and 1 μm wide samples, Pt lines and pads (Ti/Pt: 3/50 nm) were photolithographically defined by evaporation and lift-off. For the 200 nm wide sample, pads (Ti/Pt: 3/50 nm) were first photolithographically defined by evaporation and lift-off. Then, a Pt line (Ti/Pt: 3/50 nm) was defined by e-beam lithography, evaporation and lift-off. Finally, a ~10 nm thick layer of aluminum oxide (Al_2O_3) was conformally deposited using atomic layer deposition (ALD) on all Pt line samples as shown in Figure 3.4. This thin layer of Al_2O_3 serves two important purposes: 1) it prevents accidental electrical shorts between the Cr layer of the probe tip and Pt lines even if the native chrome oxide on the Cr layer is abraded during extensive scanning experiments, 2) it enables the condition of identical tip-sample contact materials on the entire samples. It is noticeable that the Al_2O_3 layer deposited by ALD is very thin and amorphous [73] and has a very small thermal conductivity (~1 W/m·K) [74]. Therefore, this Al_2O_3 layer does not cause any appreciable perturbation in temperature fields of the sample surfaces as shown in Figure 3.5. Here, I performed two-dimensional thermal modeling calculations using COMSOL since Pt lines are long enough compared with their width and thickness. Further, due to the symmetry of the problem it is sufficient to solve temperature fields in one half of the samples as represented in Figure 3.5c.

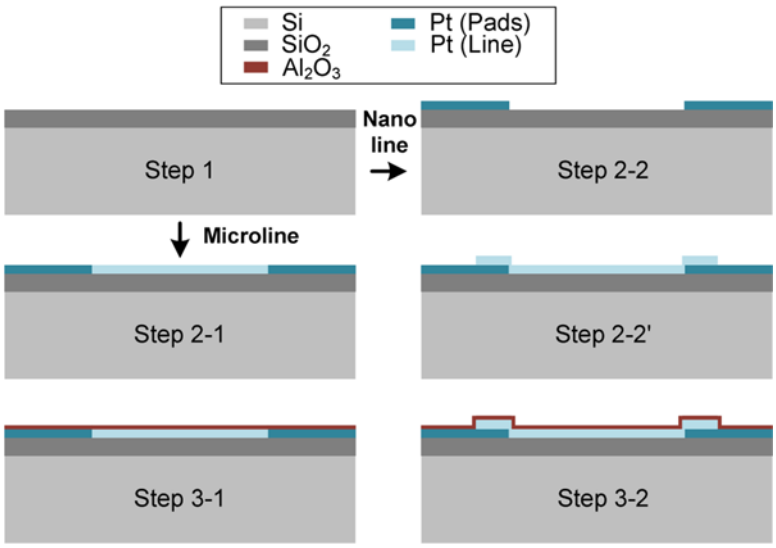

Figure 3.4: Nanofabrication process of Pt line samples: (Step 1) SiO_2 thermal growing, (Step 2-1) Pt line and pads definition by photolithography for the microline samples, (Step 3-1) Al_2O_3 deposition by ALD for the microline samples, (Step 2-2) Pt pads definition by photolithography for the nanoline sample, (Step 2-2') Pt line definition by e-beam lithography for the nanoline sample, (Step 3-2) Al_2O_3 deposition by ALD for the nanoline sample. (Figure reproduced from the author's work of Ref. 14.)

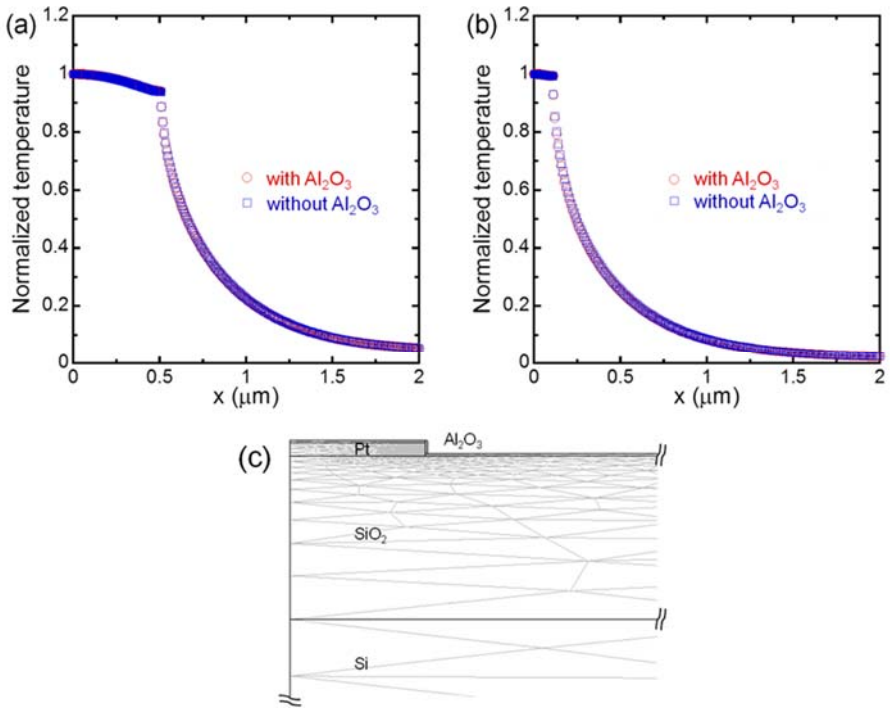

Figure 3.5: (a) Calculated amplitude of temperature oscillations (at 10 Hz) of a 1 μm wide Pt line sample with and without Al_2O_3 layer. (b) As (a) but for a 200 nm wide Pt line sample. (c) Two-dimensional meshed FEM domain used in the calculations. (Panels reproduced from the author's work of Ref. 14.)

All Pt lines used in the experiments were patterned in a four-probe configuration as shown in Figure 3.6a. In order to heat Pt lines, an alternating current (AC) at a known frequency (f = 5 Hz) and amplitude (I_0) was supplied through Pt lines (the specific choice of the oscillation frequency, f = 5 Hz, will be discussed in section 3.6). Due to Joule heating, the temperature amplitude of Pt lines oscillates at 2f, leading to the oscillation of their resistance at 2f. The component of the voltage drop across Pt lines oscillating at 3f (Figure 3.6a) is related to the temperature amplitude oscillations of Pt lines by $\Delta T(2f) = 2(\mathrm{d}T/\mathrm{d}R) \times V(3f) / I_0$, where $\Delta T(2f)$ is the amplitude of temperature oscillations at 2f, R is the resistance of Pt lines, and $V(3f)$ is the amplitude of the voltage oscillations across Pt lines at 3f. In order to determine the value of the temperature coefficient of resistance (TCR, $\mathrm{d}T/\mathrm{d}R$), the four-probe resistance of a 5 μm wide Pt line was measured while changing the ambient temperature as shown in Figure 3.7, which turned out to be 0.0023 K^{-1} at room temperature. Similar experiments performed on 1 μm and 200 nm wide Pt lines displayed very similar TCR values.

Before measuring the sensitivity of SThM probes, it is necessary to choose the contact force at which the sensitivity of the probe is characterized. This is important because the applied contact force largely affects the tip-sample contact size. In order to determine the appropriate contact force a SThM probe, which was initially separated from a Pt line whose temperature was modulated at 2f (10 Hz), was slowly displaced towards the Pt line. During this process, deflections of the SThM probe was recorded using an optical scheme [75]. The measured deflections were used to estimate the applied force on the probe cantilever from the known stiffness determined in section 3.2. Further, the temperature amplitude oscillations of the probe tip at 2f (10 Hz) were also simultaneously recorded using a lock in amplifier (SR 830) in a bandwidth of 0.26 Hz.

Data obtained in one such experiment are shown in Figure 3.6b where it is clear that the applied force on the probe cantilever is negligible when the probe is away from the sample. When the probe is in close proximity to the sample it suddenly jumps into contact due to the van der Waals force between the tip and the sample. As soon as the mechanical contact is established, the temperature amplitude oscillations of the probe tip at $2f$ (10 Hz) become detectable. After the initial contact, the amplitude of the measured temperature signals increases monotonically as the contact force is increased until the signals almost saturate. This behavior can be understood by noting that as the tip-sample contact force increases, the tip and the sample first deform elastically resulting in a gradual increase in the contact diameter. However, after transition to plastic deformation, the contact diameter no longer increases significantly resulting in the quasi-saturation of the measured temperature signals. It is clear from Figure 3.6b that a larger contact force results in a larger probe sensitivity. However, a larger contact force also increases the contact diameter, which results in a decrease in the spatial resolution of the probe. As a compromise, a contact force of 150 ± 15 nN was chosen for all further experiments as it corresponds to the smallest force where the measured temperature signals have almost saturated. The uncertainty of ±15 nN in the contact force arises from the uncertainty in the effective stiffness of the cantilever and the uncontrolled deflections resulting from bimaterial effects.

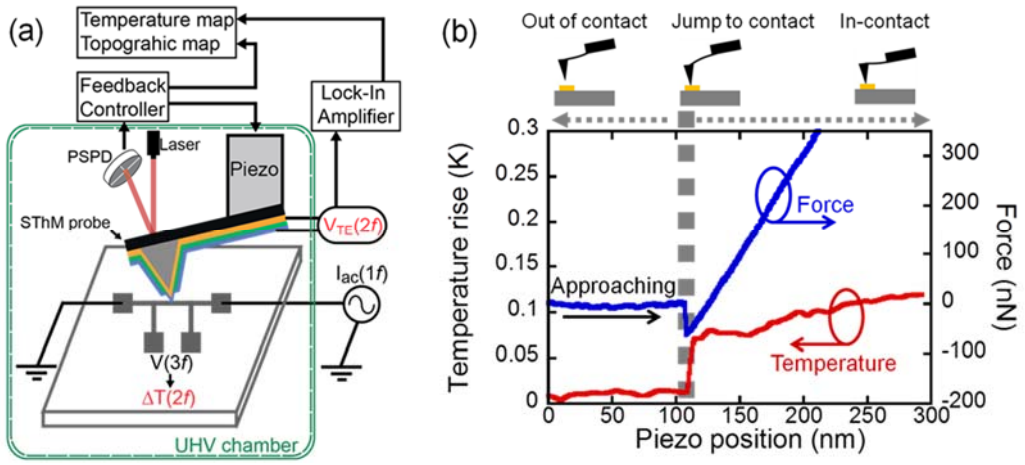

Figure 3.6: (a) Schematic of the experimental setup used in characterizing the sensitivity of SThM probes. The experiments were performed in UHV ($<10^{-9}$ torr). A sinusoidal electric current oscillating at f (5 Hz) was supplied through a Pt line and caused temperature amplitude oscillations of the Pt line at $2f$. The temperature amplitude oscillations were measured by monitoring the oscillations in the voltage drop across the Pt line at $3f$. After a SThM pobe was placed in the mechanical contact with the Pt line, thermoelectric voltages oscillating at $2f$ were recorded using a lock-in amplifier and converted to local temperature using the previously determined effective Seebeck coefficient of the Au-Cr thermocouple ($S_{\text{Au-Cr}}$). (b) Applied force on a SThM probe and temperature signals of the probe when it was gradually displaced towards a 1 μm wide heated Pt line. A sudden jump in temperature signals of the Au-Cr thermocouple was observed when the probe made the mechanical contact with the sample, and temperature signals increased steadily afterwards. (Panels reproduced from the author's work of Ref. 14.)

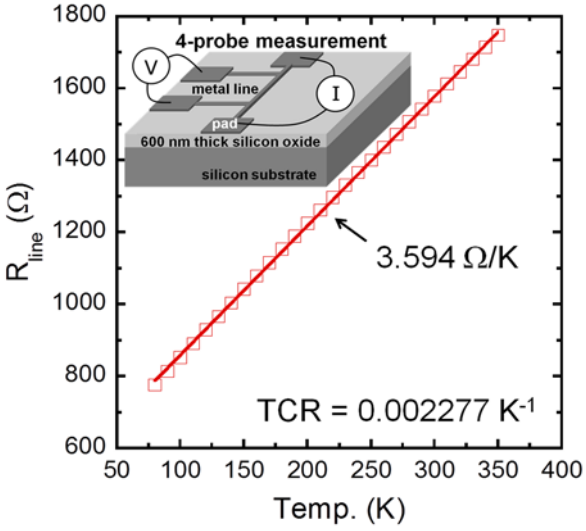

Figure 3.7: Four-probe resistance of a 5 μm wide Pt line as a function of the ambient temperature, which was varied from 80 K to 350 K in a cryostat (in a vacuum) to estimate TCR (dT/dR) of the Pt line. (Figure reproduced from the author's work of Ref. 14.)

For accurate estimation of the contact force, the effects of temperature changes on deflections of the probe cantilever were considered. This is especially important because the SThM probe cantilever consists of multiple layers of Au-SiN_x and Cr-SiN_x, which have different thermal expansion coefficient. It is worth noting that before the probe is in-contact with a sample, the temperature of the probe is raised by ~150 K (DC temperature rise) above the ambient temperature due to the heating from the incident laser on the probe reflector. Therefore, when the probe tip touches an unheated sample, the cooling of the probe can result in deflections of the cantilever, which adds an uncertainty to the measured deflections (i.e. the contact force) of the cantilever.

In order to estimate the uncertainty in the contact force, the temperature profiles of the cantilever before and after contact with an unheated sample was first calculated by finite difference modeling as shown in Figure 3.8. From the computed temperature profiles, it can be seen that the maximum temperature difference of the cantilever between the states of in-contact and out-of-contact is ~3.8 K: the change is small because the thermal contact resistance is much larger than the probe thermal resistance. Then, deflections of the cantilever due to the bimaterial effects were calculated using COMSOL. The modeling suggests that the maximum deflection of the cantilever is ~2.4 nm towards the sample when the temperature drop at the end of the cantilever is ~3.8 K (as suggested by the data shown in Figure 3.8). Since the maximum deflection and the stiffness of the probe cantilever are ~2.4 nm and 4.0 ± 0.2 N/m respectively, the uncertainty in the contact force due to the bimaterial effects is estimated to be ~10 nN.

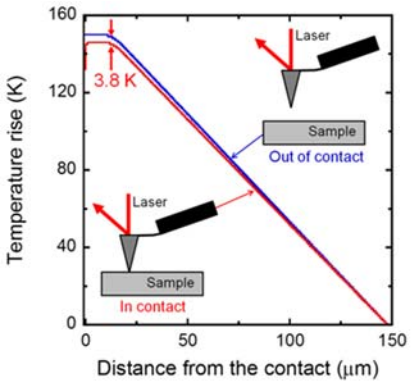

	Au	Cr	SiN_x
Thickness (*t*) [nm]	90	90	500
Young's modulus (*E*) [GPa]	78	279	289
Width (*b*) [μm]	10	10	20
Thermal expansion coefficient (α) [10^{-6}]	14.2	4.9	3.3

Figure 3.8: Calculated temperature profiles of the probe cantilever by finite difference modeling when the probe is in-contact or out-of-contact with an unheated Pt line. The table on the right shows the assumed values for calculating the uncertainty of the contact force by the bimaterial effects and for finite difference modeling of the thermal contact conductance of SThM probes, which will be discussed in section 3.5. (Panels reproduced from the author's work of Ref. 14.)

Given the contact force of 150 ± 15 nN, the contact diameter can be estimated using the classical Hertzian theory [55]:

$$a_{\text{Hertz}} = \left(\frac{6rP}{E^*}\right)^{1/3} \tag{3.2}$$

where a_{Hertz} is the contact diameter, r is the probe tip radius (~100 nm for SThM probes nanofabricated by me as represented in Chapter 2), P is the applied force (150 nN), and $E^* = [(1 - \upsilon_1^2) / E_1 + (1 - \upsilon_2^2) / E_2]^{-1}$ the effective elastic modulus obtained from Young's moduli (E_1, E_2) and Poisson's ratios (υ_1, υ_2) of the tip and the substrate materials. From Equation 3.2, the contact diameter for a Cr coated tip in contact with Al_2O_3 surface is estimated to be ~7 nm. Further, assuming elastic deformation the resulting pressure at the point contact can be estimated to be ~6.8 GPa. However, if plastic deformation occurs, the contact diameter can be larger and can be estimated [55] using,

$$a_{\text{Plastic}} = \left(\frac{4P}{\pi H}\right)^{1/2} \tag{3.3}$$

where H is the hardness of softer material (Cr) and is ~1.1 GPa. From Equation 3.3, the contact diameter for the applied force of 150 nN is estimated to be ~13 nm. Therefore,

this discussion suggests that the contact diameter is ~10 nm for the applied force of 150 ± 15 nN.

The sensitivity of SThM probes in UHV was characterized by performing experiments on three Pt lines, which are 50 nm thick and 200 nm, 1 μm and 5 μm wide respectively. In each experiment, the amplitude of temperature oscillations of the probe tip at $2f$ (10 Hz) was recorded as a function of the amplitude of temperature oscillations of heated Pt lines. The data obtained from these experiments are shown in Figure 3.9 from which the sensitivity of SThM probes is estimated to be 0.034 ± 0.006 K/K and is independent of the heated area. This invariance of the probe sensitivity with the heated area is in strong contrast to the past SThM work performed by others (operated under the ambient) where large variations in the probe sensitivity were observed [67] when the heated area was changed. This result can be easily understood by noting that heat transfer from Pt lines to the probe tip is primarily dominated by the tip-sample contact (the diameter of ~10 nm) as all other mechanisms for heat transfer between the tip and the sample such as conduction through air and liquid meniscus as well as near field radiation are negligible.

The measured sensitivity of UHV-SThM probes is smaller than what was observed by others in the past for similar probes operating in the ambient. The reduced sensitivity is primarily due to the larger tip-sample thermal contact resistance as parasitic heat transport pathways between the tip and the sample are eliminated in UHV. A simple resistance network model provided in the inset of Figure 3.9 can be used to estimate the expected sensitivity of UHV-SThM probes. From the resistance network, the sensitivity of the probe can be expressed as:

$$\text{Sensitivity} = \frac{R_C}{R_C + R_{TS}} \tag{3.4}$$

where $R_C = R_{tip} + R_{can}$ is the sum of the thermal resistances of the probe tip (R_{tip}) and the cantilever (R_{can}), whereas R_{TS} is the thermal resistance of the contact between the tip and

the sample. The thermal resistances of the tip and the cantilever can be estimated from knowledge of the geometry of SThM probes and the thermal conductivity of the various materials of which the probe is made and is found to be ~5 × 10^6 K/W. The thermal contact resistance (R_{TS}) at a solid-solid point contact between a conical shaped object and a semi-infinite solid can be approximately estimated using the following expression [55]:

$$R_{TS} = \left[\pi a \left(\frac{k_s k_{tip} \tan\theta}{2k_s + k_{tip} \tan\theta} \right) \right]^{-1} \tag{3.5}$$

where k_{tip} and k_s are the thermal conductivity of the conical tip and the semi-infinite solid, a is the point contact diameter (~10 nm) and θ (~21°) is the half angle of the conical tip. The tip-sample thermal contact resistance can be estimated using Equation 3.5 by assuming the sample as a semi-infinite solid with the thermal conductivity k_s of ~1 W/m·K as it comprises of a thin-film of amorphous Al_2O_3 and ~600 nm thick SiO_2. Further, it is reasonable to assume the probe tip to be equivalent to the one made completely of SiO_2, therefore k_{tip} is ~1 W/m·K. Under these assumptions, the thermal resistance of the tip-sample contact (R_{TS}) can be estimated to be ~2 × 10^8 K/W. This crude estimation is in good agreement with a more detailed finite difference model that predicts a thermal contact resistance of ~10^8 K/W (will be discussed in section 3.5). Using Equation 3.4 and the estimated thermal resistances, the sensitivity of the probe can be estimated to be ~0.02 K/K, which is in reasonable agreement with the measured value.

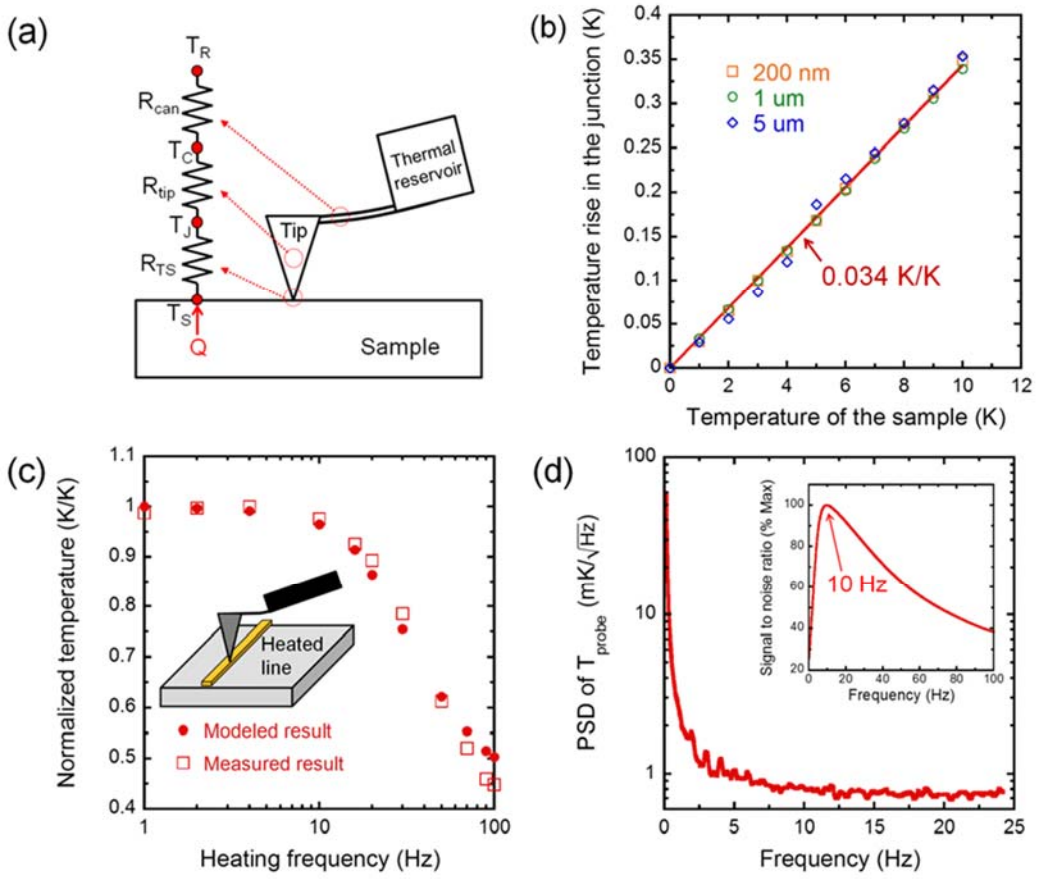

Figure 3.9: (a) Resistance network to model the thermal resistances at the tip-sample contact and the probe. (b) Measured temperature rise of the Au-Cr thermocouple as a function of the temperature rise in 5 μm, 1 μm and 200 nm wide heated Pt lines. The probe tip is in the mechanical contact with Pt lines with a contact force of ~150 nN. (c) Measured and modeled frequency responses of temperature signals when the probe is in-contact with a heated Pt line with a contact force of ~150 nN. (d) Measured power spectral density (PSD) of thermoelectric voltage noise in the Au-Cr thermocouple. The inset shows the signal to noise ratio (S/N) at different frequencies. (Panels reproduced from the author's work of Ref. 14.)

3.5 Finite difference modeling of thermal contact conductance

In order to estimate the thermal contact conductance for the applied force of ~150 nN, which is estimated to result in a contact diameter of ~10 nm, a finite difference modeling that is similar to that developed by others in past studies [65, 67, 76] was adopted.

The temperature distribution for the configuration shown in Figure 3.10 can be modeled using a one-dimensional heat conduction equation:

$$\sum \rho_i c_{p,i} A_i(x) \frac{\partial \theta(x,t)}{\partial t} = \frac{\partial}{\partial x}\left(\sum k_i A_i(x) \frac{\partial \theta(x,t)}{\partial x} \right) \tag{3.6}$$

where x is the distance from the tip-sample contact, $\theta(x, t)$ is the temperature, $A(x)$ is the cross-sectional area, ρ is the density, c_p is the heat capacity, k is the thermal conductivity and i represents the ith layer of the materials consisting of the probe. Any ballistic phonon transport effects were neglected as the tip and the substrate are primarily made of amorphous SiO_2, which has short phonon mean free paths.

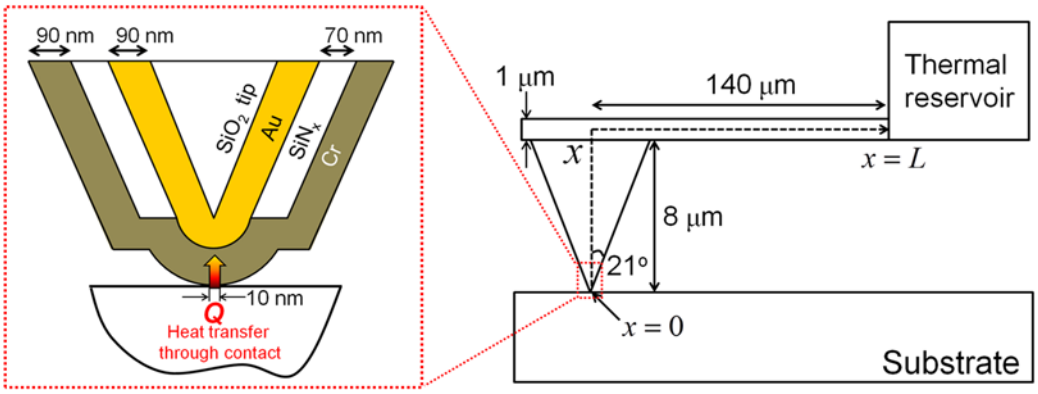

Figure 3.10: Schematic of a SThM probe in contact with a sample. x represents the position in the probe and is set to zero at the end of the probe tip where the tip is in-contact with the sample. Heat is assumed to be transferred through the point contact whose diameter is ~10 nm. The end of the probe cantilever is connected to a thermal reservoir whose temperature is ~298 K. (Figure reproduced from the author's work of Ref. 14.)

Since the temperature amplitude oscillates sinusoidally, Equation 3.6 is simplified by setting $\theta(x, t) = T(x) \cdot e^{j\omega t}$ to get,

$$\sum \rho_i c_{p,i} A_i(x) T(x) j\omega = \frac{d}{dx}\left(\sum k_i A_i(x) \frac{dT(x)}{dx} \right) \tag{3.7}$$

where $T(x)$ is the amplitude of temperature oscillations at x. Further, to calculate the thermal contact conductance the following boundary conditions were used:

$$Q = \sum k_i A_i(x) \frac{dT(x)}{dx}\bigg|_{x=0} \quad \text{and} \quad T(L) = 0 \tag{3.8}$$

where Q is the heat transferred through the tip-sample contact, and L is the distance from the tip-sample contact to the end of the probe cantilever.

In order to estimate the thermal contact conductance using this model, it is necessary to know the thermal conductivity of various thin-films that are parts of SThM probes. The thermal conductivity of metal thin-films was first estimated by the Wiedemann-Franz law [67]. Since application of the Wiedemann-Franz law requires knowledge of the electrical resistivity, an approach similar to that used in past studies by Roh *et al*. [77, 78] was adopted. The estimated electrical resistivity of Au and Cr thin-films was ~20 times larger than the bulk values suggesting that the effective thermal conductivity would be ~20 times smaller than that of bulk. Therefore, these reduced thermal conductivity values were used for the metal thin-films (k_{Au} = 16.0 W/m·K, k_{Cr} = 4.7 W/m·K). Further, the thermal conductivity of SiN_x (k_{SiNx}) was assumed to be ~2.0 W/m·K [79].

To compute the thermal conductance of the tip-sample contact, the amplitude of the heat current Q through the tip-sample contact was first assumed for a scenario where the sample temperature was oscillating with an amplitude of 1 K and a frequency of 10 Hz ($2f$) then computed the resulting amplitude of temperature oscillations in the Au-Cr thermocouple. Subsequently, this computed amplitude was compared with the experimental result (0.034 K). If the computed value was not very close (within ±1 mK) to the measured result, the computation was iterated with a new value of Q until the computed amplitude was consistent with the experimental result. Once the amplitude of the heat current was estimated, the thermal contact conductance G_c was calculated from the relation $Q = G_c \times (T_s - T_c)$. The thermal contact conductance estimated using this procedure was ~10 nW/K.

3.6 Thermal time constant

The choice of the measurement frequency $2f$ (10 Hz) was determined by measuring the thermal time constant of SThM probes and the power spectral density of the thermoelectric voltage noise. First, the thermal time constant of SThM probes was obtained by measuring the temperature rise of the probe tip at various heating frequencies while the amplitude of electric current was held constant. A normalized temperature response obtained in such an experiment is shown in Figure 3.9c. The measured temperature response is found to be constant until ~10 Hz and decreases monotonically afterwards. The thermal time constant (τ_{th}) of the probe tip is defined as $\tau_{th} = 1 / (2\pi f_R)$, where f_R is the roll-off frequency that is defined as the frequency at which the normalized temperature amplitude is $1/\sqrt{2}$. Because the roll-off frequency of the probe is ~40 Hz as shown in Figure 3.9c, the thermal time constant of the probe is ~4 ms. In order to confirm that the measured frequency response is consistent with the device geometry and the estimated tip-sample thermal contact resistance, the experimental results were also analyzed using a time dependent finite difference modeling. The modeled result is represented along with the measured frequency response in Figure 3.9c and agrees well with the experimental result.

In order to obtain the signal to noise (S/N) ratio, the noise in thermoelectric voltages (V_N) of the Au-Cr thermocouple was measured in a configuration where the probe tip is in-contact with an unheated Pt line. The measured thermoelectric voltage noise is converted into an equivalent temperature noise (ΔT_N) using the known effective Seebeck coefficient of the Au-Cr thermocouple determined in section 3.3 ($\Delta T_N = V_N / S_{Au\text{-}Cr}$). The power spectral density (PSD) of the thermoelectric voltage noise is represented in Figure 3.9d and features the increased noise as decreasing frequencies. The signal to noise ratio (S/N) at various frequencies was obtained by first fitting polynomial curves to

temperature signals (Figure 3.9c) and the PSD of the thermoelectric voltage noise (Figure 3.9d), then subsequently dividing temperature signals by the noise obtained from the PSD in a bandwidth of ~0.26 Hz (the same bandwidth used in obtaining temperature signals shown in Figure 3.9c). The calculated S/N is shown in the inset of Figure 3.9d and features a peak in S/N at the frequency of ~10 Hz (2*f*) suggesting that the optimal modulation frequency for thermal imaging is ~10 Hz.

3.7 Demonstration of quantitative temperature measurements

In order to demonstrate quantitative temperature measurement capabilities of UHV-SThM, the temperature profile of sample surfaces was directly measured in a direction perpendicular to a heated Pt line by performing line-scans as shown in Figure 3.11a (a 1 μm wide Pt line whose temperature amplitude of 3 K was oscillating at 10 Hz) and compared with a temperature profile obtained from a FEM calculation represented in Figure 3.5. In this modeling, the values of thermal conductivity were assumed as follows: Si (150 W/m·K) [80], SiO_2 (1.4 W/m·K) [80], Al_2O_3 (1.0 W/m·K, amorphous Al_2O_3 has a low thermal conductivity) [74] and Pt (29.5 W/m·K, thin-film platinum has lower thermal conductivity than that of bulk) [81] respectively. Heat transfer by convection and radiation between the sample and surroundings were all neglected for the computation simplicity. As boundary conditions, the temperature of the bottom surface of Si substrate was set to 300 K, and all other surfaces were set to be thermally insulated. Finally, the amplitude of sinusoidal volumetric heating (oscillating at 10 Hz) of the Pt line was adjusted such that the amplitude of temperature oscillations of the Pt line was in correspondence with the amplitude of measured temperature oscillations. Figure 3.11b shows the topographical profile of the Pt line along with the measured and the modeled temperature profiles, which are in excellent agreement with each other suggesting that

UHV-SThM can quantitatively measure temperature fields. This result is particularly significant because it is in strong contrast to conventional SThM performed by others under the ambient [67] where large discrepancies between the measured and the modeled temperature profiles were observed.

In addition to measuring the temperature profile of a 1 μm wide Pt line, that of a 200 nm wide Pt line was also studied whose temperature amplitude of 6 K was oscillating at 10 Hz. Specifically, line-scans were conducted in a direction perpendicular to the 200 nm wide Pt line at two different scan rates: one scan was performed slowly (at a speed of ~50 nm/s) whereas the other scan was performed at a faster rate (at a speed of ~200 nm/s), which was comparable to the scan rate of the experiment performed on the 1 μm wide Pt line. The temperature profiles obtained in the slow and fast scans are shown in Figure 3.11c and d respectively along with the topographical profile of the Pt line and the modeled temperature profile. The measured data shown in Figure 3.11d (in the fast scan case) were found to be in excellent agreement with the computed temperature profile. However, the data obtained in the slow scan case show features that deviate significantly from the computed temperature profile near the line edge. This deviation from the modeled temperature profile can be understood by noting that sudden changes in the contact area between the tip and the sample occurs when the probe tip moves spatially from the top of the Pt line located near the edge to a neighboring point on the dielectric surface or vice versa (the inset of Figure 3.11c). This change in the contact area results in a corresponding change in the thermal resistance between the tip and the sample resulting in a spurious measurement. However, these features are not visible in the fast scan case due to the spatial averaging of measured temperature signals: such edge effects have been also observed by others in past SThM studies performed in the ambient [65, 76]. The results shown in Figure 3.11 unambiguously demonstrate that UHV-SThM is capable of

performing quantitative temperature measurements; however deviations from the actual temperature can occur when the probe scans near the line edge.

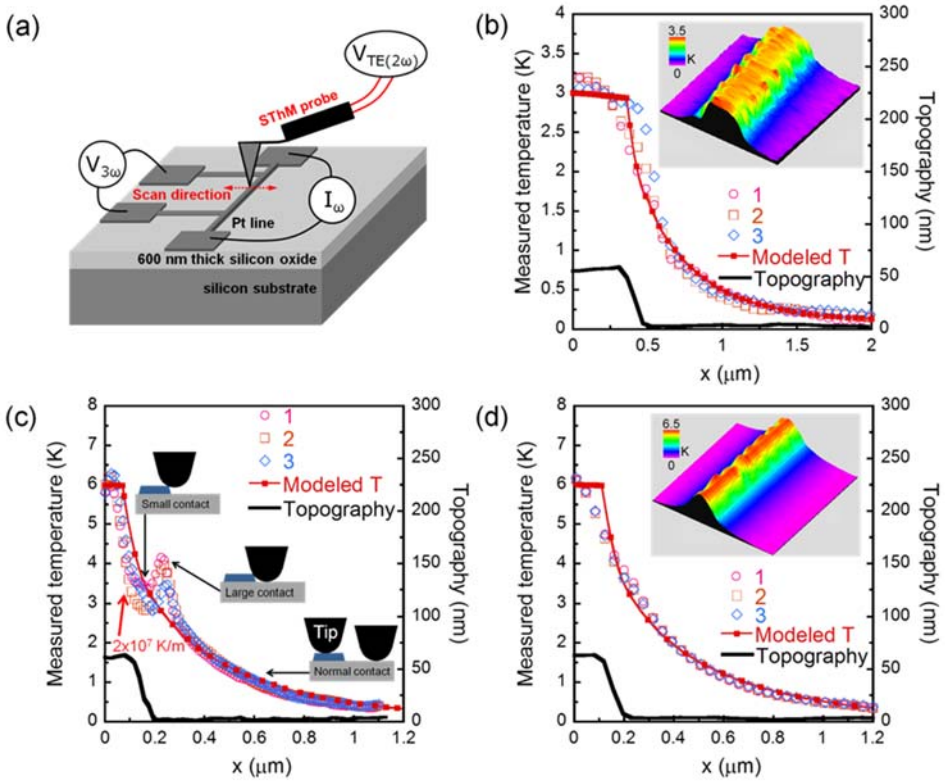

Figure 3.11: (a) Schematic of the experimental setup used to demonstrate the capability of quantitative temperature measurements. Temperature fields and the topography of a heated Pt line sample are simultaneously obtained by scanning in a direction perpendicular to the Pt line. (b) Topographical profile of a 1 μm wide Pt line along with the measured and the modeled temperature profiles. The inset depicts a three-dimensional map of the measured temperature fields. (c, d) Temperature profiles obtained in the slow and the fast scan cases respectively along with the modeled temperature profile and the topographical profile of a 200 nm wide Pt line. The inset of (c) depicts contact conditions between the tip and the sample while scanning measurements. Whereas, the inset of (d) depicts a three-dimensional map of the measured temperature fields. (Panels reproduced from the author's work of Ref. 14.)

3.8 Demonstration of thermal imaging

Since the Au-Cr thermocouple is integrated into the SThM probe tip, it is possible to obtain both the topographical and the thermal images simultaneously. To demonstrate this capability a region where a 200 nm wide Pt line (through which an electric current is

flowing) is connected to a 1 μm wide Pt line (probe leads through which no electric current is passing, Figure 3.12) was studied. Figure 3.12b shows the topography of the region of interest, whereas Figure 3.12c represents the measured temperature fields. As can be seen from Figure 3.12c, the temperature rise of the 200 nm Pt line is lower in the region where it intersects the 1 μm wide Pt line because the wider Pt line acts as a thermal fin. Further, temperature fields in the sections of 200 nm and 1 μm wide heated Pt lines were also studied as shown in the insets of Figure 3.11b and d. The obtained thermal images show the feature that the amplitude of temperature oscillations decays rapidly when the probe scans away from heated Pt lines as expected in the thermal modeling.

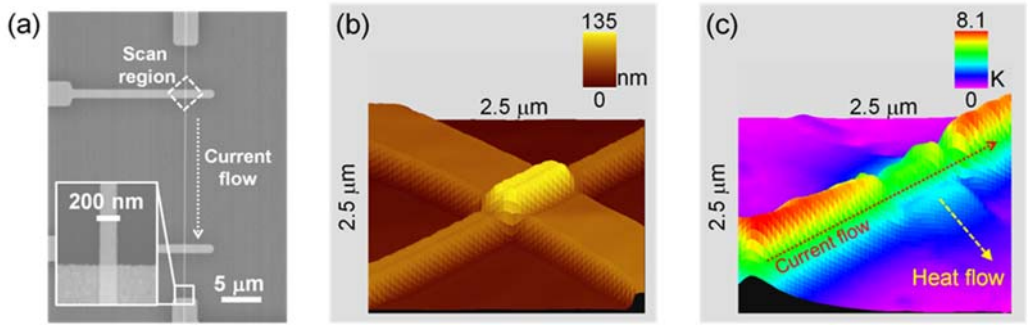

Figure 3.12: (a) SEM image of a 200 nm wide Pt line connecting to a 1 μm wide Pt line. (b) Topographical image of a 2.5 μm × 2.5 μm region represented as the dotted line in (a). (c) Thermal image of the same region shown in (b). The temperature rise of the 200 nm Pt line is lower in the region where it intersects the 1 μm wide Pt line because the wider Pt line acts as a thermal fin. (Panels reproduced from the author's work of Ref. 14.)

3.9 Temperature and spatial resolutions of UHV-SThM

The temperature resolution of UHV-SThM can be estimated from knowledge of the PSD of the thermoelectric voltage noise of the Au-Cr thermocouple (Figure 3.9d) and the measured sensitivity of SThM probes (0.034 K/K). From the measured PSD, the noise at the measurement frequency $2f$ (10 Hz) was found to be ~1 $\mathrm{mK}/\sqrt{\mathrm{Hz}}$ (Figure 3.9d). This

implies that in the measurement bandwidth (0.26 Hz) the root mean square noise of temperature signals (ΔT_N) is ~0.5 mK. Therefore, the noise limited temperature resolution ($\Delta T_{resolution}$ = ΔT_N / Sensitivity) can be estimated to be ~15 mK. The sensitivity of the measurements can be improved further by choosing a smaller measurement bandwidth. However, such a reduction greatly increases the scanning time making it infeasible to dramatically reduce the measurement bandwidth.

The spatial resolution of UHV-SThM is related to the largest temperature gradient ($\left|\vec{\nabla}T\right|_{max}$) that can be measured. Specifically, the spatial resolution (Δr) can be defined as $\Delta r = \Delta T_{resolution} / \left|\vec{\nabla}T\right|$. It can be seen from Figure 3.11c that the temperature gradient as large as 2×10^7 K/m can be measured while scanning the probe from the center to the edge of a heated 200 nm wide Pt line. From this measured temperature gradient, the spatial resolution of UHV-SThM can be estimated to be ~1 nm. However, this estimation needs to be interpreted with caution because the contact diameter of the point contact is ~10 nm resulting in a reduction of the spatial resolution due to the averaging effects. Therefore, practically the spatial resolution of UHV-SThM is ~10 nm—this value still represents the highest spatial resolution among all nanoscale temperature measurement techniques reported until now.

3.10 Summary

To summarize, in this chapter a scanning thermal microscopy technique capable of a spatial resolution of ~10 nm and a temperature resolution of ~15 mK was demonstrated. These high resolutions were achieved by using nanofabricated AFM probes with an integrated nanoscale thermocouple operating in an ultra-high vacuum environment. The quantitative temperature measurement capabilities of this technique were also demonstrated by directly imaging temperature fields in the vicinity of a 200 nm wide

heated Pt line intersecting a 1 μm wide unheated Pt line. Further, the measurement results are found to be in excellent agreement with the computational results—unambiguously demonstrating quantitative temperature measurement capabilities. Given its superior spatial and temperature resolutions, UHV-SThM is well suited for the studies of nanoscale thermal transport and will play an important role in understanding energy dissipation, phonon transport and electron-phonon interactions in various nanoscale electronic and photonic devices. In the work presented in this thesis (in the next few chapters), UHV-SThM was extensively leveraged to obtain the information regarding nanoscale temperature fields.

Acknowledgements: I nanofabricated SThM probes in collaboration with Kyeongtae Kim. I characterized SThM probes and performed scanning measurements along with Kyeongtae Kim and Woochul Lee. I performed the finite element modeling for estimation of probe stiffness, temperature fields and bimaterial effects. Kyeongtae Kim performed the finite difference modeling.

Chapter 4

Thermal effects on electromigration of Au nanowires

4.1 Direct quantification of nanoscale temperature fields

In this chapter, I will present a detailed description of my investigations of thermal effects on electromigration of Au nanowires. Electromigration plays an important role in the degradation of nanoscale devices. Further, it also plays a key role in the EBJIH devices that I developed for studying thermoelectric phenomena in MMMJs (details in Chapter 5). Therefore, I carefully studied the impact of Joule heating on electromigration using the UHV-SThM technique described in the previous chapter.

Understanding heat dissipation (Joule heating) and energy transport in nanoscale devices is critical for realizing novel nanoscale functional devices [54, 82, 83]. In fact, Joule heating is widely expected to play an important role in electromigration induced device failures: a process where metal atoms in a device are displaced due to the momentum transfer between charge carriers and the lattice [48, 84-93]. Electromigration in functional devices is always accompanied by Joule heating, which accelerates the electromigration process by affecting the mobility of metal atoms and is well known to limit the operating voltages and the reliability of the devices [82, 84, 94]. Recently, electromigration has also been leveraged to create novel nanoscale electronic and memory devices [51, 95, 96]. In spite of the importance of Joule heating in

electromigration and the extensive previous studies on the electromigration process, it has not been possible to quantify temperature fields in nanoscale devices during electromigration. However, such knowledge is critical for both increasing the reliability of nanoscale devices and creating functional devices that take advantage of electromigration.

Several research groups have indirectly estimated the local temperature changes that arise during the electromigration process [87-89, 91, 97]. These studies have provided valuable insights that have guided the development of molecular electronic devices leveraging electromigration for trapping molecules. However, in spite of the broad impact of electromigration on nanoelectronic devices, a direct measurement of local lattice temperature during electromigration has remained elusive due to experimental challenges in performing quantitative nanoscale temperature measurements. In this work, I exploited UHV-SThM [14] to quantify temperature fields in prototypical bow-tie shaped Au nanowires (Figure 4.1a) that are widely used in molecular electronics for creating electromigrated break junction based molecular devices [1, 51, 98] and in plasmonics for obtaining local enhancements in electric fields [99, 100].

To measure local temperature of the devices, a custom nanofabricated scanning probe with an integrated thermocouple, in contact mode, was used. Specifically, temperature measurements were performed in two different schemes: (a) an unmodulated scheme (DC scheme) where temperature fields are not periodically modulated and (b) a modulated scheme (AC scheme) where temperature fields are periodically modulated at a frequency of 10 Hz (2*f*). The DC scheme enables fast temperature measurements while achieving a somewhat lower temperature resolution (~2 K). Whereas, the AC scheme requires a relatively longer time (~85 minutes) to map temperature fields but enables higher spatial (~10 nm) and temperature (~15 mK) resolutions (The details of two schemes will be discussed in section 4.2 and 4.3). By employing these two schemes, experiments were

performed to obtain detailed information regarding both the temperature rise of local hot spots where electromigration is initiated and the spatial variations of temperature fields in nanoscale devices during electromigration.

The schematic of the experimental setup is shown in Figure 4.1a. The bow-tie shaped nanowires (~225 nm wide and ~450 nm long) were defined by e-beam lithography and evaporation (40 nm thick Au) on a Si wafer with a 500 nm thick thermally grown SiO_2 layer. Subsequently, the source and drain electrodes were defined by photolithography and evaporation (3/70 nm thick Ti/Au) in order to ensure good electrical contact with the Au nanowires. In order to carry out thermal studies during electromigration the bow-tie samples were placed in a UHV chamber, and all experiments were performed in UHV ($<10^{-9}$ torr) at room temperature (~300 K) or at a low temperature (~100 K).

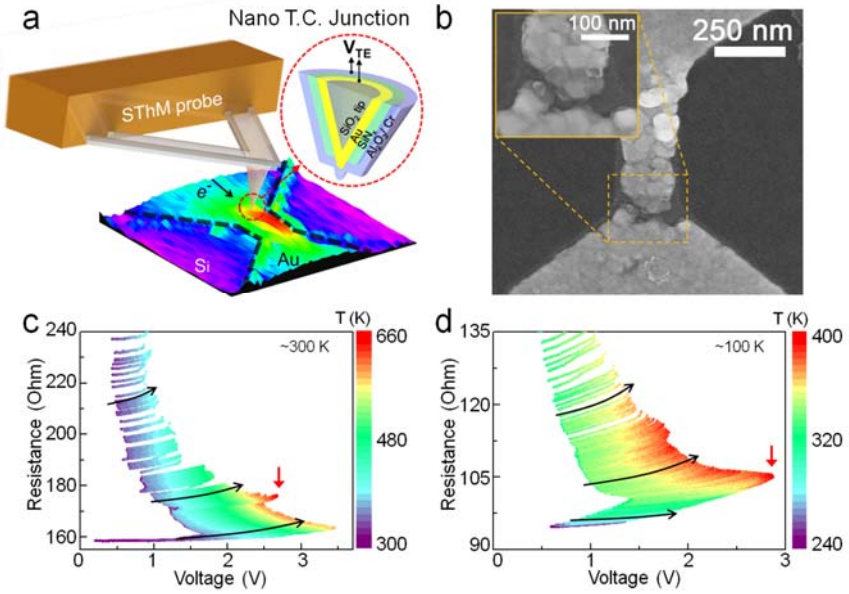

Figure 4.1: (a) Schematic of UHV-SThM used in this work. (b) Representative SEM image of a nanogap junction after the electromigration process. (c) Representative two-dimensional color plot that captures the resistance changes and local temperature rise of a device when it is subjected to a cyclic voltage application (represented by black arrows) at room temperature (~300 K). The measured local temperature rise is color coded. The point at which the maximum temperature is attained is indicated by the red vertical arrow. (d) Same as (c) but for a low temperature (~100 K) measurement. (Panels reproduced from the author's work of Ref. 53.)

In order to perform electromigration a process originally developed by others [87, 90, 101] was employed. Briefly, a cyclic voltage was applied to the Au nanowires of the bow-tie structure (Figure 4.1c and d) while the electrical resistance of the nanowires was continuously monitored. The applied voltage was linearly ramped up in steps of 5 mV every 100 ms until the nanowire resistance increased by 1 – 5%. This threshold value was manually controlled depending on the monitored resistance of the nanowires. Upon detection of a desired increase in the resistance, the voltage bias was rapidly ramped down. The resistance of the devices increased irreversibly as electromigration proceeded; this is in contrast to reversible changes in the resistance due to temperature changes. This process was continued until the electromigration process was completed resulting in a nanoscale gap in the bow-tie devices as shown in Figure 4.1b. The formation of a nanoscale gap is readily recognized by a rapid increase in the resistance.

4.2 Local temperature measurements with the DC scheme

To measure the local temperature rise of the Au nanowires during the electromigration process, a SThM probe was first placed in the mechanical contact at a contact force of 150 ± 25 nN with a bow-tie device, on the cathode side (i.e. the electrode from which electrons enter the nanowire) at a point that is ~100 nm away from the region where the cathode meets the nanowire (Figure 4.2a). This location is well suited because: 1) it is sufficiently close to the nanowire to record the temperature that is representative of the local temperature rise of the nanowire, 2) this is the region where the temperature rise is the largest after electromigration (will be discussed in section 4.3), and 3) the measured temperature signals are not affected by the electromigration induced topographical changes of the devices. The temperature rise of the nanowires was recorded via the nanoscale thermocouple integrated into the probe tip while a cyclic voltage was applied

to the bow-tie devices to initiate electromigration. As the nanowires are electromigrated, the temperature of the devices changes, which results in thermoelectric voltages at the nanoscale thermocouple. In this experiment, thermoelectric voltages were first amplified by a voltage preamplifier (gain of 1000) and then low-pass filtered at 30 Hz to obtain desired temperature signals. This enables a direct in-situ measurement of the local temperature rise of the devices during electromigration. Thermoelectric voltages of the integrated thermocouple (ΔV) are related to the local temperature rise (ΔT) by $\Delta T \times \beta = |\Delta V| / S_T$, where S_T = 16.3 ± 0.1 μV/K [14] is the effective Seebeck coefficient of the nanoscale thermocouple, and β = 0.083 ± 0.006 K/K is the sensitivity of the probe (Figure 4.3). The obtained sensitivity is ~2.5 times larger than that was reported in Chapter 3. This increased probe sensitivity is understood by the presence of an additional insulating layer of Al_2O_3 on the outermost surface of SThM probes, which is intended to prevent possible electrical shorts between the sample and the probe during extensive scanning measurements but results in an increase of the contact size. Further, it is noticeable that the sensitivity of the probe does not change in the DC measurement case as the frequency response of the probe is invariant until ~10 Hz [14].

Figure 4.1c shows a two-dimensional color plot of the measured local temperature rise and the evolution of the electrical resistance as an applied voltage is cycled at room temperature (~300 K). Data obtained in a similar experiment performed at a lower temperature (~100 K) are shown in Figure 4.1d. Since the thermal time constant of SThM probes is sufficiently small (<100 ms) [14] they track the variations in the local temperature rise with high fidelity. It can be seen from Figure 4.1c and d that the maximum temperature rise during electromigration in both the high and low temperature measurements occurs when the resistance changes by ~10%. Specifically, the maximum local temperature rise was ~660 K for the experiment performed at room temperature and ~400 K for the experiment performed at a low temperature, which were measured at the

location aforementioned. From the data shown in Figure 4.1c and d, it is clear that the overall trends of local temperature rise during electromigration are relatively independent of the ambient temperature. However, the maximum temperature rise during electromigration is significantly smaller in low temperature measurements—this represents important information that can be leveraged to create molecule-based devices where a large increase in the local absolute temperature is detrimental to the stability of molecules [97].

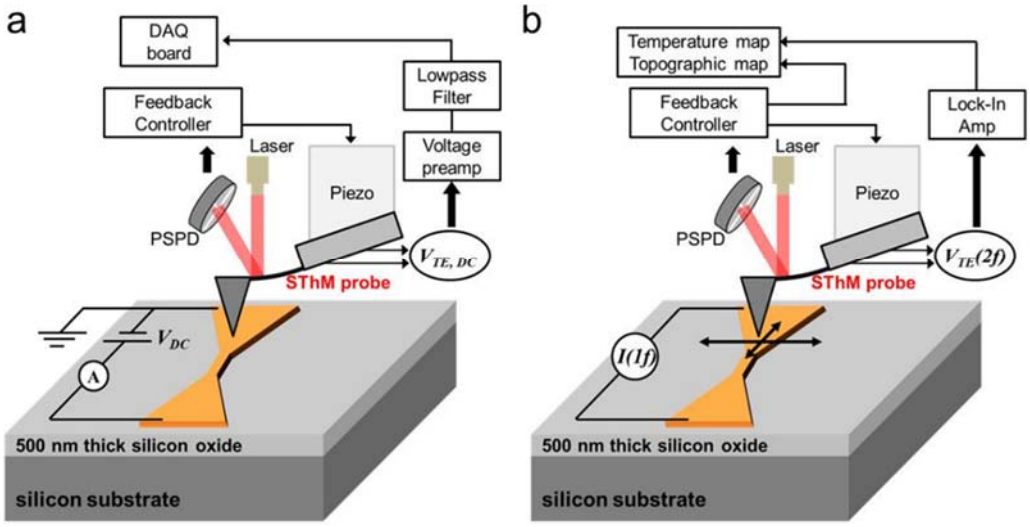

Figure 4.2: Schematic of DC and AC schemes. (a) In the DC scheme, a SThM probe was placed in the mechanical contact with a sample (at a constant contact force of 150 nN) at ~100 nm away from the region where the cathode meets the nanowire. Thermoelectric voltages from the integrated thermocouple were constantly monitored while the bow-tie shaped Au nanowire was electromigrated. (b) In the AC scheme, a sinusoidal electric current at 1*f* (5 Hz) was applied to a device, which resulted in temperature amplitude oscillations at 2*f*. As a SThM probe scanned over the bow-tie device with a constant contact force, temperature amplitude oscillations (thermoelectric voltages) at 2*f* were recorded using a lock-in amplifier in a bandwidth of ~0.5 Hz. The topographic information was also simultaneously obtained by monitoring deflections of the probe cantilever. (Panels reproduced from the author's work of Ref. 53.)

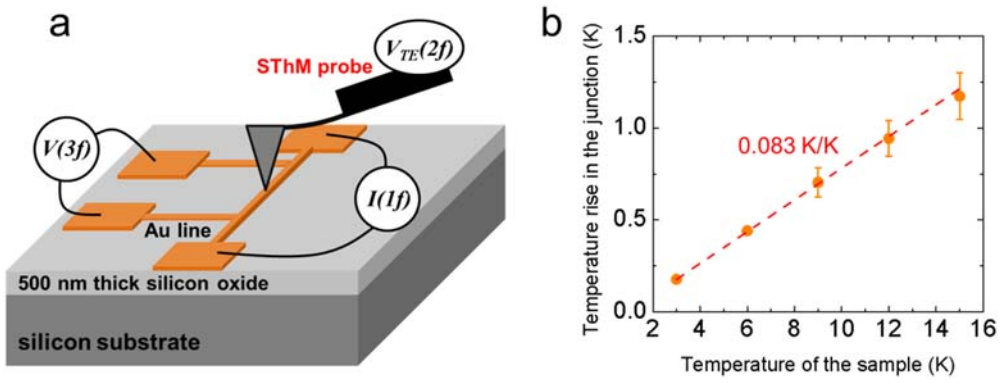

Figure 4.3: Characterization of the sensitivity of SThM probes. (a) Schematic of the experimental setup used to measure the sensitivity of the probe. (b) Measured temperature amplitude oscillations of the integrated thermocouple as a function of the temperature amplitude oscillations of a heated Au line. (Panels reproduced from the author's work of Ref. 53.)

An important question to address in this context is: What is the local temperature rise of hot spots at which electromigration is actually initiated? In order to answer this question, it is instructive to present the data shown in Figure 4.1c and d in a different form that enables visualization of the relationship between the resistance changes and the temperature rise. Therefore, in Figure 4.4 the measured temperature rise is presented as a function of the device resistance during electromigration. In Figure 4.4a it can be seen that before electromigration is initiated the temperature rise increases approximately linearly with the resistance. This should be expected because for a metallic wire the relationship between the temperature rise (ΔT) and the resistance (R) is given by $R = R_0 \times (1 + \alpha\Delta T)$, where R_0 is the wire resistance when ΔT is zero, and α is the temperature coefficient of resistance (TCR) of the wire. This implies that $dT/dR = 1/\alpha R_0$, therefore if αR_0 changes the slope (dT/dR) becomes non-linear. As mentioned above, in Figure 4.4a the temperature rise and the power dissipation traces overlap each other and show a linear dependence on the nanowire resistance because the resistance change is dominated by Joule heating. The range where this linear relation appears is marked as region i) in Figure 4.4.

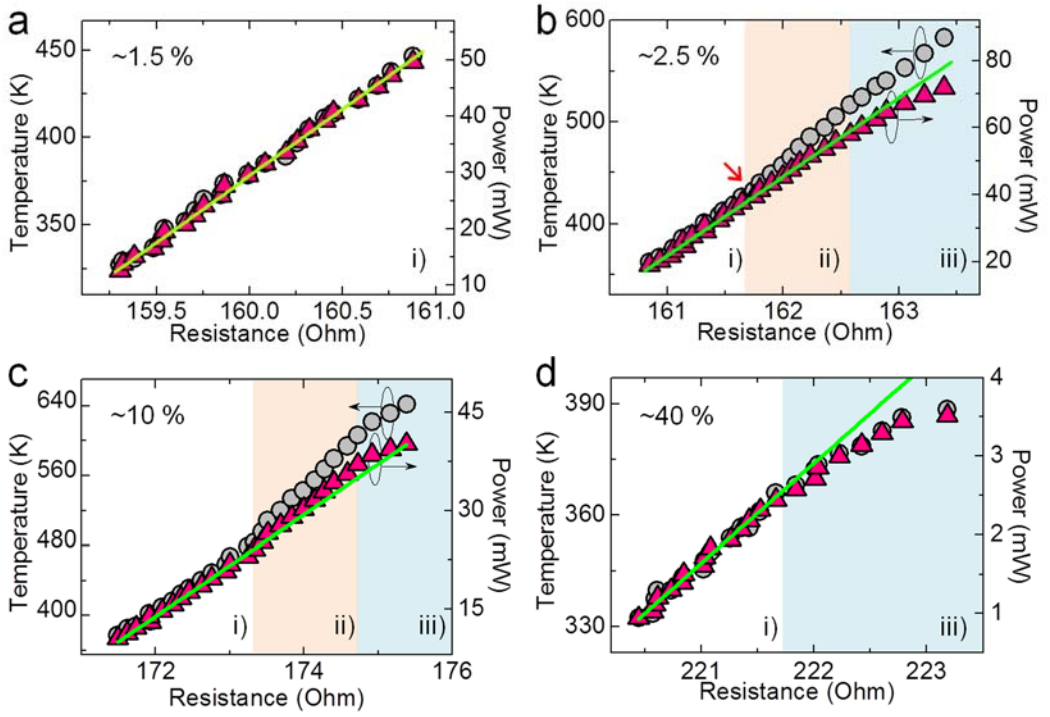

Figure 4.4: Local temperature rise during the electromigration process. (a) – (d) Traces relating both the temperature rise and the power dissipation to the device resistance during electromigration. The traces were obtained at various stages of electromigration where the device resistance increased by 1.5%, 2.5%, 10% and 40% respectively, in comparison with the device resistance before initiating the electromigration process. (Panels reproduced from the author's work of Ref. 53.)

In contrast, for the devices where the resistance had irreversibly changed by 2.5% or 10% (Figure 4.4b and c), the relationship between the temperature rise and the resistance as well as the power dissipation and the resistance were found to be non-linear. The onset of the nonlinearity in the relationship between the temperature rise and the resistance is highlighted by the red arrow in Figure 4.4b and indicates the point at which electromigration is initiated, when the local temperature rise of the nanowire reached ~430 K. Similar analysis of the data obtained in low temperature measurements indicate that electromigration is initiated at ~315 K. Further, from FEM simulations I estimated that the temperature rise (before electromigration) at the middle of the nanowire is ~20% larger than what measured at the location aforementioned as shown in Figure 4.5. This

implies that the local temperature rise at hot spots when electromigration initiates is ~520 K in room temperature measurements and ~380 K in low temperature measurements. These values are larger than those reported by others in previous studies [89, 97]. This discrepancy can be attributed to the indirect way in which previous temperature measurements were performed that resulted in a spatial averaging of the device temperature rise, which is lower than the local temperature rise at hot spots. These results clearly show that electromigration is indeed initiated at temperatures much lower than the melting temperature of Au (~1337 K) [102]. In addition, from the data shown in Figure 4.4b and c, it is clear that immediately after the initiation of electromigration both the resistance and the slope of the temperature rise (dT/dR) increase implying that TCR decreases (indicated as region ii)). This observed decrease in TCR is hypothesized to occur due to the creation of voids that results in a reduced electron mean free path, which is known to suppress TCR [103]. It can be also seen in Figure 4.4b and c that at larger temperature rises, which correspond to higher voltage biases (marked as region iii)), the slope of the temperature rise (dT/dR) and the power dissipation (dP/dR) curves decrease simultaneously. This can be understood by noting that an increased electrical resistance due to voids accumulation reduces the overall Joule heating in the device. This behavior was also observed in Figure 4.4d for the device where the resistance had changed by 40%.

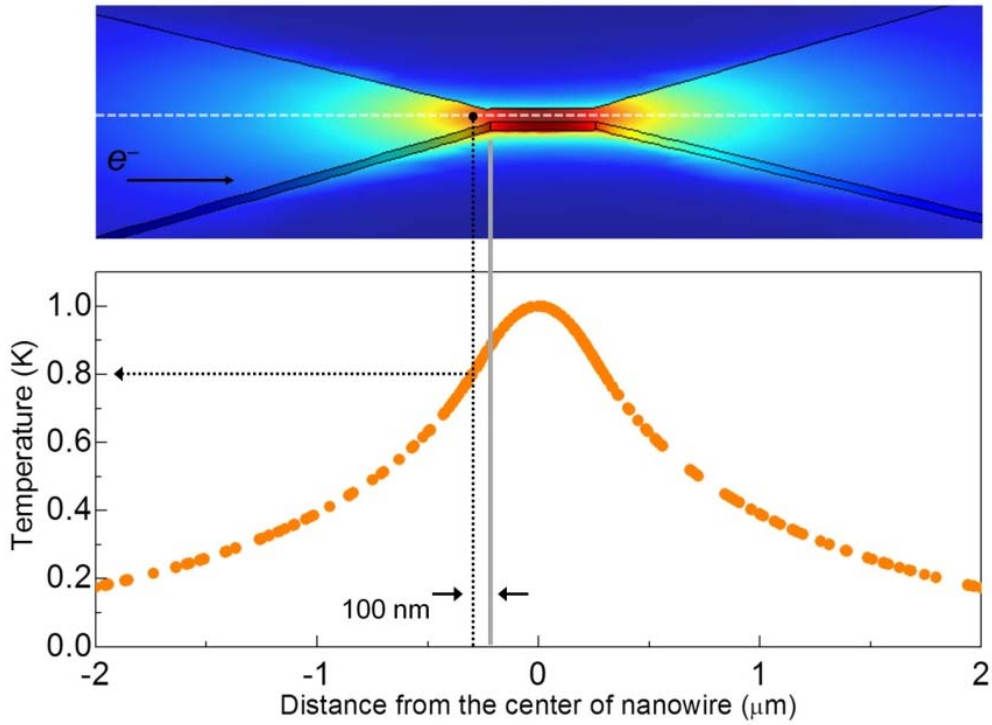

Figure 4.5: Finite element modeling of the temperature field in an as-fabricated device. The calculated temperature profile of the device shows that the temperature rise of the point at which the measurements of local temperature rise were performed (indicated by the black dot) is ~20% lower than the maximum temperature rise of the device, which occurs at the middle of the nanowire before electromigration initiates. (Figure reproduced from the author's work of Ref. 53.)

4.3 Temperature fields mapping with the AC scheme

In order to obtain further insights, additional experiments were performed where the electromigration process was first terminated at certain representative states (the resistance of the devices had increased by 2.5%, 10% and 40% respectively). Subsequently, the topographical image as well as temperature fields of the devices were mapped under a small sinusoidal bias voltage with an amplitude <0.3 V and a frequency of 5 Hz (1*f*) as shown in Figure 4.2b. The applied voltage bias was sufficiently small that no further electromigration occurs during the thermal characterization. The topography was obtained in contact mode at a contact force of 150 ± 25 nN while temperature fields were mapped by locking in to the second harmonic component (10 Hz) of thermoelectric

voltages from the integrated thermocouple [14]. The time constant of the lock-in amplifier (SR 830) was chosen to be 300 ms and the scan speed was chosen to be 40 seconds per line (128 lines in total for each thermal map, thus it takes ~85 minutes to obtain each temperature field).

The obtained topography for a Au nanowire when the resistance of the device had changed by 0%, 2.5%, 10% and 40% are shown in Figure 4.6a – d respectively. The measured topography unambiguously shows the formation of hillocks and depressions, which mostly emerged at an early stage of the electromigration process where the resistance increase was <10%. The corresponding temperature fields are shown in Figure 4.6e – h, which highlight an important feature: an increase in the asymmetry of temperature fields upon electromigration. Specifically, before electromigration temperature fields are symmetrical about the center line (the dotted line) with the maxima of temperature fields being located in the middle of the nanowire. However, as electromigration progresses and results in a 40% resistance change, temperature fields become increasingly asymmetric with the temperature rise being larger at the intersection of the nanowire and the cathode. The color codes used in Figure 4.6e – h and 4.6m – p represent normalized temperature rise with red being hotter than blue. The increase in the asymmetry of temperature fields can be qualitatively understood by hypothesizing that voids are created and primarily accumulated in the cathode of the device, which will be discussed in section 4.4 with a simple model. This hypothesis is consistent with previous studies by others that observed voids accumulation in nanoscale devices [85, 88, 89, 92, 93, 104].

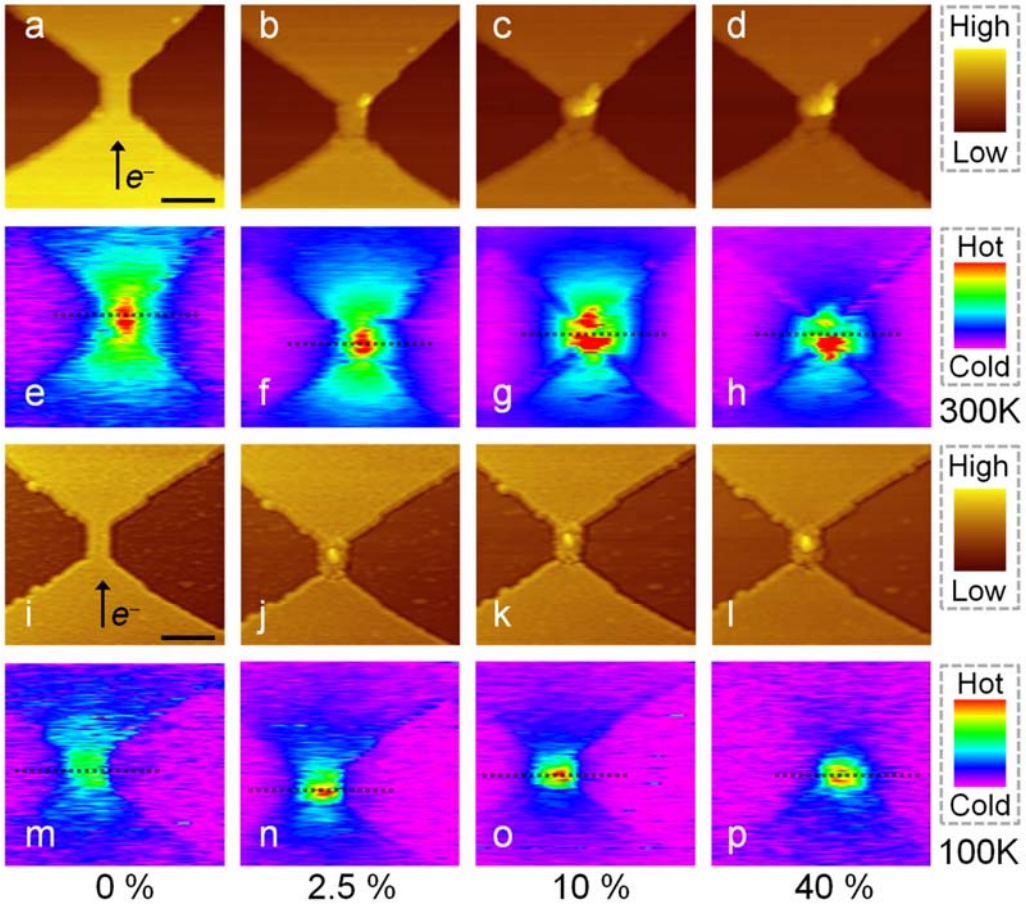

Figure 4.6: Topographic and thermal images during electromigration. (a) – (d) and (i) – (l) Topography of nanowire devices at various stages of electromigration performed at room temperature (~300 K) and a low temperature (~100 K), respectively. (e) – (h) and (m) – (p) Thermal images obtained under a small sinusoidal bias at ambient temperatures (or minimum temperatures) of ~300 K and ~100 K, respectively. The maximum temperatures of (e) – (h) and (m) – (p) are 311.4 K, 328.2 K, 385.8 K, 346.8 K, 108.2 K, 111.9 K, 122.2 K and 115.9 K respectively. Temperature fields of Au nanowires were observed to change from symmetrical ((e) – (g) and (m) – (o)) to asymmetrical ((h) and (p)), about the dotted center line, as electromigration proceeded. The direction of the electron flow is indicated by the black arrow. The scale bar corresponds to 500 nm. (Panels reproduced from the author's work of Ref. 53.)

The above results raise an important question: What is the source of the observed asymmetry in temperature fields after electromigration? Is it due to the formation of a notch in the nanowire or caused by a local change in the electrical resistivity resulting from the accumulation of voids, which enhances electron scattering and increases the local temperature rise? In order to answer this question I performed FEM simulations

using COMSOL (Joule heating module). An electric current was simulated through the Au nanowire from the source electrode to the drain electrode, while all other surfaces were electrically insulated. In addition, the temperature of the bottom surface (Si substrate) was modeled to be at 300 K, while all other surfaces were modeled to be thermally insulated. The thermal conductivity and the electrical resistivity of materials were chosen to be 320 W/m·K and 2.2×10^{-8} Ω·m for bulk Au and 160 W/m·K and 4.4×10^{-8} Ω·m for thin-film Au in the bow-tie region [105]. Further, the thermal conductivity of Si and SiO_2 were assigned to be 150 W/m·K and 1.4 W/m·K respectively [80]. In these simulations, I first considered the case where a notch is developed in the nanowire without a change in the local electrical resistivity. When a current density of 1.3×10^{11} A/m^2, which is comparable to that used in the scanning measurements is applied across the nanowire region of such a device, the obtained temperature field from the FEM calculation is shown in Figure 4.7a. It can be clearly seen that the temperature field is largely symmetric highlighting that structural effects alone—i.e. the nanogap formation as the breakdown proceeds—cannot explain the asymmetrical temperature fields observed in the experiments. For comparison, I performed another FEM simulation (Figure 4.7b) where in addition to the notch, the local electrical resistivity of the cathode was increased by a factor of ten to 2.2×10^{-7} Ω·m—to mimic the effects of the accumulation of voids—in the region of the cathode highlighted by the dotted line in Figure 4.7b. It can be seen that the modeled temperature field is asymmetric in correspondence with the experimental observations providing strong support for the hypothesis of voids accumulation in the cathode during electromigration.

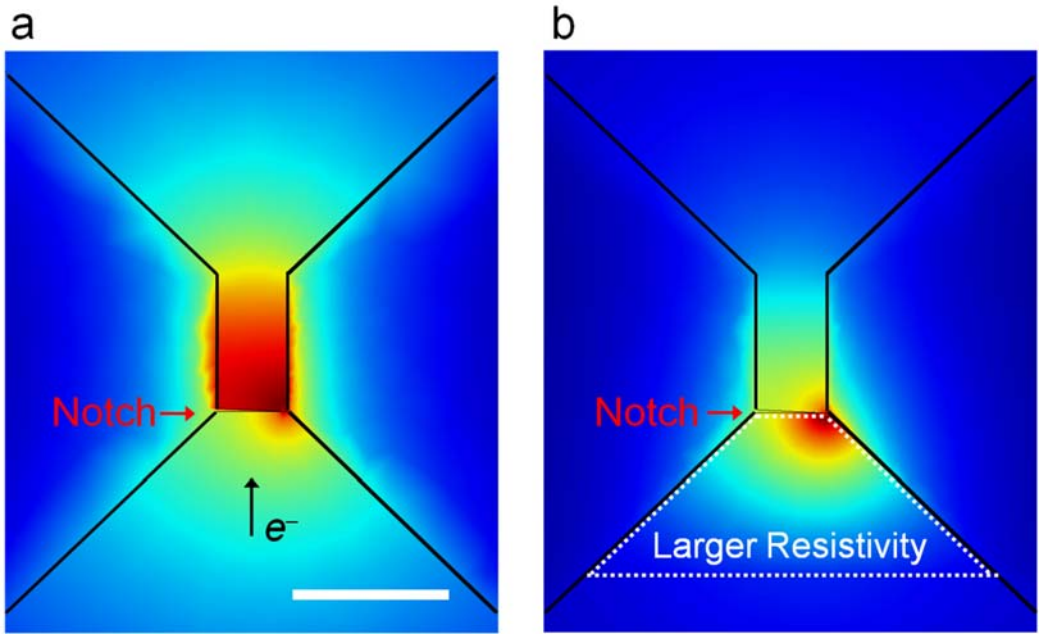

Figure 4.7: Finite element modeling calculations to simulate the effects of structural changes and the increased electrical resistivity. (a) Temperature field obtained from a FEM simulation of a notched nanowire, under an applied voltage bias, shows no appreciable asymmetry. (b) Similar modeling performed for the nanowire with both a notch and a local increase in the electrical resistivity of the highlighted region (marked by the dotted line) of the cathode by ten times (to 2.2×10^{-7} Ω·m). In this case an asymmetrical temperature field is observed. The scale bar corresponds to 500 nm. (Panels reproduced from the author's work of Ref. 53.)

Further, thermal imaging measurements performed at a low temperature (~100 K) show similar trends (Figure 4.6m – p). However, in this case the asymmetry in temperature fields is less prominent than that performed at room temperature. These results can be partly understood by noting that the mobility of Au atoms is lower at ~100 K than that at room temperature, which requires a larger current density for initiating electromigration as experimentally observed. It is expected that this large current density creates voids both in the cathode and in the nanowire leading to a less asymmetrical temperature field. In spite of this reduced asymmetry, the location of nanogap formation still showed the same bias-polarity dependence, i.e. voids accumulated primarily in the cathode.

Finally, the topographical and thermal imaging studies were limited to the devices whose resistance has changed by 40% or less because the voltage bias required for obtaining appreciable temperature fields increases with the device resistance. In general, large applied voltage biases tend to induce electromigration making it extremely difficult to thermally image the devices before the resistance increases further.

4.4 A model to explain preferential nanogap formation in the cathode

It is noticeable that in all devices studied in this work the nanogap is preferentially created in the cathode after electromigration. This behavior can be qualitatively understood using a relatively simple model. The conservation of mass during the electromigration process implies that [89, 106]:

$$\frac{\partial n}{\partial t} + \left(\nabla \cdot \vec{J}\right) = 0 \tag{4.1}$$

where n is the local number density of atoms and $\vec{J} = \overrightarrow{J_E} + \overrightarrow{J_S} + \overrightarrow{J_T}$ is the local atomic flux. Here $\overrightarrow{J_E}$, $\overrightarrow{J_S}$ and $\overrightarrow{J_T}$ are the local atomic fluxes induced by electric field, back stress and temperature gradients, respectively [89, 106]. Equation 4.1 can be simplified further by neglecting small variations in the current density along the y-direction (Figure 4.8b) to give:

$$\frac{\partial n(x,t)}{\partial t} + \frac{\partial J_x}{\partial x} = 0 \tag{4.2}$$

where $n(x, t)$ is the local number density of atoms at a position x, and J_x is the x-component of the local atomic flux. It is known that after the initiation of electromigration $\overrightarrow{J_E}$ dominates over all other components ($\overrightarrow{J_S}$ and $\overrightarrow{J_T}$) [89, 106]. Thus,

under this approximation $\vec{J} \approx \overrightarrow{J_E}$. Further, J_x can be related to the x-component of the local current density j_x by:

$$J_x \approx J_{E,x} = \frac{eZ^* n(x,t) D \rho(x,t)}{k_B T} j_x \tag{4.3}$$

where eZ^* is the effective charge of metal atoms, $\rho(x, t)$ is the local electrical resistivity of the device, T is the absolute temperature, and D is the local diffusion constant given by:

$$D = D_0 e^{-E_a / k_B T} \tag{4.4}$$

where E_a is the activation energy for the atomic diffusion of Au and is ~0.12 eV [89], and D_0 is a constant. In order to model the local atomic flux, I first computed the temperature profile of an as-fabricated device (before electromigration initiated) using COMSOL. The result of the computed temperature field is shown in Figure 4.8a. This temperature profile was used in conjunction with the simplified one-dimensional model, described by Equation 4.2, 4.3 and 4.4 to compute the time derivative of the local number density of atoms ($\partial n(x, t)/\partial t$) at $t = 0$ along the centerline of the device (Figure 4.8) using a finite difference scheme. The obtained temperature profile was used to compute $J_{E,x}$ at each location of x using Equation 4.3 and 4.4. In this calculation, I assumed that $\rho(x, t = 0) = 4.4 \times 10^{-8}$ Ω·m. Subsequently, I computed $\partial J_x/\partial x$ by the following approximation $\partial J_x/\partial x \approx [J_x(x + \Delta x) - J_x(x)] / \Delta x$, where $\Delta x = 10$ nm. It is worth noting that this one-dimensional model is a good approximation in the nanowire region and in close proximity to the nanowire as both the current density and temperature fields have a very weak y-dependence. Further, the values of $\partial n(x, t = 0)/\partial t$ presented in Figure 4.8b are normalized such that the maximum value of $|\partial n(x, t = 0)/\partial t|$ is equal to 1 for the highest current density, therefore the results are independent of the values of $n(x, t = 0)$ and D_0 in Equation 4.3 and 4.4. The computed results are shown in Figure 4.8b where it can be seen that $\partial n(x, t = 0)/\partial t < 0$ in the cathode signifying a depletion of the number density. In

contrast, $\partial n(x, t = 0)/\partial t > 0$ in the anode implying an increase in the number density. Further, it is noticeable that this asymmetry in the number density is ultimately related to the presence of temperature gradients in the device, in the absence of which Equation 4.2, 4.3 and 4.4 would not predict any accumulation or depletion of atoms in either the anode or the cathode.

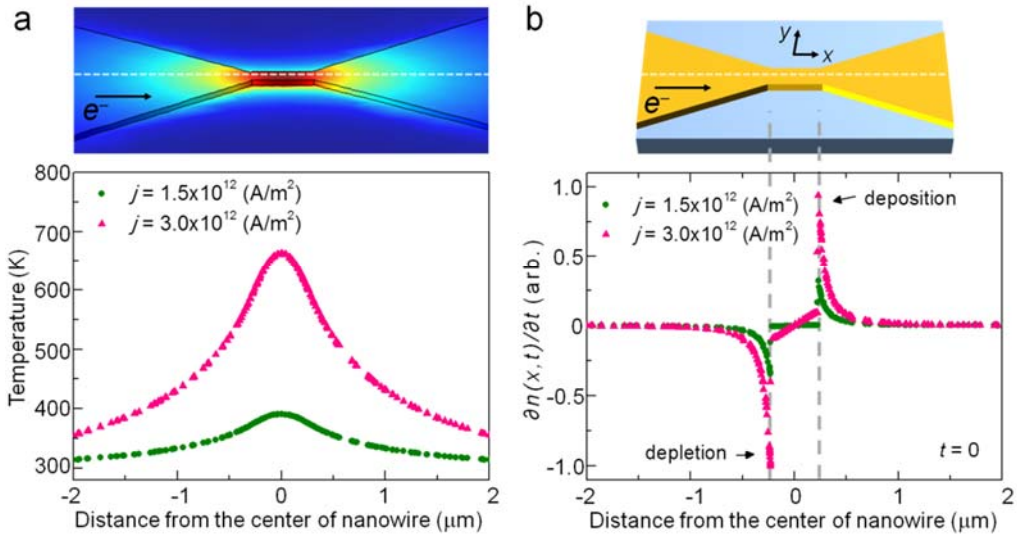

Figure 4.8: Temperature profiles of a nanowire device and the time derivative of the local number density of atoms at $t = 0$ along the centerline of the device. (a) Simulated temperature field (top) and the temperature profiles (bottom) along the centerline (shown by the dotted line) of a bow-tie structure for two different current densities supplied through the device (current densities were estimated using the cross-sectional area of the nanowire ($\sim 10^{-14}$ m^2)). (b) Time derivative of the local number density of atoms at $t = 0$ (bottom) along the centerline (the dotted line) of a bow-tie shaped nanowire (top) obtained for two different current density conditions using a finite difference scheme. Depletion of atoms is seen in the converging region of the cathode, while the accumulation of atoms is observed in the converging region of the anode. (The electron flow direction is indicated by the black arrow.) The region of the plot from –0.225 μm to +0.225 μm corresponds to the nanowire region, and the origin corresponds to the center of the nanowire. (Panels reproduced from the author's work of Ref. 53.)

4.5 Summary

To summarize, temperature fields and topography of Au nanowires during electromigration were studied using scanning thermal microscopy at both room temperature (~300 K) and a low temperature (~100 K). From these measurements, the local temperature rise and the spatial inhomogeneity of the electrical resistivity in the nanowires during electromigration were observed. Specifically, the later information was obtained by thermally imaging the nanowires under a small sinusoidal bias to elucidate the emergence of the asymmetries in temperature fields. It is also found that the maximum absolute temperature at the onset of electromigration can be substantially suppressed by lowering the ambient temperature. Further, the experimental results provide strong evidence for the accumulation of voids in the cathode of the devices during electromigration, which results in preferential nanogap formation on the cathode side. The experimental approach reported in this chapter enables deeper insights into the role of Joule heating in the failure of nanoscale functional devices. Further, this approach can be also applied to investigate a variety of interesting thermal phenomena relevant to many areas of nano-science and technology.

Acknowledgements: I nanofabricated nanowire samples in collaboration with Youngsang Kim. I performed local temperature rise measurements and scanning experiments along with Kyeongtae Kim, Youngsang Kim and Woochul Lee. I performed the thermal modeling. I analyzed the creation of preferential nanogaps via a modeling.

Chapter 5

Electrostatic control of thermoelectricity in molecular junctions

5.1 Introduction

In the beginning of this thesis, I presented arguments for why tuning the electronic structure of molecular junctions can lead to enhance their electronic and thermoelectric properties. The central goal of this chapter is to describe the experimental approach I took to demonstrate that such enhancements were indeed possible. Specifically, I will describe the novel approach that I developed to unambiguously demonstrate that the thermoelectric properties of molecular junctions can be enhanced by controlling their electronic structure.

Note that charge transport in molecular junctions (MJs) has been extensively studied in both two-terminal [11, 12, 45, 54, 107, 108] and three-terminal configurations [1, 4, 50, 51, 109, 110] as MJs are excellent candidates for testing quantum transport theories [2, 111, 112] and due to their significant promise for reaching the ultimate limit of device miniaturization [111]. Experimental efforts [13, 113-118] have also accomplished two-terminal measurements of the thermoelectric properties to obtain insight into the nature of the dominant charge carriers in MJs. Key to obtaining both deeper insights and the optimization of the thermoelectric properties in MJs is the ability to tune their charge transmission characteristics at the chemical potential (E_F), as their thermoelectric

properties are controlled by the magnitude and the derivative of the transmission at E_F [8, 119]. Although recent pioneering work [1, 4, 51, 109, 110] has established the feasibility of actively tuning charge transmission characteristics of MJs, by creating three-terminal devices that feature an additional gate electrode, thermoelectric measurements in such three-terminal configurations have not been achieved. This inability is primarily due to major experimental challenges in establishing temperature differentials across the source and drain electrodes of MJs and has severely impeded the ability to test several important theoretical and computational predictions [6, 33, 120].

In order to overcome this barrier, I performed extensive thermal modeling to conceive a design (Figure 5.1a) that offers adequate thermal resistance between the source and drain electrodes for establishing desired temperature differentials. Specifically, in the design an electrical heater, which is insulated from other leads, is integrated in close proximity to a gold (Au) nanowire. Further, a thin (~7 nm) aluminum (Al) gate electrode is located beneath the Au nanowire and is electrically isolated from it via a 10 nm thick silicon nitride (SiN_x) dielectric layer (see Chapter 2 for details). The continuum-level thermal modeling, performed using the finite element method (COMSOL), suggested that when heat is dissipated in the heater and a nanoscale gap is created in the Au nanowire, a temperature differential can be readily established across the nanogap (the solid lines in Figure 5.1b (bottom panel) and will be discussed in section 5.3). Based on the insights obtained from this modeling, I nanofabricated devices that incorporated all the features described above. A scanning electron microscope image of one such device is shown in Figure 5.1c.

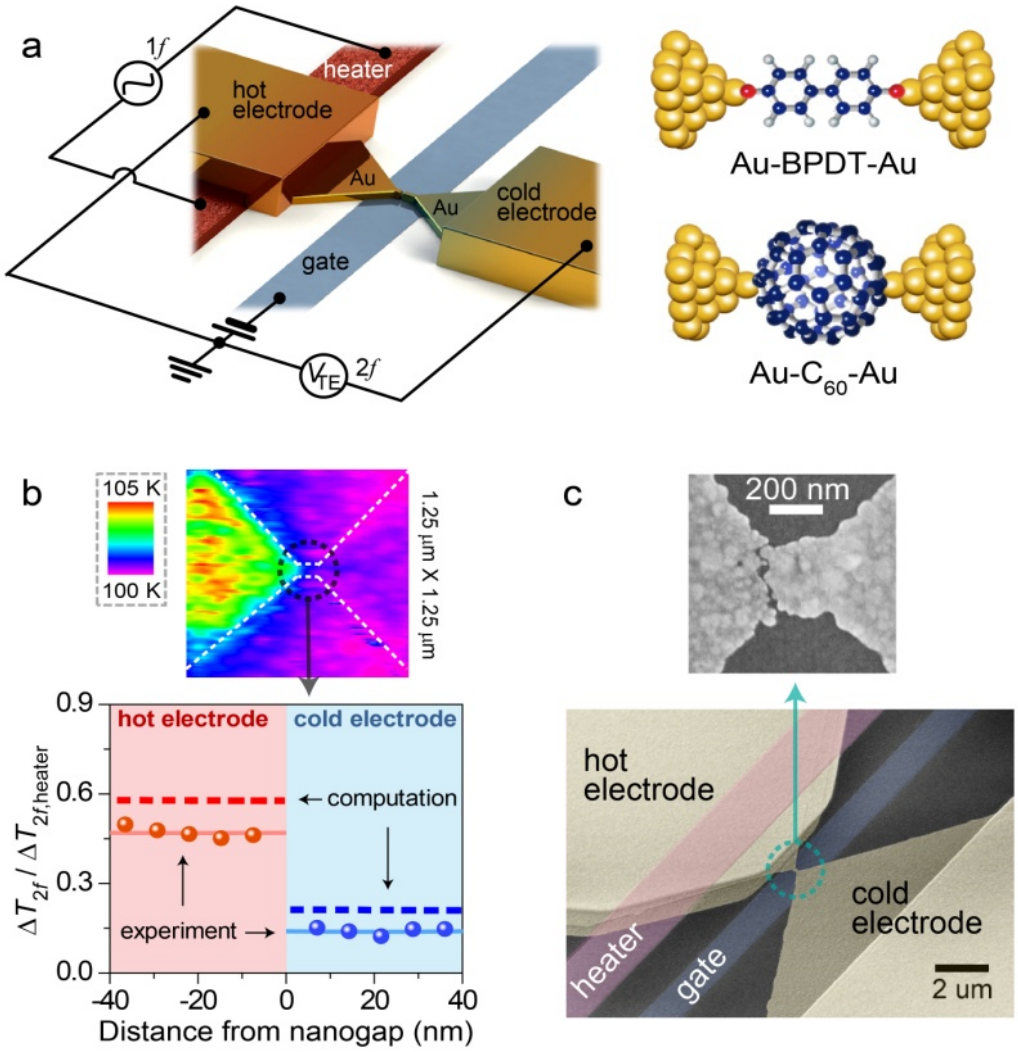

Figure 5.1: (a) Schematic of EBJIHs (left) and the molecular junctions studied in this work (right). Although the schematic shows a single molecule junction, the number of molecules in the junction is not necessarily one. The temperature differentials across MJs were established using the integrated heater. The electronic structure of MJs was tuned electrostatically via the gate electrode. Thermoelectric voltages were measured by monitoring voltage differentials between the hot and the cold electrodes. (b) (Top) Thermal map of a nanogap junction obtained using UHV-SThM at the ambient temperature of 100 K. Dashed line indicates the outline of the sample. (Bottom) Normalized temperature profile in the vicinity of the nanogap junction measured using UHV-SThM (circles) and calculated by the thermal modeling (dotted lines). (c) (Bottom) False-colored SEM image of an as-fabricated device. (Top) Magnified SEM image of a nanogap junction formed after electromigration. (Panels reproduced from the author's work of Ref. 52.)

Upon nanofabrication of the device, an electromigration approach is employed to create a nanometer-sized gap in Au nanowires (Figure 5.1c and will be discussed in section 5.2). Subsequently, a sinusoidally modulated electric current was supplied at a frequency f (5 Hz) into the integrated heater. This resulted in temperature amplitude oscillations at a frequency $2f$ due to Joule heating. In order to experimentally confirm the presence of temperature differentials across the nanometer-sized gaps, temperature fields were characterized using ultra-high vacuum scanning thermal microscopy (UHV-SThM) [14]. The measured amplitude of temperature oscillations in the vicinity of a nanoscale gap at the ambient temperature of 100 K is shown in the inset of Figure 5.1b (top panel) and features a rapid drop in the amplitude across the nanometer-sized gap. In order to further characterize the temperature profile, high spatial resolution (~8 nm) UHV-SThM imaging was performed in the immediate vicinity of the nanoscale gap. The measured temperature profile normalized to the heater temperature (ΔT_{2f} / $\Delta T_{2f,\,\mathrm{heater}}$) is shown in Figure 5.1b (bottom panel). It can be clearly seen that there is indeed an abrupt drop in the amplitude of temperature oscillations across the nanoscale gap. Specifically, the detailed experimental characterization (will be discussed in section 5.3) confirms that if the amplitude of temperature oscillations of the heater is $\Delta T_{2f,\,\mathrm{heater}}$, then the drop in the amplitude across the nanoscale gap ($\Delta T_{2f,\,\mathrm{Junc}}$) is $(0.34 \pm 0.03) \times \Delta T_{2f,\,\mathrm{heater}}$ and is in good agreement with the thermal modeling.

Upon successful characterization of temperature differentials, devices identical to those shown in Figure 5.1 (EBJIHs) were employed to study the thermoelectric properties in MJs. To accomplish this goal, EBJIHs were exposed to a solution containing prototypical molecules of biphenyl-4,4'-dithiol (BPDT) or fullerene (C_{60}) (see Figure 5.1a). This choice was governed by the expectation, from past studies by others [121-123], that molecular junctions created from BPDT and C_{60} feature off-resonant and resonant charge transport characteristics, respectively. Subsequently, the devices were

placed in a cryostat at the ambient temperature of 100 K (in a vacuum) and the electromigration process was initiated. This enables stochastical trapping of, in a subset of the devices, one or a few molecules between the source and drain electrodes [1, 50, 51]. The presence of the molecules was inferred from the gate voltage dependence of both the low-bias conductance and the Seebeck coefficient. Upon trapping the molecules, gate voltage (V_G) dependent low-bias conductance (G), V_G dependent thermoelectric voltages (ΔV_{2f}) and inelastic electron tunneling spectroscopy (IETS) were measured on the same junction.

The measured low-bias conductance of a Au-BPDT-Au junction ($G_{\text{Au-BPDT-Au}}$), as a function of gate voltage (V_G), is shown in Figure 5.2a. When V_G was varied from –8 V to +8 V, it was found that $G_{\text{Au-BPDT-Au}}$ decreased systematically. To characterize the thermoelectric properties of the Au-BPDT-Au junctions, temperature modulations ($\Delta T_{2f,\text{Junc}}$) of 1 K, 2 K, 3 K and 4 K were applied across the junctions and measured the resulting thermoelectric voltages (ΔV_{2f}) as a function of V_G as shown in Figure 5.2b. The error bars in Figure 5.2a and b correspond to the standard deviation of the data obtained from ten independent measurements on the same device. The magnitude of the measured thermoelectric voltages is seen to decrease systematically upon increasing V_G. In Figure 5.2c the obtained Seebeck coefficient of the junction ($S_{\text{Au-BPDT-Au}}$) is shown as a function of V_G (will be discussed in Appendix D for details of the estimation of the Seebeck coefficient). It can be seen that the Seebeck coefficient of the junction decreases systematically as V_G is increased—demonstrating that the thermoelectric properties of the junction can indeed be actively tuned significantly (~35%). Further, $S_{\text{Au-BPDT-Au}}$ is found to be positive for all values of V_G showing that charge transport is HOMO dominated [8, 13]. It should be noted that in control experiments performed on the pristine electromigrated devices (not exposed to molecules) there was no observable variation in both the low-bias conductance and the Seebeck coefficient of vacuum tunneling gaps

when V_G was varied from –8 V to +8 V (will be discussed in section 5.9). This is consistent with previous studies by others [124] of the electrical conductance of vacuum gaps in three-terminal configurations. Further, this is in contrast to what is observed in Figure 5.2 strongly suggesting that the observed data correspond to that of the molecular junction. In order to further confirm the presence of molecules in the junctions, IETS measurements [51, 107, 108] were performed and the vibrational features corresponding to Au-BPDT-Au junctions were observed (will be discussed in section 5.10). Finally, the data shown in Figure 5.2 correspond to one of seven Au-BPDT-Au junctions studied (will be discussed in section 5.5 for details on the variability between measurements of different devices).

In order to obtain a microscopic understanding of the observed dependence of $S_{\text{Au-BPDT-Au}}$ on V_G, a one-level transport model [8, 107, 111] is adopted. Within this model, it is assumed that energy (E) and gate voltage (V_G) dependent transmission ($T(E,V_G)$) of a MJ is well approximated by a Lorentzian function:

$$T(E,V_G) = \frac{4\Gamma^2}{\left[E-(E_0-\alpha V_G)\right]^2 + 4\Gamma^2} \tag{5.1}$$

Here, E_0 is the energetic separation of the dominant transport orbital with respect to the chemical potential E_F, Γ represents the coupling of the molecular orbital to the left and right electrodes (assuming symmetric coupling), and α is the effectiveness of gate coupling. From Equation 5.1 it can be shown that gate voltage dependent Seebeck coefficient ($S_{\text{Junc}}(V_G)$) of the junction is given by [8, 111, 113, 115, 119]:

$$S_{\text{Junc}}(V_G) = -\frac{\pi^2 k_B^2 T_{\text{amb}}}{3|e|}\left.\frac{\partial \ln\left[T(E,V_G)\right]}{\partial E}\right|_{E=E_F} = \frac{\pi^2 k_B^2 T_{\text{amb}}}{3|e|}\frac{2\left[E_F-(E_0-\alpha V_G)\right]}{\left[E_F-(E_0-\alpha V_G)\right]^2+4\Gamma^2} \tag{5.2}$$

where k_B is the Boltzmann's constant, e is the charge of an electron, and T_{amb} is the ambient temperature (100 K in this work).

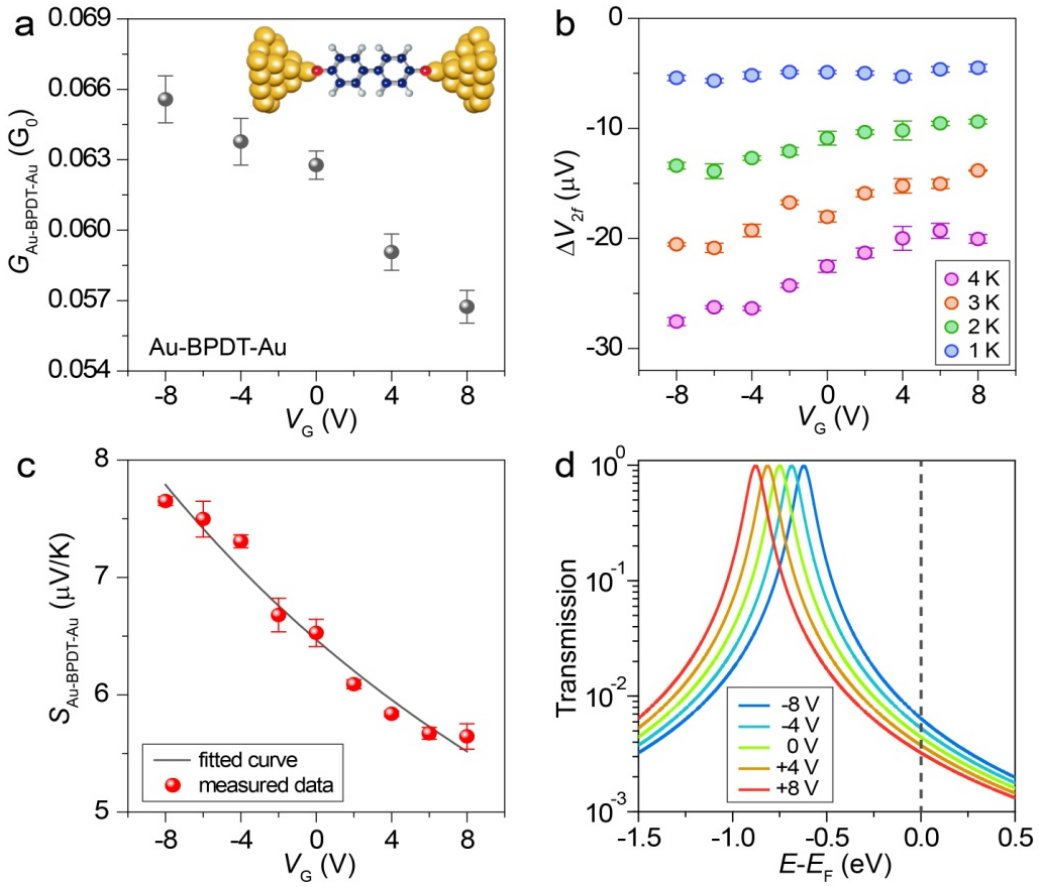

Figure 5.2: (a) Electrical conductance as a function of V_G for a BPDT junction (shown in the inset). Although the schematic shows a single molecule junction, the number of molecules in the junction is not necessarily one. G_0 equals $2e^2/h$, the quantum of the electrical conductance. (b) Measured thermoelectric voltages as a function of V_G for various temperature differentials across the junction. (c) Seebeck coefficient of the molecular junction as a function of V_G. The solid line indicates a least squares fit to the experimental data using Equation 5.2. (d) Transmission curves as a function of energy for five different values of V_G obtained using Equation 5.1 and the parameters obtained from the least squares fit. The vertical dotted line indicates the position of the chemical potential E_F. (Panels reproduced from the author's work of Ref. 52.)

It is clear from Equation 5.2 that a positive Seebeck coefficient implies that $[\partial \ln T(E, V_G)/\partial E]|_{E=E_F}$ is negative and that charge transport is HOMO dominated [8, 13, 113, 115, 119]. To gain more insights, the data in Figure 5.2c were fitted using Equation 5.2 and a least squares method to estimate the values of Γ, E_0 and α, which were found to be 0.025 eV, –0.75 eV and 0.016 eV/V respectively. Using these values the transmission curves were calculated for various values of V_G from Equation 5.1, which are shown in

Figure 5.2d. It can be seen that the resonant peak in the transmission shifts by ~0.26 eV when V_G is swept from –8 V to +8 V illustrating that gate voltage is effectively tuning the electronic structure of MJs. It is also clear from Figure 5.2d that the resonant peak of the transmission is far from E_F (the dotted line) for all values of V_G showing that charge transport in the Au-BPDT-Au junction occurs far-from resonance. Specifically, the resonant peak of the transmission at V_G = 0 V is ~0.75 eV from E_F and is in good agreement with what was found by others in previous studies [125]. The transmission curves in Figure 5.2d can be used to estimate the low-bias conductance of the Au-BPDT-Au junction ($G = G_0 \times T(E = E_F, V_G)$) and is found to decrease monotonically from ~0.006 G_0 to ~0.003 G_0 at E_F when V_G is varied from –8 V to +8 V: These values are smaller than those of the experimental results shown in Figure 5.2a suggesting that there are probably multiple molecules in the junction.

In addition to these measurements, corresponding measurements were also performed on Au-C_{60}-Au junctions. The measured V_G dependent low-bias conductance, thermoelectric voltages and Seebeck coefficient ($S_{Au\text{-}C60\text{-}Au}$) are shown in Figure 5.3a – c, respectively (the data correspond to one of seven fullerene junctions studied) and the corresponding IETS is presented in section 5.10. It is noticeable that in Au-C_{60}-Au junctions both the low-bias conductance and the Seebeck coefficient are ~10 times larger than those of Au-BPDT-Au junctions. Further, the Seebeck coefficient could be tuned by a large amount (~300%) via electrostatic gating. As shown later, this is primarily due to the resonant charge transport characteristics of C_{60} junctions. It is clear from both the observed increase in the low-bias conductance [8] upon increasing V_G and the negative sign of $S_{Au\text{-}C60\text{-}Au}$ [8, 113, 114, 117] that charge transport is dominated by the lowest unoccupied molecular orbital (LUMO). Surprisingly, in contrast to Au-BPDT-Au junctions, the measured $S_{Au\text{-}C60\text{-}Au}$ shown in Figure 5.3c neither monotonically increases

nor decreases as V_G is increased from –8 V to +8 V—instead, it exhibits a pronounced minimum and is concaved upwards ("U" shaped).

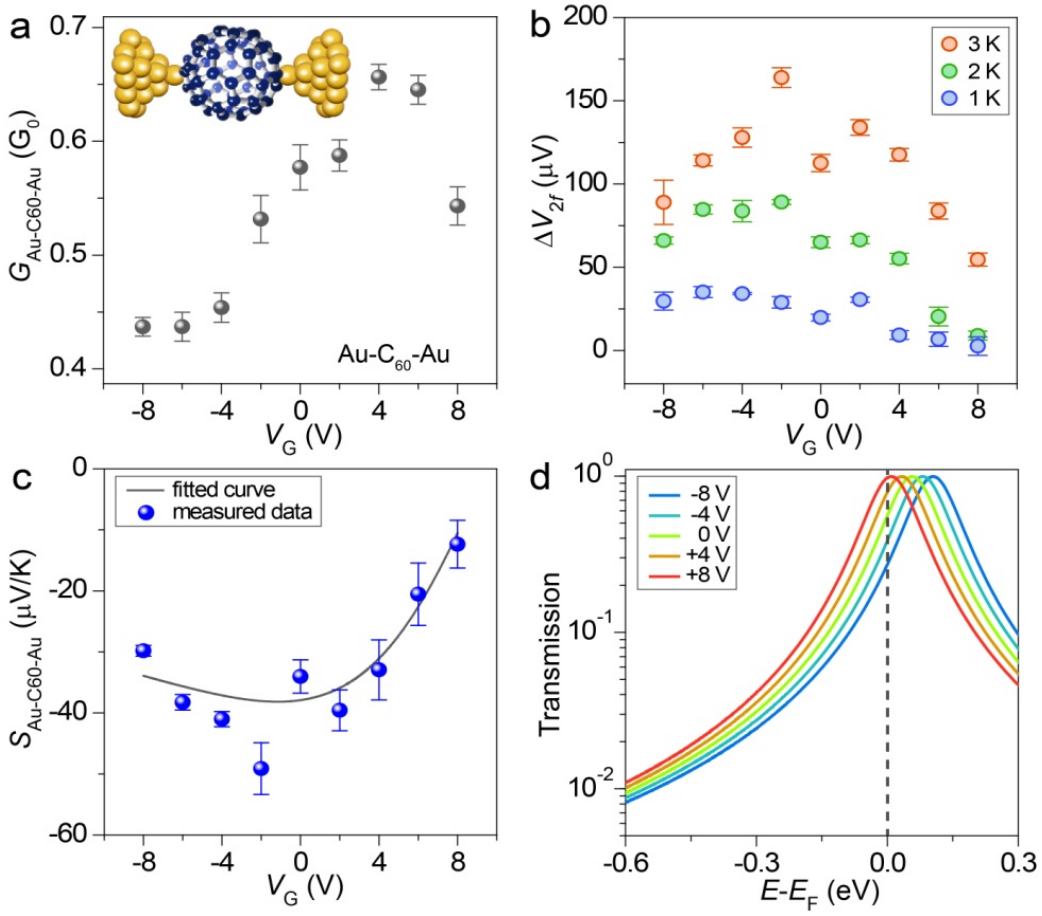

Figure 5.3: (a – d) Same as Figure 5.2 but for a Au–C_{60}–Au junction. In contrast to Au–BPDT–Au junctions, charge transport is dominated by the LUMO level, which is indicated by a negative Seebeck coefficient in Figure 5.3c. (Panels reproduced from the author's work of Ref. 52.)

In order to better understand this behavior, a least squares fit of the Seebeck coefficient data were again performed using Equation 5.2 and estimated Γ, E_0 and α to be 0.032 eV, 0.057 eV and 0.006 eV/V respectively. The estimated transmission curves for various values of V_G are shown in Figure 5.3d and reveal that charge transport in C_{60} junctions is close to resonance (i.e. the dominant transport orbital is very close to E_F): A

result that confirms previous theoretical predictions [122, 123]. The concave up V_G dependence of the Seebeck coefficient is intimately related to the resonant charge transport properties. Specifically, this dependence arises from a change in the sign of the curvature ($\kappa \propto \partial^2 T / \partial E^2$) of the transmission at an energy close to the resonant peak or in other words due to the presence of an inflection point in $T(E,V_G)$. Thus, when V_G is chosen such that the inflection point and E_F overlap with each other, the magnitude of the Seebeck coefficient is maximized. Whereas, further changes in V_G move the inflection point away from E_F and result in a decrease in the magnitude of S_{Junc} (will be discussed in section 5.8). The predicted magnitude of the transmission at E_F (Figure 5.3d) is consistent with the measured low-bias conductance (Figure 5.3a) of the C_{60} junction suggesting that there is probably only one or a few C_{60} molecules in the junction. Since charge transport is close to resonance in C_{60} junctions, it is expected that small perturbations in E_0 and/or Γ, which may arise from minor variations in contact geometry [122, 123], could result in a different dependence of $S_{Au\text{-}C60\text{-}Au}$ on V_G and is indeed experimentally confirmed (will be discussed in section 5.6 for additional datasets). Further, the non-monotonic behavior observed in Figure 5.3a, at high values of V_G, is also possibly due to small variations in junction geometry introduced by electrostatic perturbations.

Finally, I note that the gate coupling (α) estimated in this work, from a one-level transport model, was 0.016 eV/V for a BPDT junction and 0.006 eV/V for a C_{60} junction, respectively. These relatively low values of α are due to the additional dielectric layer (10 nm thick SiN_x) deposited on top of native Al_2O_3 layer during the nanofabrication process. In the current design, this dielectric layer is essential for electrically isolating the source and drain electrodes from the gate electrode. The gate coupling can be potentially improved by employing the principles developed in this work in conjunction with a side-gate scheme [124] that has been recently demonstrated. In such a side-gate scheme the gate electrode can be placed in the immediate vicinity (<10 nm) of the source and drain

electrodes. Further, a higher gate voltage can be applied due to higher breakdown voltage limit of vacuum. I hypothesize, based on some preliminary calculations, that gate couplings four times larger than those accomplished in this work can be potentially obtained using such a side-gate scheme.

5.2 Preparation of samples and electromigration for creating MJs

In order to create MJs, electromigration (EM) was performed by the following procedures described elsewhere [1, 50, 51, 110]. Briefly, EBJIHs were mounted in a cryostat after they were exposed to a solution of the desired molecules of BPDT [51, 107] or C_{60} [50] to assemble the molecules on the samples pre-cleaned by O_2 plasma (10 minutes at 250 mW). The samples were immersed in a dilute solution of BPDT molecules (~0.1 mM) in 2 ml ethanol for >5 hours or C_{60} molecules (~0.1 mM) in 2 ml toluene for 2 minutes. Subsequently, the samples exposed to BPDT molecules were rinsed with ethanol and blown dry, whereas the samples covered by C_{60} molecules were ambient dried without rinsing [3, 47, 50, 107, 126]. Subsequently, EM was initiated in a vacuum at 100 K by applying a cyclic voltage bias across the Au nanowires of EBJIHs, while the resistance of the nanowires was continuously monitored. The applied voltage was linearly ramped up in steps of 1 mV every 50 ms until the resistance increased by a value that was heuristically chosen to be 1 – 10% of the increase in the nanowire resistance before the initiation of the voltage ramp. Upon detection of the predetermined increase in the resistance, the voltage was rapidly ramped down (~1 ms) to a low voltage (~0.1 V). This process was repeated multiple times until the nanowires break forming nanogaps. It should be noted that the molecular trapping event during EM occurs stochastically. In the EM process of this work, the yield of forming MJs that show non-

trivial dependence of both the low-bias conductance and the Seebeck coefficient on V_G is ~3% (14/464).

5.3 Characterization of temperature differentials across nanometer-sized gaps

In order to characterize temperature differentials across nanogaps in EBJIHs, I first performed finite element modeling using COMSOL (Joule heating module). An electric current was simulated through the integrated heater, while all other surfaces were considered to be electrically insulated. In addition, the temperature of the bottom surface (Si substrate), which is in contact with the cold finger of a cryostat in the experiments, was modeled to be at 100 K, while all other surfaces were assigned to be thermally insulated. Further, the triangular shaped feature located on the electrode I (Figure 5.4a) was introduced to mimic the effects of the shield layer, which enhances heat transfer from the integrated heater to the nanogap (through electrode I).

The thermal conductivity and the electrical resistivity of materials were chosen to be 320 W/m·K [69] for Au electrodes, 160 W/m·K and 4.4×10^{-8} Ω·m respectively for thin-film Au layers [105] (heater, shield and nanowires) and 11.75 W/m·K for thin Al gate [77, 78]. Further, the thermal conductivity of Si, SiO_2, SiN_x and Al_2O_3 were assigned to be 150 W/m·K [69], 0.7 W/m·K [127], 0.2 W/m·K [127] and 1 W/m·K [74] respectively. As can be seen in Figure 5.4c, the computed temperature profile shows a clear discontinuity at the nanogap. It is noticeable that in this modeling all thermal boundary resistances were ignored for computational simplicity. However, such thermal boundary resistances only serve to further increase the thermal resistance and to enhance the temperature drop across nanogaps. The mesh employed in the calculations is shown in Figure 5.4d. It can be seen that the adaptive meshing scheme employed by me results in a relatively fine

mesh (~10 nm) in the vicinity of the nanogap. The mesh size is in fact smaller than both the inelastic mean free path of electrons in Au electrodes and the width of the nanowire in the device. Thus the finite element model provides an excellent continuum level description of the temperature field.

The calculation results showing the temperature discontinuity at the nanogap can be qualitatively understood as follows. From Fourier's law for heat conduction in isotropic materials it is clear that the gradient of the temperature field ($\vec{\nabla}T$) is related to the local heat flux ($\vec{q}$) and the thermal conductivity (k) via the following relationship: $\vec{\nabla}T = -\vec{q}/k$. This implies that the temperature gradients are large in the presence of large heat fluxes and/or low thermal conductivity. The finite element simulations indeed reflect this fact and show that the temperature gradients within the two electrodes that surround the nanogap (Figure 5.1b) are small. This is because the heat currents in this region are relatively small and the thermal conductivity of Au is relatively large. Further, the simulations suggest that there is a significant temperature drop across the nanogap. In order to experimentally demonstrate the presence of a temperature drop across the nanogap, it is necessary to prove the following facts: 1) the temperature gradients in the electrodes surrounding the nanogap are small/negligible, 2) the temperature of the electrodes on the two sides of the nanogap is different (this would show that there is a temperature differential across the nanogap and since there is a negligible temperature drop within the electrodes the temperature drop has to be in the nanogap).

In order to experimentally confirm the existence of temperature differentials across nanogaps and also to estimate the actual temperature drop, temperature fields in the vicinity of nanoscale gaps were measured (as shown in Figure 5.1b) using UHV-SThM [14]. The amplitude of temperature oscillations of the heater and the amplitude of temperature differentials across nanogaps were measured while applying AC current to

the heater (Figure 5.5a). As expected, the amplitude of temperature oscillations of the heater and the nanogap show a linear dependence on the power input to the heater. In order to obtain the information of temperature amplitude systematically with high spatial resolution, the following strategy was adopted: The temperature amplitude along nanowires was measured at points separating by ~8 nm from each other. The data from one such measurement are shown in Figure 5.5b and clearly show an abrupt temperature drop across the nanogap. The result also shows that the temperature gradients within the electrodes are very small. Hence, it is expected that the temperature at the edge of the electrodes is the same as the temperature of a point that is within each electrode and ~10 nm away from it. Thus the experimental results unambiguously confirm that there is a temperature differential across the nanogap. Further, similar measurements were performed on six different devices (three line-scans like the one shown in Figure 5.5b on each device), and based on these measurements the average temperature amplitude of the hot and the cold electrodes was estimated. From these data the temperature drop across the nanogaps (more precisely the difference in the amplitude of temperature oscillations) was estimated to be ~34 ± 3% of the amplitude of temperature oscillations of the heater ($\Delta T_{2f,\,\mathrm{heater}}$) as summarized in Table 5.1.

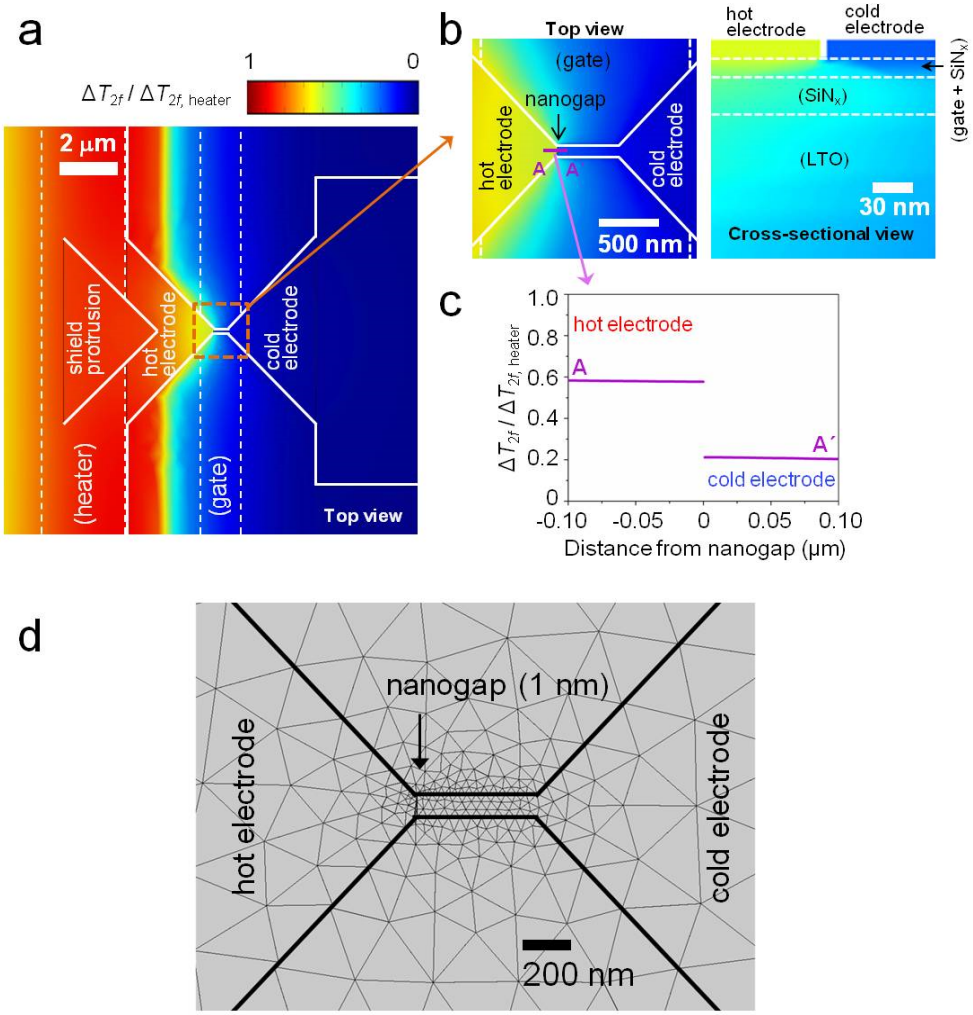

Figure 5.4: (a) Calculated temperature field of an EBJIH. The device including the nanowire is highlighted by solid lines for visual clarity. The embedded layers (gate and heater) are represented by dotted lines. (b) Magnified image of the region surrounding the nanogap indicated by the dotted square in (a). (c) Temperature profile along the line A–A' depicted in (b). The discontinuity of temperature amplitude oscillations at the nanogap is clearly seen. (d) Depiction of the mesh employed in the finite element modeling. There are no points within the nanogap as the surfaces surrounding the nanogap are assumed to be thermally insulating. (Panels reproduced from the author's work of Ref. 52.)

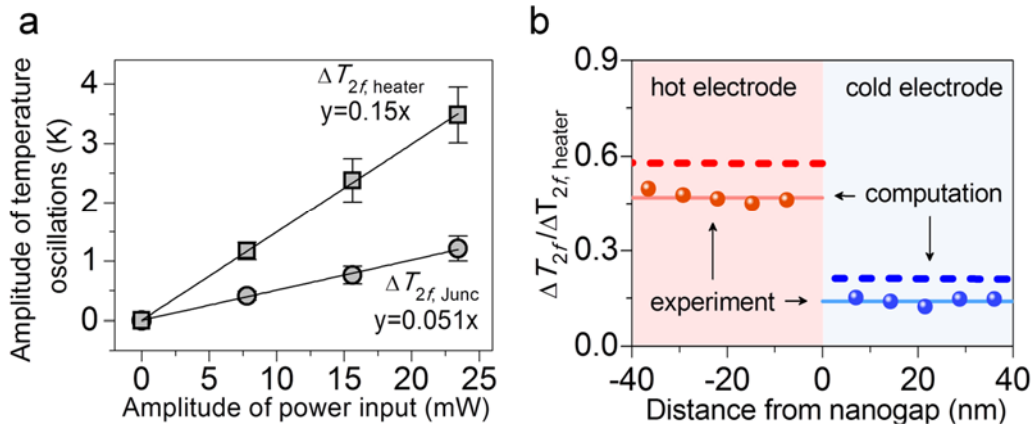

Figure 5.5: (a) Measured amplitude of temperature oscillations of the heater (square symbols) and the measured amplitude of temperature differentials across the nanogap (circles) are shown as a function of the amplitude of power input to the integrated heater. The obtained linear relationship is used to estimate the appropriate power input required to establish 1 K, 2 K, 3 K and 4 K temperature differentials across nanogaps during the thermoelectric voltage measurements. (b) Presence of temperature differentials across a nanogap was confirmed by UHV-SThM, which shows that the drop in the amplitude of temperature oscillations across the nanogap is ~34% of the amplitude of temperature oscillations of the heater. Circles: measured temperature amplitude along nanowires, Solid lines: linear fits of the experimental data in each electrode, and Dotted lines: calculated temperature profile depicted in Figure 5.4c magnified in the immediate vicinity of the nanogap. (Panels reproduced from the author's work of Ref. 52.)

Table 5.1: Summary of the measured temperature differentials across nanogaps. The amplitude of temperature oscillations of the heater ($\Delta T_{2f,\,\text{heater}}$) was assigned to be 1, and all other temperature amplitude oscillations were normalized accordingly. (Table reproduced from the author's work of Ref. 52.)

	Devices					
	#1	#2	#3	#4	#5	#6
Hot electrode	0.64	0.59	0.64	0.67	0.55	0.62
Cold electrode	0.25	0.27	0.29	0.32	0.24	0.28
$\Delta T_{2f,\,\text{Junc}}$ (% of $\Delta T_{2f,\,\text{heater}}$)	39	32	35	35	31	34

5.4 Thermoelectric voltage measurements

In order to establish temperature differentials across the nanogaps, a sinusoidal electric current is applied to the integrated heater at a frequency f (5 Hz) using a function generator (Agilent 33210A), and this results in temperature differentials that oscillate at

2*f* (Figure 5.6). This in turn results in thermoelectric voltage differentials across the junctions. The thermoelectric voltage differentials are measured by first buffering using a high input impedance (100 MΩ) voltage amplifier (SIM 910) and subsequently measuring using a SR 830 lock-in amplifier (LIA) in a bandwidth of 0.078 Hz. While measuring thermoelectric voltages of MJs, a gate voltage was incremented in steps of 2 V with a 10-second delay between the steps to minimize the effects of the capacitive coupling between the gate electrode and other electrodes of MJs. At each gate voltage step, the output of LIA was recorded for 1 second and averaged to obtain one data point. This procedure was repeated ten times to get ten data points at each step. The data shown in Figure 5.2 and 5.3 are the average of ten data points, whereas the error bars represent the standard deviation of these data points. For the gate voltage dependent low-bias conductance measurements, the same measurement scheme was used to estimate the average and the standard deviation. In addition, the applied gate voltage was restricted to be in the range of ±8 V as the ~12 nm thick dielectric layer (native Al_2O_3 and SiN_x) between the gate electrode and other electrodes of MJs was found to break down at gate voltages of ~±10 V.

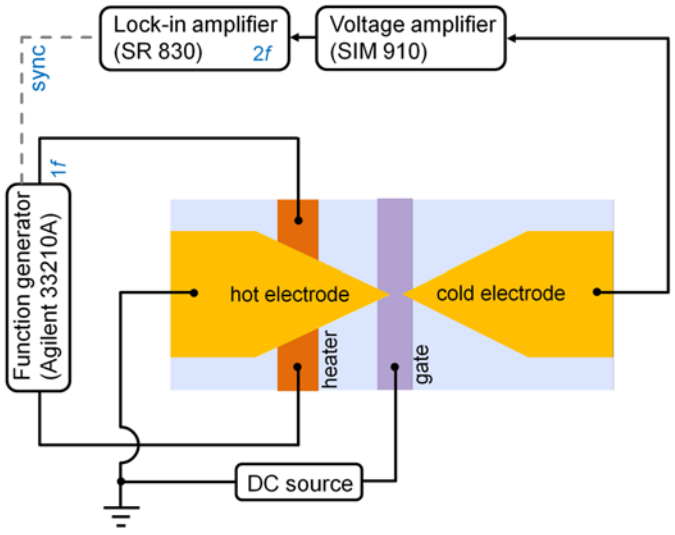

Figure 5.6: Schematic of the thermoelectric voltage measurements setup. (Figure reproduced from the author's work of Ref. 52.)

5.5 Variability in the measured low-bias conductance and the Seebeck coefficient of MJs

Creation of molecular junctions in EBJIHs is a stochastic process, therefore not all electromigrated junctions have molecules bridging the source and drain electrodes. In this work, a total of 1152 devices were nanofabricated, of which 464 devices (~40%) were appropriate to perform the experiments. The remaining had defects such as a leakage of gate dielectrics and the failure of nanowires by electrostatic discharge. Among these, after electromigration at 100 K, ~35% (162/464) displayed non-trivial *I-V* characteristics. However, only a much smaller subset (~3% (14/464), seven for BPDT junctions and seven for C_{60} junctions) had repeatable gate voltage dependent characteristics and was able to be reliably operated to obtain the full-set of data from diverse measurements for a couple of hours. All these junctions displayed a non-trivial dependence of the low-bias conductance and the Seebeck coefficient on gate voltage. This low-yield is indeed consistent with what observed by others in previous studies [51, 128, 129]. It is also noticeable that in this work junctions showing the Coulomb blockade effects [3, 129] were not considered. Further, since the microscopic details of the molecular junctions created by electromigration are not controllable, the low-bias conductance and the Seebeck coefficient measured in the experiments show a broad distribution. In Figure 5.7, the variability in the measured low-bias conductance and the Seebeck coefficient is shown when no gate voltage is applied (V_G = 0 V). The average of the measured low-bias conductance of Au-BPDT-Au junctions is ~10 times larger than that of a single molecular junction (~0.001 G_0) [115, 126, 130, 131], which may attributed to the presence of multiple molecules in the junctions. In contrast, the measured Seebeck coefficient of the BPDT junctions is comparable to what is expected from previous measurements by others at ~300 K [13, 132]. This is due to the relative insensitivity of

the Seebeck coefficient [13, 111] to the number of molecules in the junctions. The measured low-bias conductance of C_{60} junctions are comparable to that of a C_{60} single molecular junction (~0.1 G_0) [114, 133] suggesting that only one or a few molecules are present in the junctions. Further, the measured Seebeck coefficient of C_{60} junctions also falls into the range observed from the previous measurements by others at ~300 K [114].

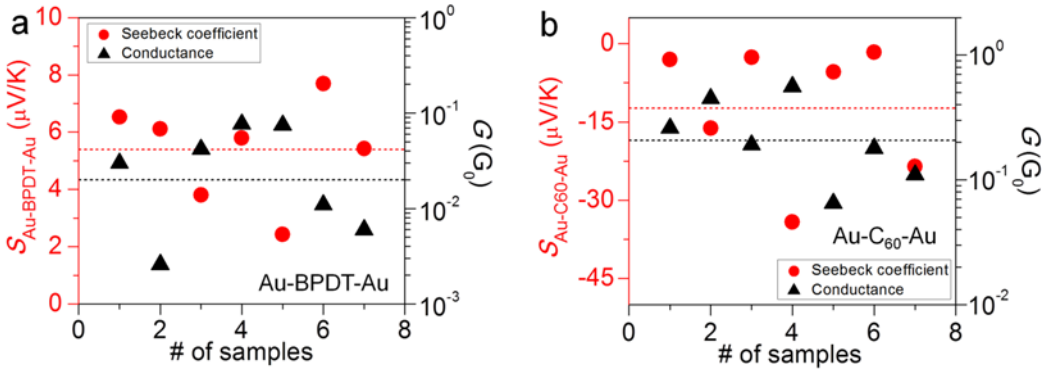

Figure 5.7: Variability of the low-bias conductance (G) and the Seebeck coefficient (S) of BPDT (a) and C_{60} (b) junctions when V_G = 0 V. The average values of S and G are ~+5.4 μV/K and ~0.02 G_0 for BPDT junctions and ~–12.4 μV/K and ~0.2 G_0 for C_{60} junctions, respectively. (Panels reproduced from the author's work of Ref. 52.)

5.6 Additional datasets of gated Seebeck coefficient

In Figure 5.8, two additional datasets of the gated Seebeck coefficient are shown for BPDT and C_{60} junctions (measured at 100 K). The Seebeck coefficient of BPDT junctions (Figure 5.8a and b) is found to systematically decrease when a gate voltage is varied from –8 V to +8 V as the dominant HOMO level shifts away from E_F. Further, the Seebeck coefficient of these junctions were found to be ~+6 μV/K when no gate voltage was applied (V_G = 0 V). These values are very similar to that reported in Figure 5.2 and reflect the relative insensitivity of the Seebeck coefficient of Au-BPDT-Au junctions to variations in junction geometry. The measured Seebeck coefficient of two additional C_{60} junctions is shown in Figure 5.8c and d, which feature a negative Seebeck coefficient

(consistent with the data shown in Figure 5.3) that indicates charge transport is LUMO dominanted [114, 122, 123] in Au-C_{60}-Au junctions. However, gate voltage dependence of the Seebeck coefficient of these junctions is different from each other and also different from what was shown in Figure 5.3. This is primarily due to the fact that in C_{60} junctions charge transport is very close to resonance, thus gate voltage dependence of the Seebeck coefficient is very sensitive to small perturbations in junction geometry (will be discussed in section 5.8).

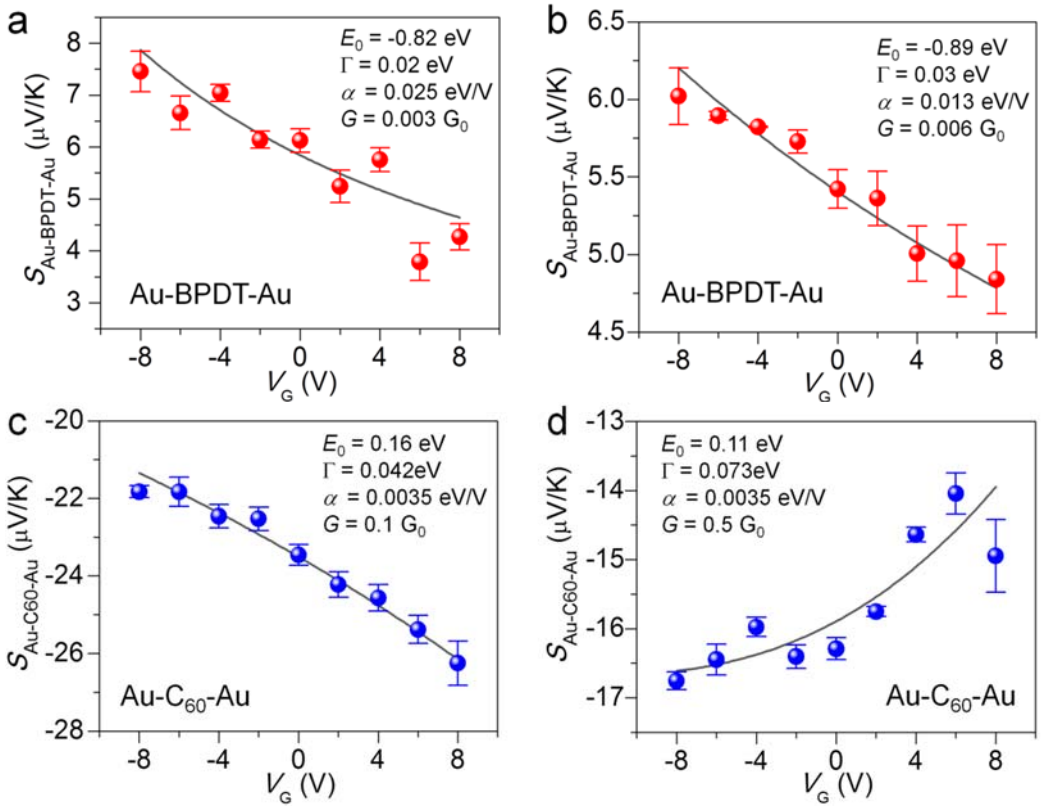

Figure 5.8: More datasets of the gated Seebeck coefficient along with fitting curves obtained using Equation 5.4 for BPDT (a, b) and C_{60} (c, d) junctions. The values of fitting parameters corresponding to a one-level transport model are listed in the insets. (Panels reproduced from the author's work of Ref. 52.)

5.7 One-level transport model to quantify gate voltage dependence

A one-level model of charge transport has been extensively used to obtain additional insights into charge transport in MJs [111]. In this work, this model was employed to obtain the information about the electrode-molecule coupling and the energy level alignment relative to the chemical potential E_F. In the one-level transport model, the transmission is given by the formula as shown in Equation 5.3. The transmission (T) depends on the energetic location of the dominant molecular level (E_0), the coupling constant Γ (in the case of symmetric coupling) as well as the gate voltage V_G [111, 134] and is given by:

$$T(E,V_G)=\frac{4\Gamma^2}{\left[E-(E_0-\alpha V_G)\right]^2+4\Gamma^2} \text{ and } G=\frac{2e^2}{h}T(E=E_F,V_G) \tag{5.3}$$

This can be used to obtain the Seebeck coefficient of the junction using the following equation:

$$S_{Junc}(V_G)=-\frac{\pi^2 k_B^2 T_{amb}}{3|e|}\frac{\partial \ln\left[T\left(E,V_G\right)\right]}{\partial E}\bigg|_{E=E_F}=\frac{\pi^2 k_B^2 T_{amb}}{3|e|}\frac{2\left[E_F-(E_0-\alpha V_G)\right]}{\left[E_F-(E_0-\alpha V_G)\right]^2+4\Gamma^2} \tag{5.4}$$

where k_B is the Boltzmann's constant, e is the charge of an electron and T_{amb} is the ambient temperature, respectively.

The shift in the energetic separation between the resonant energy level and E_F was analyzed in section 5.1 when a gate voltage is applied. Specifically, these shifts were obtained by fitting the measured Seebeck coefficient to Equation 5.4. Here, the same data are presented in a slightly different form in Figure 5.9. In plotting these figures it is assumed that the position of the dominant transport orbital is fixed and the position of the chemical potential changes. This approach has been used by several researchers including in a recent work [135] and is presented here for the sake of completeness.

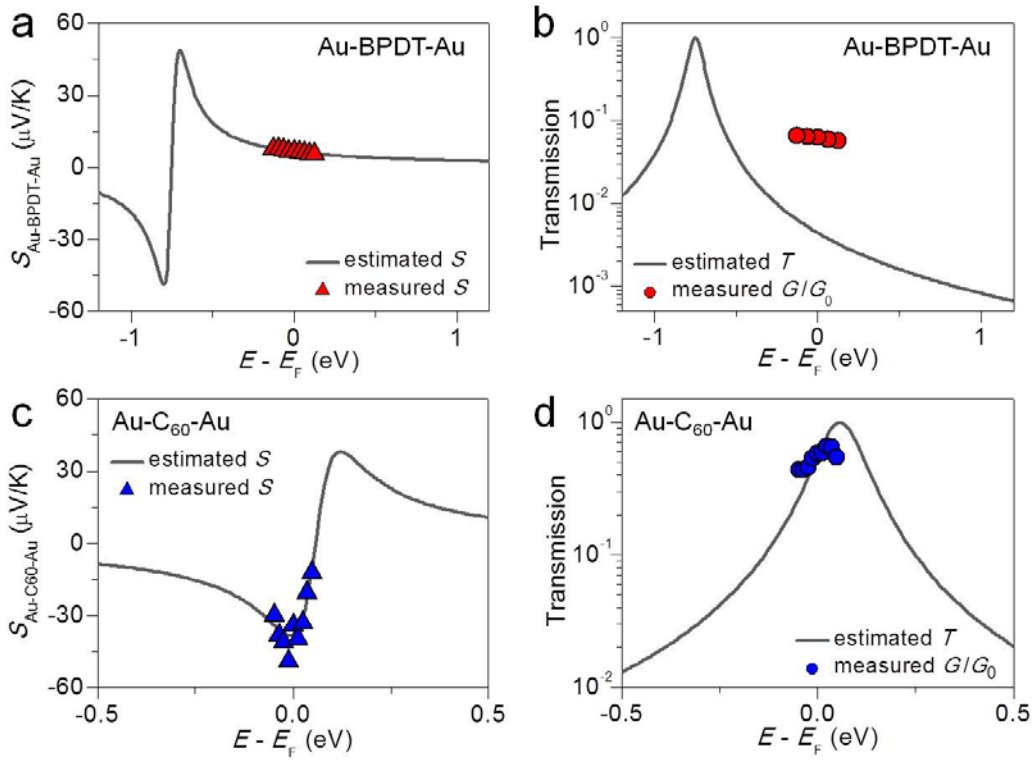

Figure 5.9: Seebeck coefficient and transmission corresponding to the parameters obtained by fitting a one-level transport model to the Seebeck coefficient data shown in Figure 5.2 and 5.3. Experimental data (symbols) for a BPDT junction are shown in (a, b) and data for a C_{60} junction are shown in (c, d). The parameters corresponding to these fittings are: $\Gamma = 0.025$ eV, $E_0 = -0.75$ eV, $\alpha = 0.016$ eV/V for the BPDT junction and $\Gamma = 0.032$ eV, $E_0 = +0.057$ eV, $\alpha = 0.006$ eV/V for the C_{60} junction respectively. (Panels reproduced from the author's work of Ref. 52.)

It can be seen from Figure 5.9a and c that the measured Seebeck coefficients fit the one-level transport model very well. Further, in correspondence to what has been discussed in section 5.1, it can be seen in Figure 5.9b that the measured low-bias conductance is larger than that predicted by the model. This can be directly attributed to the presence of multiple molecules in the junction. It should be noted that the measured Seebeck coefficient was used in the fitting to Equation 5.4 because the Seebeck coefficient is insensitive to the number of molecules in the junction.

5.8 Additional discussion of the gate voltage dependence of the Seebeck coefficient of Au-C_{60}-Au junctions

In order to understand gate voltage dependence of the Seebeck coefficient of C_{60} junctions, the computed transmission is shown in Figure 5.10a in a scenario where charge transport is close to resonance: i.e. the peak of the transmission is close to E_F. Specifically, the transmission is constructed using the same parameters that were extracted for the Au-C_{60}-Au junction in Figure 5.3: Γ = 0.032 eV, E_0 = 0.057 eV, α = 0.006 eV/V and V_G = 0. Further, in Figure 5.10b the computed Seebeck coefficient is shown (using Equation 5.4 and the transmission in Figure 5.10a) as the position of the resonant peak (E_0) is varied with respect to E_F. Here, it should be noted that Equation 5.4 was simplified by assuming the low temperature limit. However, it was found from another calculation [111], performed without the low temperature approximation, that the Seebeck coefficient does not differ significantly from that obtained using Equation 5.4. It can be seen that from Figure 5.10 that when $\Delta = E_F - E_0 = 0$, i.e. when the resonant peak is aligned with E_F, the Seebeck coefficient becomes zero. Further, it is clear that when Δ = –0.062 eV the magnitude of the Seebeck coefficient is the largest. This existence of the maxima at Δ = –0.062 eV is due to a sign change in the curvature ($\kappa \propto \partial^2 T / \partial E^2$) of the transmission at the point where the blue and the red regions meet in Figure 5.10a (the inflection point is marked by the arrow). Therefore, it is clear that if charge transport is close to resonance, a non-monotonic change in the magnitude of the Seebeck coefficient can be observed.

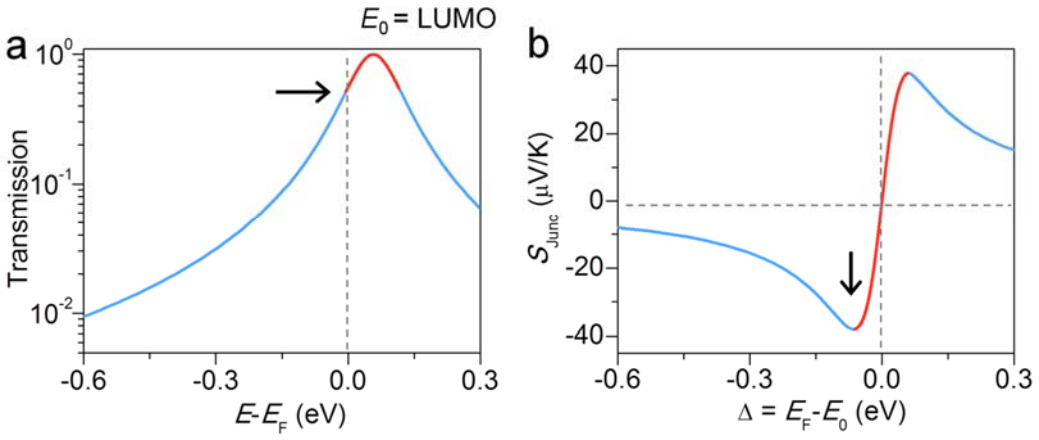

Figure 5.10: Computed transmission for a Au-C_{60}-Au junction (a) and the corresponding Seebeck coefficient computed using Equation 5.4 (b). The arrow in (a) indicates the position of an inflection point. The regions of the curve shown in different colors have different signs of the curvature. In (b), the Seebeck coefficient is plotted as a function of $\Delta = E_F - E_0$ (as E_0 is varied with respect to E_F) to visualize the sign change of the Seebeck coefficient and the "U" shaped feature reported in Figure 5.3. (Panels reproduced from the author's work of Ref. 52.)

5.9 Gate voltage independence of the low-bias conductance and the Seebeck coefficient in clean vacuum tunnel junctions

The control experiments were performed on pristine devices that were not exposed to molecules (i.e. clean vacuum tunnel junctions). Upon electromigration of the devices, gate voltage dependence of the low-bias conductance and the Seebeck coefficient of clean vacuum tunnel junctions were studied. The results obtained from these measurements on two representative devices, one with a large low-bias conductance (~0.46 G_0) and the other with a smaller low-bias conductance (~0.006 G_0) are shown in Figure 5.11. It can be seen that both the low-bias conductance and the Seebeck coefficient are independent of the applied gate voltage—in strong contrast to what is seen in Au-BPDT-Au and Au-C_{60}-Au junctions. In addition, the magnitude of the Seebeck coefficient of these vacuum tunnel junctions is seen to be significantly smaller than what was measured on molecular junctions. Finally, the sign of the Seebeck coefficient is found to be negative in both cases indicating LUMO-like tunneling.

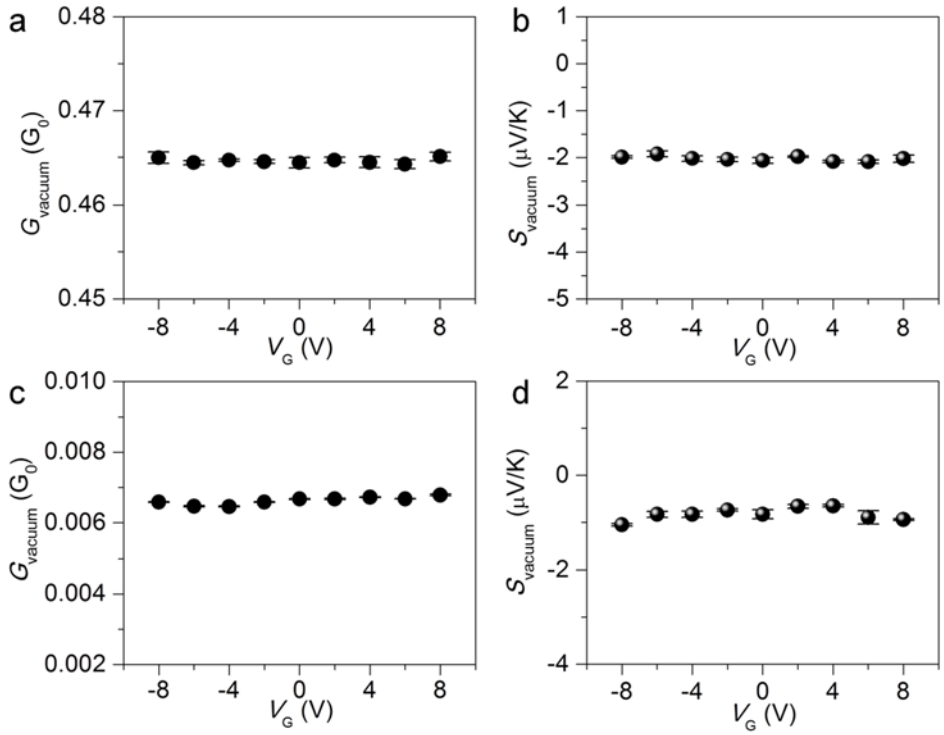

Figure 5.11: Low-bias conductance (a, c) and the Seebeck coefficient (b, d) as a function of V_G for electromigrated EBJIHs that were not exposed to molecules. The Seebeck coefficient shown in (b) and (d) were measured on the same junctions corresponding to the data shown in (a) and (c), respectively. (Panels reproduced from the author's work of Ref. 52.)

5.10 Inelastic electron tunneling spectroscopy (IETS)

IETS (d^2I/dV^2) was employed to identify the unique vibrational modes of Au-BPDT-Au and Au-C_{60}-Au junctions. These spectra provide additional evidence confirming the presence of appropriate molecules in the nanogaps of EBJIHs [51, 107, 108, 136, 137]. In Figure 5.12, IETS spectra obtained by numerical computation from *I-V* curves (measured at 100 K) [5, 136-138] are presented. The red curves in Figure 5.12 represent antisymmetrized spectra (*AS*), obtained by $AS = (f(V) - f(-V)) / 2$, where $f(V)$ represents the IETS data. The similarity between the IETS spectra and the *AS* confirms that molecules are almost symmetrically bonded to both source and drain electrodes. In addition, the fact that peaks appear at the same absolute voltages for both bias polarities provides strong evidence that they indeed originate from molecular vibrations [108, 133,

139]. Therefore, the vibrational modes are assigned, which appear in both bias polarities symmetrically.

Note that the IETS spectrum obtained at 100 K is significantly broadened and hence only a few peaks can be detected [140]. This is evident in the IETS data presented in Figure 5.12. Although the peaks are not sharp, they provide compelling evidence for the presence of appropriate molecules in the Au-BPDT-Au and Au-C_{60}-Au junctions. The molecular vibrational modes corresponding to the peaks are listed in Table 5.2 and 5.3.

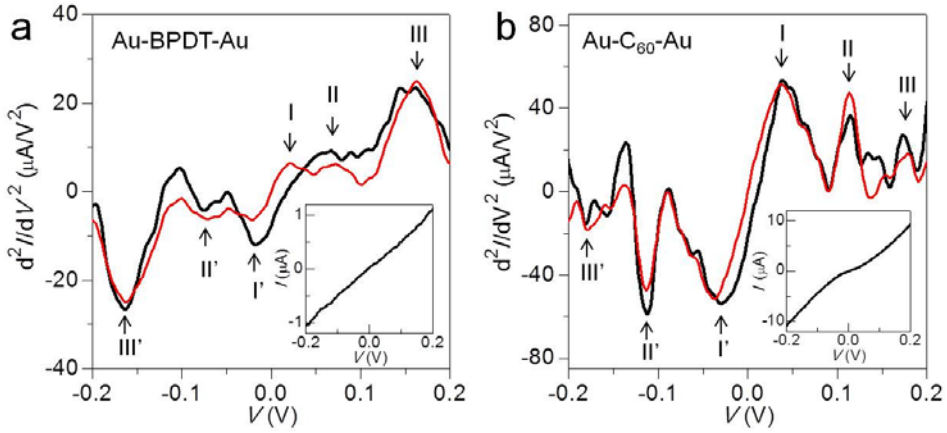

Figure 5.12: Representative IETS spectra and *I-V*s (inset) of (a) Au-BPDT-Au and (b) Au-C_{60}-Au junctions are presented. IETS spectra (black) for both bias polarities are shown together with a curve antisymmetrized (red) with respect to the bias polarity, obtained by a simple formula, $AS = (f(V) - f(-V)) / 2$. IETS spectra were obtained from numerical derivative of each *I-V* curve in the inset. Roman numerals in (a) and (b) indicate each vibrational mode as listed in Table 5.2 and 5.3 for BPDT and C_{60} junctions, respectively. (Panels reproduced from the author's work of Ref. 52.)

Table 5.2: Summary of the vibrational modes assignment in the IETS spectra for a BPDT junction. Each peak position in the IETS spectra is identified by previous theoretical calculations and experiments. (Table reproduced from the author's work of Ref. 52.)

Peak position (mV)		Mode	Description	References
I	20	ν(Au-S)	Au-S stretching	[51, 136]
II	70	ν(C-S)	C-S stretching	[107, 138, 140, 141]
III	160	γ(C-H)	C-H in-plain bending	[107, 138, 140, 141]

Table 5.3: Summary of the vibrational modes assignment in the IETS spectra for a C_{60} junction. Each peak position in the IETS spectra is identified by previous theoretical calculations and experiments. (Panels reproduced from the author's work of Ref. 52.)

Peak position (mV)		Modes	References
I	39	Gu(1) / H g(1/2)	[133, 142]
II	112	Gg(4) / Hg(4)	[133]
III	180	Hg(7)	[142]

5.11 Summary

To summarize, the experimental results based on EBJIHs unambiguously demonstrate the direct relationship between charge transmission characteristics and the thermoelectric properties of molecular junctions. Further, the experimental techniques developed here show for the first time that it is indeed possible to establish large temperature differentials across molecular junctions while actively tuning their thermoelectric properties. This represents a much needed technical advancement that provides a rational approach for systematically evaluating intriguing computational predictions [6, 33, 120], which suggest that thermoelectric energy conversion can be accomplished—at the Carnot (high efficiency) or the Curzon-Ahlborn limits (high power)—in the junctions whose charge transmission characteristics are appropriately tuned.

Acknowledgements: I nanofabricated EBJIHs in collaboration with Youngsang Kim and with inputs from Kyeongtae Kim. I performed thermopower gating and other electrical measurements along with Youngsang Kim. Kyeongtae Kim and Woochul Lee performed the scanning thermal imaging. I performed the thermal modeling.

Chapter 6

Future work

6.1 Introduction

The results presented in the previous chapter unambigiously prove the hypothesis of thermopower gating in molecular junctions. It is to be noted that researchers in various fields including nanoelectronics, quantum transport and the multi-disciplinary field of thermoelectrics have working towards developing tools for electrostatically tuning the thermoelectric properties in molecular junctions. However, such efforts have remained unsuccessful due to multiple technical challenges. Therefore, the results described in this thesis that experimentally demonstrate thermopower gating at molecular scale—for the first time ever—are a significant and timely contribution to the community.

Although EBJIHs are a much needed technical advancement, performing statistical experiments in this platform is not practical at all because of the very low yield (<5%) of obtaining desired molecular devices. In order to systematically probe novel thermoelectric phenomena arising in molecular junctions, it would be very useful to develop an alternative/complementary experimental platform that will enable a large number of experiments (100s) in a short time (days) to enable statistical analysis. Here, I will briefly describe a plan of creating a new experimental platform that may enable such measurements. Further, I will also describe important experiments that can be performed using the EBJIH devices to test the feasibility of employing quantum interference effects for achieving enhanced thermoelectric properties.

6.2 Proposal for a new experimental platform

Recently, a research group reported a mechanically controllable break junction (MCBJ) based molecular field effect transistor (FET), which leverages a side-gate scheme [124] as shown in Figure 6.1. Since MCBJs provide an excellent platform for establishing repeatable and very stable molecular junctions, if they can be adapted to perform thermoelectric measurements they may provide a facile approach for statistically meaningful thermoelectric studies in molecular junctions.

In order to adopt MCBJs for molecular thermoelectric studies it is necessary to simultaneously achieve: 1) The capability to establish very large temperature gradients ($>10^9$ K/m) across nanometer-sized separations, 2) a reasonable gate coupling to molecular junctions and 3) excellent junction stability when temperature differentials are modulated. The first requirement is expected to be easily satisfied in a MCBJ based FET as the source and drain electrodes of the device are suspended, thus there is no direct thermal pathway between the electrodes. The challenge for satisfying the second requirement in the nanofabrication aspect is placing the gate electrode in the immediate vicinity (<10 nm) of the source and drain electrodes while it should be not too close (~1 nm) to the extent of accidently trapping molecules. Therefore, it is important to determine the appropriate e-beam doses before starting a batch of nanofabrication. Satisfying the last requirement will be key to conceiving the right device as suspended electrodes are susceptible to the effects of periodic thermal expansion-contraction. Hence, it is needed to find a reasonable level of undercut below the source and drain electrodes, which minimizes the thermal expansion effects as well as simultaneously provides enough stretching of the electrodes to form molecular junctions. As a preliminary check, I have already performed finite element modeling to estimate the displacement resulting from the thermal expansion effects for an MCBJ with a 300 nm undercut (smaller than the

usual undercut in conventional MCBJs, which is 500 nm). The calculations suggest that the displacement is <20 pm/K, which may be acceptable for performing the desired measurements. If this estimate does not deviate much from the real case, the side-gate scheme can be employed to create a novel experimental platform in conjunction with the principles developed in this work (integrated heater, shield).

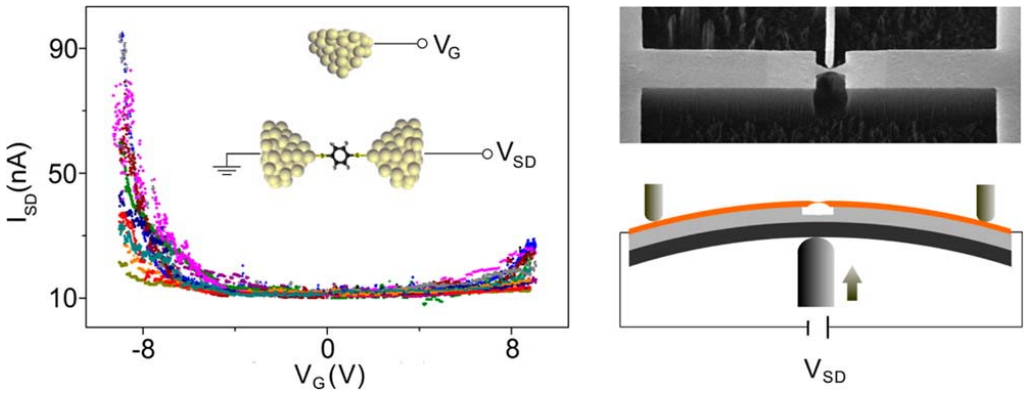

Figure 6.1: MCBJ based FET, which incorporates a side-gate scheme. (Panels reproduced with permission from Ref. 124.)

6.3 Expected observations

As described by the Landauer theory, the Seebeck coefficient of molecular junctions is closely related to the derivative of their charge transmission at the chemical potential E_F (Equation 5.2). It is noticeable that the gating range of the molecular orbitals is limited by the breakdown of dielectric layer (<1 V/nm) between the gate electrode and other electrodes of molecular junctions. Considering a typical gate coupling (in the order of 0.01 eV/V) of three-terminal molecular devices, achieving the shift of the molecular orbitals in the order of 1 eV is very challenging. Therefore, in order to experimentally observe a huge enhancement in the Seebeck coefficient of molecular junctions, it is required to have the molecular junctions whose charge transmission changes abruptly in the vicinity of the chemical potential. A promising approach for achieving such charge

transmission is to employ molecular junctions that feature quantum interference effects [143, 144], which can result in a dip in their charge transmission near E_F as shown in Figure 6.2. If this prediction is indeed realized experimentally, it will be a big first step towards engineering very efficient organic based thermoelectric system.

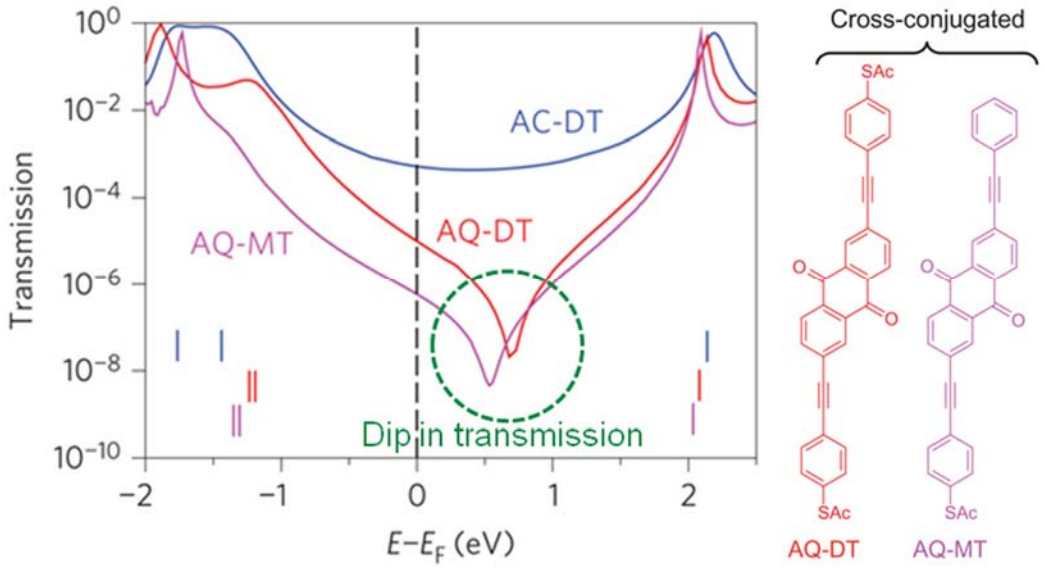

Figure 6.2: Example of molecular junctions having quantum interference effects. Due to a dip in their charge transmission near E_F, it is expected to observe a huge enhancement in the Seebeck coefficient in these molecular junctions. (Panel reproduced with permission from Ref. 143.)

Another attractive observation, which can be studied in the new experimental platform (MCBJ based FET with integrated heater), is the mechanical thermopower gating. This novel phenomena can potentially be observed in helicene based molecular junctions by stretching and/or compressing the junctions because it is predicted that these mechanical effects significantly changes their electrical conductance and Seebeck coefficient. Considering the separations between the source and drain electrodes can be finely controlled in MCBJs, the new experimental platform will be an ideal setup for realizing these novel phenomena.

Appendix A

Precautions in nanofabrication

The nanofabrication process is very delicate. Therefore, if proper precautions are not taken it is not possible to successfully create the desired devices. To facilitate reproduction of the devices described in this work, I provide some suggestions that may be helpful. In my experience following these suggestions is critical to significantly decreasing the failure rate.

1. Plan ahead before you start working in the cleanroom. Five minutes of pre-planning makes a big difference and helps reduce mistakes.
2. Do piranha (1:2 = H_2O_2:H_2SO_4) cleaning after every lift-off or etching step. Nanofabricated devices usually consist of multiple layers, thus the adhesion between layers is very important. Residual photoresist (PR), which can be easily removed by piranha cleaning, is detrimental to the adhesion between layers. Note that a long piranha cleaning can degrade the quality of metal layers, thus a short piranha cleaning (20 – 30 seconds) is preferred.
3. Over-development of PR is preferable to under-development. Although over-development makes the feature size wider, under-development can leave residual PR. As mentioned above, PR residue can frequently be an issue in nanofabrication process. If it is necessary to get an exact feature size, I recommend making the feature size smaller then over-developing PR.
4. Use HMDS and LOR (Lift-off resist) whenever you conduct lift-off. These chemicals ensure a better lift-off result (smoother metal line edge). Of course, it requires much

longer time to prepare for photolithography and is less convenient (e.g. using ACS 200 cluster is not possible), however it is definitely worth adopting these chemicals.

5. If you fail at a step of nanofabrication process, try to find the reason before you restart. Without this, you will most probably fail again due to the same reason.

Appendix B

B.1 Stability of the nanogaps and the frequency dependence of thermoelectric voltages

As described in Chapter 5, all Seebeck coefficient data were obtained under applied modulated temperature differentials. One may suspect that the temperature modulations may result in periodic thermal expansion and contraction of the nanogaps, which may be detrimental to the stability of the junctions and result in measurement artifacts. In order to rule out this concern, the magnitude of the change in gap size was experimentally quantified and it was found to be negligibly small. To establish this fact, vacuum tunnel junctions were first created by electromigration [53] of the devices. For such tunnel junctions the low-bias conductance (G) is given, to an excellent approximation by $G(d) = Ae^{-\beta d}$, where A is a constant, β is the attenuation factor (~1.85 $Å^{-1}$ for vacuum tunnel junctions [145]) and d is the gap size [45, 126, 145]. This implies that if a small DC bias is applied the resulting tunneling current is given by $I_{DC} = G(d)V_{DC}$. Further, under such a bias, if the gap size is modulated sinusoidally (i.e. by the thermal expansion effects) at a frequency $2f$ by an amplitude $\Delta d << d$, a sinusoidal current with an amplitude given by $I_{2f} = [\beta G(d)\Delta d]V_{DC}$ is also set up due to the modulation of the low-bias conductance. From these relationships it can be seen that $I_{2f} / I_{DC} = \beta\Delta d$. Therefore, the modulation in gap size (Δd) can be obtained by measuring I_{DC}, I_{2f} and from knowledge of β. The employed scheme to quantify the effects of applied temperature modulations on the gap size is shown in Figure B.1a. Specifically, small DC biases across the source and drain electrodes were applied while sinusoidally modulating a temperature differential of 1 K at

a frequency $2f$ (10 Hz) across the nanogap. The measured values of I_{DC} and I_{2f} under these conditions are shown in Figure B.1b. As expected and in accordance with the aforementioned relationships, in the small bias limit both the AC and DC components increase linearly. Further, the fact that I_{2f} increases linearly with the applied biases eliminates the possibility that it is a thermoelectric current arising from the applied temperature differential. From Figure B.1b, it can be seen that $I_{2f} / I_{DC} \sim 0.02$. Therefore, from the relationship ($I_{2f} / I_{DC} = \beta \Delta d$ with $\beta \sim 1.85$ Å^{-1}) it can be seen that Δd is ~1.1 pm. This implies that the change in gap size is ~1.1 pm/K. Note that such displacements are comparable to the amplitude of thermally excited vibrations of Au atoms at 100 K [146]. Under such small gap modulations the low-bias conductance of molecular junctions is extremely stable showing that the electronic structure and the energy levels of the junctions are unaffected.

In order to further confirm that the experimental result is indeed reasonable, the change in gap size was computed using finite element modeling. Specifically, the known geometry of the devices (i.e. thickness and dimensions of the layers) was used in conjunction with known thermal expansion coefficient of the materials of the device to estimate the displacement of the gap size for a 1 nm sized tunnel junction (the expected gap size of molecular junctions). From this modeling, it is found that the gap size changes by ~1.6 pm per Kelvin temperature differential across the nanogap, which is in excellent agreement with the experimental estimate. Therefore, based on the above two independent estimates it is reasonable to conclude that the change in gap size is <8 pm even for the largest temperature differentials (4K) applied in the Seebeck coefficient measurements. Such small changes in gap size are known to negligibly impact the thermoelectric properties of molecular junctions.

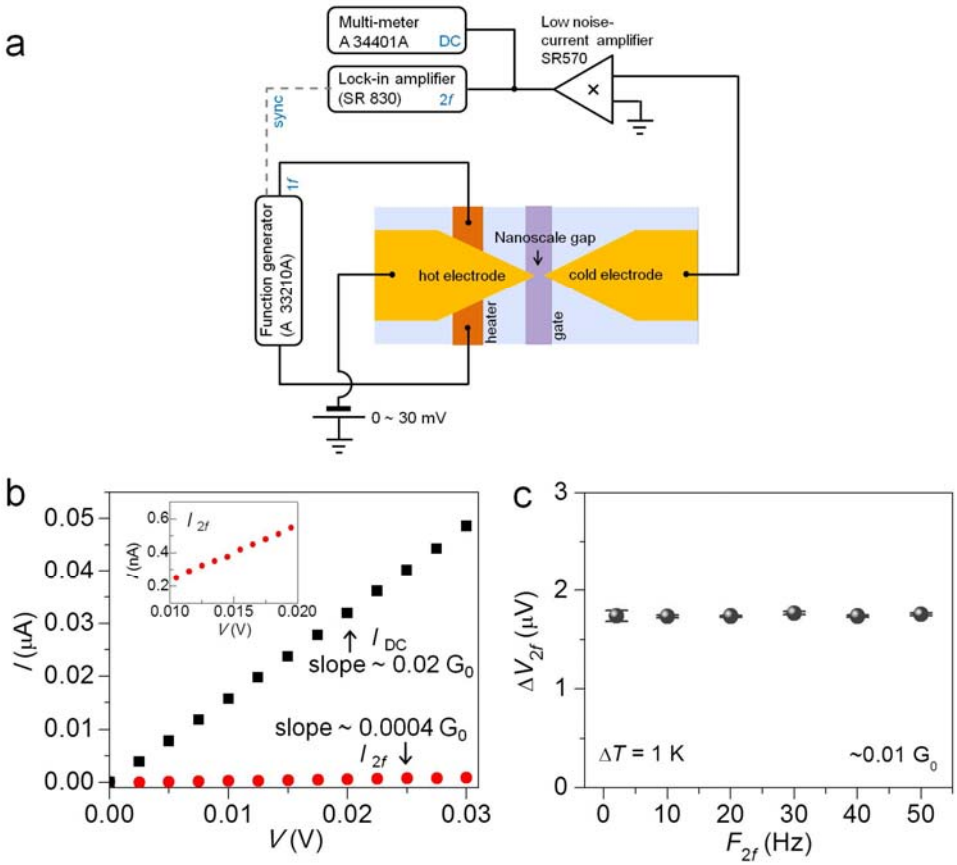

Figure B.1: (a) Schematic of the experimental setup for quantifying the amplitude of thermally induced expansion. (b) DC tunneling current (I_{DC}, black squares) and 2f component of the tunneling current (I_{2f}, red circles) resulting from the modulation of the gap size due to the periodic thermal expansion were measured as a function of the DC bias (V_{DC}) applied to a tunnel junction. The inset shows the magnified view of I_{2f}. It can be seen that I_{2f} is ~2% of I_{DC} indicating that the displacement of the nanogap by the periodic thermal expansion is ~1.1 pm/K. (c) Frequency independent thermoelectric voltages (ΔV_{2f}) of a tunnel gap (G ~0.01 G_0). ΔV_{2f} is independent of the frequency (2f) until 50 Hz. (Panels reproduced from the author's work of Ref. 52.)

In addition, the frequency independence of thermoelectric voltages (ΔV_{2f}) in a tunnel gap was also tested as shown in Fig. B.1c. It can be seen that the measured ΔV_{2f} is indeed independent of the frequency even when the frequency (2f) is raised to 50 Hz, which is 5 times larger than the temperature modulation frequency of the Seebeck coefficient measurements. This result shows that there is indeed no capacitive coupling between higher harmonics of the sinusoidal voltage bias applied to the heater and thermoelectric voltages across the source and drain electrodes.

B.2 Sign determination of the Seebeck coefficient of MJs

Information regarding the sign of the Seebeck coefficient is contained in the phase of thermoelectric voltages measured by a lock-in amplifier (LIA). If thermoelectric voltage measurements are performed by applying unmodulated (DC) temperature differentials, the sign of the Seebeck coefficient of MJs can be easily determined from knowledge of whether the hot electrode is at a higher or lower electrical potential with respect to the cold electrode. However, such a DC measurement scheme suffers from a low signal-to-noise ratio and makes it difficult to perform measurements under small temperature differentials, which are essential to prevent temperature related instabilities in MJs. Whereas, the AC measurement scheme adapted in this work features a high signal-to-noise ratio and makes possible the thermoelectric voltage measurements with small temperature differentials (1 – 4 K). Here, I described how the sign of the Seebeck coefficient of MJs can be extracted by monitoring the phase of thermoelectric voltages. When a sinusoidal current $I = I_0 \sin(\omega t)$ at a frequency $\omega = 2\pi f$ is applied to the heater, the power dissipation is given by:

$$P = I^2 R = I_0^2 R \sin^2(\omega t) = \frac{I_0^2 R}{2}\left[1 - \cos(2\omega t)\right] = \frac{I_0^2 R}{2}\left[1 + \sin(2\omega t - \frac{\pi}{2})\right] \quad \text{(B.1)}$$

This implies that if a sinusoidal reference signal at 2ω is created from the excitation signal such that the nodes of the reference signal are coincident with the alternating nodes of the excitation signal, i.e. if the reference signal is given by (as is generated by the digital signal processor in LIA):

$$I = I_0 \sin(2\omega t) \quad \text{(B.2)}$$

then there is a phase delay of –90° between the internally generated reference signal and the power dissipation of the system. Temperature fields of EBJIHs are proportional to the power dissipation with an additional phase delay (ϕ), which is a small value and reflects

the thermal characteristics of the devices. Thus, the oscillating temperature fields are given by:

$$T(t) = \Delta T_{2f,\,\text{heater}}\left[1+\sin\left(2\omega\,\text{t}-\left(\frac{\pi}{2}+\phi\right)\right)\right] \tag{B.3}$$

where $\Delta T_{2f,\,\text{heater}}$ is the amplitude of temperature oscillations of the heater. It is noticeable that the position dependence of ϕ is very weak for the modulation frequency used in this work, thus there is no measurable phase difference between two neighboring points that are separated by a few nanometers. Therefore, the 2ω component of the temperature amplitude oscillations across the junction is given by:

$$\Delta T_{2f,\,\text{Junc}} = \Delta T_{2f,\,\text{Hot}} - \Delta T_{2f,\,\text{Cold}} = \Delta T_{2f,\,\text{Junc}}\sin\left(2\omega t-\left(\frac{\pi}{2}+\tilde{\phi}\right)\right) \tag{B.4}$$

Finally, thermoelectric voltages are given by:

$$\Delta V_{2f} = -S_{\text{Junc}}\Delta T_{2f,\,\text{Junc}} \tag{B.5}$$

Further, it can be seen that:

$$\left.\begin{aligned}\Delta V_{2f} &= S_{\text{Junc}}\Delta T_{2f,\,\text{Junc}}\sin\left(2\omega t+\left(\frac{\pi}{2}-\tilde{\phi}\right)\right)\ \text{when } S_{\text{Junc}}\ \text{is positive}\\ \Delta V_{2f} &= S_{\text{Junc}}\Delta T_{2f,\,\text{Junc}}\sin\left(2\omega t-\left(\frac{\pi}{2}+\tilde{\phi}\right)\right)\ \text{when } S_{\text{Junc}}\ \text{is negative}\end{aligned}\right\} \tag{B.6}$$

From Equation 5.8 it is clear that if the sign of the Seebeck coefficient changes, then the phase of thermoelectric voltages will change accordingly. Therefore, when the measured phase difference, with respect to the reference signal given by Equation B.2, is ~–90° the Seebeck coefficient is negative, whereas when the measured phase difference is ~+90° the Seebeck coefficient is positive. In addition, this sign determination of the Seebeck coefficient was checked by applying a large DC power to the heater and measuring the DC thermoelectric voltages between the electrodes of MJs using a DC voltmeter and found to be consistent with that obtained from the phase information.

B.3 Effects of the temperature gradients in other parts of the devices on the measured S_{Junc}

The Seebeck coefficient is defined by the following relation,

$$\Delta V = -S\Delta T \tag{B.7}$$

Thus, it can be shown that,

$$\begin{aligned} &V_2 - V_1 = -S_{\text{bk}}(T_2 - T_1),\ V_3 - V_2 = -S_{\text{tk}}(T_3 - T_2), \\ &V_4 - V_3 = -S_{\text{tn}}(T_4 - T_3),\ V_5 - V_4 = -S_{\text{Junc}}(T_5 - T_4), \\ &V_6 - V_5 = -S_{\text{tn}}(T_6 - T_5),\ V_7 - V_6 = -S_{\text{tk}}(T_7 - T_6),\ V_8 - V_7 = -S_{\text{bk}}(T_8 - T_7) \end{aligned} \tag{B.8}$$

where S_{Junc}, S_{bk}, S_{tk} and S_{tn} is the Seebeck coefficient of the molecular junction, bulk Au, ~80 nm and ~15 nm thick Au thin-films respectively, V_x and T_x are the amplitude of voltage oscillations and temperature oscillations at each point (x = 1 – 8 in Figure B.2) respectively. The Seebeck coefficient of two different thin-films is considered separately because it is expected that their Seebeck coefficient is slightly different. It is also noticeable that in EBJIHs the amplitude of temperature oscillations at the locations of 1, 2, 7 and 8 is negligible. After adding the seven equations in B.8,

$$V_8 - V_1 = \left(S_{\text{tk}} - S_{\text{tn}}\right)(T_6 - T_3) + \left(S_{\text{tn}} - S_{\text{Junc}}\right)(T_5 - T_4) \tag{B.9}$$

$$S_{\text{Junc}} = -\frac{V_8 - V_1}{T_5 - T_4} + S_{\text{tn}} + \frac{T_6 - T_3}{T_5 - T_4}\left(S_{\text{tk}} - S_{\text{tn}}\right) \tag{B.10}$$

It can be also shown that,

$$V_8 - V_1 = \Delta V_{2f},\ T_5 - T_4 = \Delta T_{2f,\,\text{Junc}} \text{ and } \frac{T_6 - T_3}{T_5 - T_4} \approx 3 \tag{B.11}$$

The last term in Equation B.11 is ascertained from both the thermal modeling and the UHV-SThM measurements. From Equation B.10 and B.11, it is clear that the Seebeck coefficient of the junction is given by,

$$S_{\text{Junc}} = -\frac{\Delta V_{2f}}{\Delta T_{2f,\,\text{Junc}}} + S_{\text{tk}} + 2\left(S_{\text{tk}} - S_{\text{tn}}\right) \tag{B.12}$$

Therefore, in order to obtain S_{Junc} it is necessary to incorporate the Seebeck coefficient of both ~80 nm and ~15 nm thick Au thin-films (S_{tk} and S_{tn}). It is known that the Seebeck coefficient of bulk Au is ~2 μV/K [147] at room temperature (300 K) and decreases to ~0.8 μV/K [147] at 100 K because the Seebeck coefficient is approximately linearly proportional to the ambient temperature. Further, It is worth noting that the Seebeck coefficient of Au thin-films shows only small deviations from that of bulk Au [148], and the difference of the Seebeck coefficient between ~80 nm and ~15 nm thick Au thin-films is also small [148]. Therefore, the last term of Equation B.12, $S_{\text{tk}} - S_{\text{tn}}$, is equal to zero to a very good approximation. Thus S_{Junc} is given by:

$$S_{\text{Junc}} = -\frac{\Delta V_{2f}}{\Delta T_{2f,\,\text{Junc}}} + S_{\text{tk}} \tag{B.13}$$

where S_{tk} is ~0.8 μV/K [147] and was used in estimating the Seebeck coefficient of molecular junctions in this work.

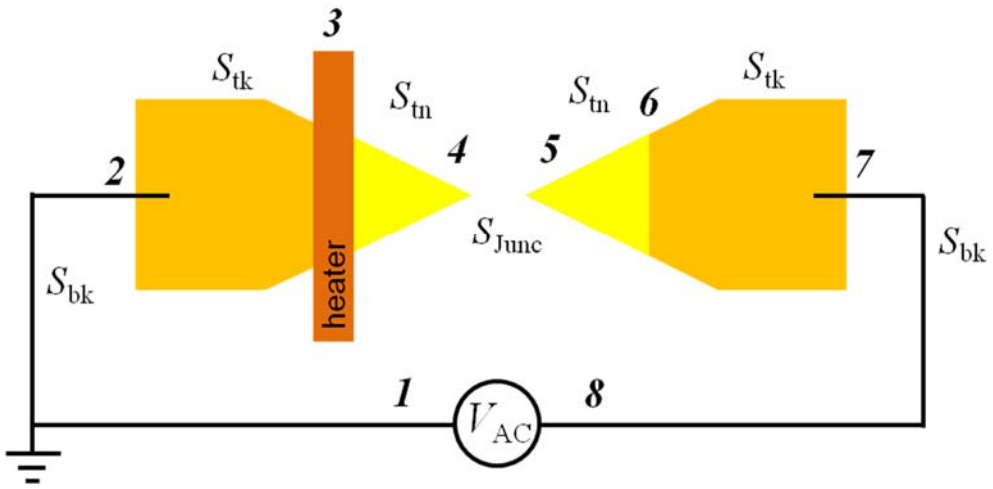

Figure B.2: Schematic diagram labeling the various portions of an EBJIH where temperature differentials are present. The Seebeck coefficient of the various portions of the device is labeled by S_{bk}, S_{tk}, S_{tn} and S_{Junc} and indicates the Seebeck coefficient of bulk Au, ~80 nm and ~15 nm thick Au thin-films and the molecular junction, respectively. (Figure reproduced from the author's work of Ref. 52.)

B.4 Examples of the linear fit of thermoelectric voltages vs. temperature differentials

As described briefly in Chapter 5, the Seebeck coefficient was estimated by first plotting ΔV_{2f} vs. $\Delta T_{2f,\,\mathrm{Junc}}$ and then calculating the Seebeck coefficient from Equation B.13. In Figure B.3, representative plots are shown for Au-BPDT-Au and Au-C_{60}-Au junctions obtained when no gate voltage was applied (V_G = 0 V).

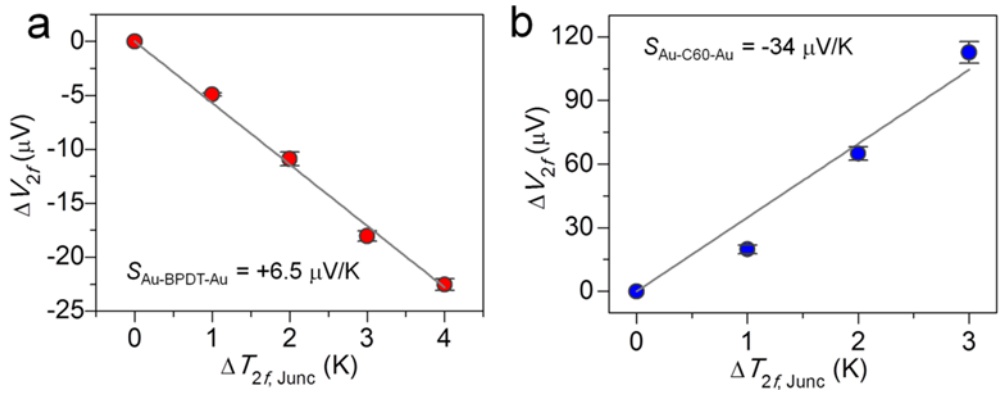

Figure B.3: Representative linear fits of ΔV_{2f} vs. $\Delta T_{2f,\,\mathrm{Junc}}$ used to estimate the Seebeck coefficient of BPDT (a) and C_{60} (b) junctions when V_G = 0 V. These sets of data are identical to the data shown in Figure 5.2b and 5.3b. (Panels reproduced from the author's work of Ref. 52.)

References

[1] Liang, W. J., Shores, M. P., Bockrath, M. *et al.* Kondo resonance in a single-molecule transistor. *Nature* 417, 725-729 (**2002**).

[2] Nitzan, A. & Ratner, M. A. Electron transport in molecular wire junctions. *Science* 300, 1384-1389 (**2003**).

[3] Park, H., Park, J., Lim, A. K. L. *et al.* Nanomechanical oscillations in a single-C_{60} transistor. *Nature* 407, 57-60 (**2000**).

[4] Park, J., Pasupathy, A. N., Goldsmith, J. I. *et al.* Coulomb blockade and the Kondo effect in single-atom transistors. *Nature* 417, 722-725 (**2002**).

[5] Smit, R. H. M., Noat, Y., Untiedt, C. *et al.* Measurement of the conductance of a hydrogen molecule. *Nature* 419, 906-909 (**2002**).

[6] Bergfield, J. P., Solis, M. A. & Stafford, C. A. Giant thermoelectric effect from transmission supernodes. *ACS Nano* 4, 5314-5320 (**2010**).

[7] Bergfield, J. P. & Stafford, C. A. Thermoelectric signatures of coherent transport in single-molecule heterojunctions. *Nano Lett.* 9, 3072-3076 (**2009**).

[8] Paulsson, M. & Datta, S. Thermoelectric effect in molecular electronics. *Phys. Rev. B* 67, 241403(R) (**2003**).

[9] Beebe, J. M., Engelkes, V. B., Miller, L. L. *et al.* Contact resistance in metal-molecule-metal junctions based on aliphatic SAMs: Effects of surface linker and metal work function. *J. Am. Chem. Soc.* 124, 11268-11269 (**2002**).

[10] Reed, M. A., Zhou, C., Muller, C. J. *et al.* Conductance of a molecular junction. *Science* 278, 252-254 (**1997**).

[11] Venkataraman, L., Klare, J. E., Nuckolls, C. *et al.* Dependence of single-molecule junction conductance on molecular conformation. *Nature* 442, 904-907 (**2006**).

[12] Xu, B. Q. & Tao, N. J. J. Measurement of single-molecule resistance by repeated formation of molecular junctions. *Science* 301, 1221-1223 (**2003**).

[13] Reddy, P., Jang, S. Y., Segalman, R. A. *et al.* Thermoelectricity in molecular junctions. *Science* 315, 1568-1571 (**2007**).

[14] Kim, K., Jeong, W., Lee, W. *et al.* Ultra-high vacuum scanning thermal microscopy for nanometer resolution quantitative thermometry. *ACS Nano* 6, 4248-4257 (**2012**).

[15] Hicks, L. D. & Dresselhaus, M. S. Thermoelectric figure of merit of a one-dimensional conductor. *Phys. Rev. B* 47, 16631-16634 (**1993**).

[16] Bejenari, I. & Kantser, V. Thermoelectric properties of bismuth telluride nanowires in the constant relaxation-time approximation. *Phys. Rev. B* 78, 115322 (**2008**).

[17] Boukai, A. I., Bunimovich, Y., Tahir-Kheli, J. *et al.* Silicon nanowires as efficient thermoelectric materials. *Nature* 451, 168-171 (**2008**).

[18] Dresselhaus, M. S., Chen, G., Tang, M. Y. *et al.* New directions for low-dimensional thermoelectric materials. *Adv. Mater.* 19, 1043-1053 (**2007**).

[19] Heremans, J. P., Thrush, C. M., Morelli, D. T. *et al.* Thermoelectric power of bismuth nanocomposites. *Phys. Rev. Lett.* 88, 216801 (**2002**).

[20] Hochbaum, A. I., Chen, R. K., Delgado, R. D. *et al.* Enhanced thermoelectric performance of rough silicon nanowires. *Nature* 451, 163-167 (**2008**).

[21] Martin-Gonzalez, M., Snyder, G. J., Prieto, A. L. *et al.* Direct electrodeposition of highly dense 50 nm $Bi_2Te_{3-y}Se_y$ nanowire arrays. *Nano Lett.* 3, 973-977 (**2003**).

[22] Huang, Y., Duan, X. F., Cui, Y. *et al.* Logic gates and computation from assembled nanowire building blocks. *Science* 294, 1313-1317 (**2001**).

[23] Melosh, N. A., Boukai, A., Diana, F. *et al.* Ultrahigh-density nanowire lattices and circuits. *Science* 300, 112-115 (**2003**).

[24] Postma, H. W. C., Teepen, T., Yao, Z. *et al.* Carbon nanotube single-electron transistors at room temperature. *Science* 293, 76-79 (**2001**).

[25] Xiang, J., Lu, W., Hu, Y. J. *et al.* Ge/Si nanowire heterostructures as high-performance field-effect transistors. *Nature* 441, 489-493 (**2006**).

[26] Duan, X. F., Huang, Y., Agarwal, R. *et al.* Single-nanowire electrically driven lasers. *Nature* 421, 241-245 (**2003**).

[27] Huang, M. H., Mao, S., Feick, H. *et al.* Room-temperature ultraviolet nanowire nanolasers. *Science* 292, 1897-1899 (**2001**).

[28] Huber, C. A., Huber, T. E., Sadoqi, M. *et al.* Nanowire array composites. *Science* 263, 800-802 (**1994**).

[29] Nakayama, Y., Pauzauskie, P. J., Radenovic, A. *et al.* Tunable nanowire nonlinear optical probe. *Nature* 447, 1098-1101 (**2007**).

[30] Qin, Y., Wang, X. D. & Wang, Z. L. Microfibre-nanowire hybrid structure for energy scavenging. *Nature* 451, 809-813 (**2008**).

[31] Tian, B. Z., Zheng, X. L., Kempa, T. J. *et al.* Coaxial silicon nanowires as solar cells and nanoelectronic power sources. *Nature* 449, 885-889 (**2007**).

[32] Yang, R. S., Qin, Y., Dai, L. M. *et al.* Power generation with laterally packaged piezoelectric fine wires. *Nature Nanotech.* 4, 34-39 (**2009**).

[33] Finch, C. M., Garcia-Suarez, V. M. & Lambert, C. J. Giant thermopower and figure of merit in single-molecule devices. *Phys. Rev. B* 79, 033405 (**2009**).

[34] Murphy, P., Mukerjee, S. & Moore, J. Optimal thermoelectric figure of merit of a molecular junction. *Phys. Rev. B* 78, 161406(R) (**2008**).

[35] Majumdar, A. Thermoelectricity in semiconductor nanostructures. *Science* 303, 777-778 (**2004**).

[36] Snyder, G. J. & Toberer, E. S. Complex thermoelectric materials. *Nature Mater.* 7, 105-114 (**2008**).

[37] Harman, T. C., Taylor, P. J., Walsh, M. P. *et al.* Quantum dot superlattice thermoelectric materials and devices. *Science* 297, 2229-2232 (**2002**).

[38] Heremans, J. P., Jovovic, V., Toberer, E. S. *et al.* Enhancement of thermoelectric efficiency in PbTe by distortion of the electronic density of states. *Science* 321, 554-557 (**2008**).

[39] Hsu, K. F., Loo, S., Guo, F. *et al.* Cubic $AgPb_mSbTe_{2+m}$: Bulk thermoelectric materials with high figure of merit. *Science* 303, 818-821 (**2004**).

[40] Poudel, B., Hao, Q., Ma, Y. *et al.* High-thermoelectric performance of nanostructured bismuth antimony telluride bulk alloys. *Science* 320, 634-638 (**2008**).

[41] Mahan, G. D. & Sofo, J. O. The best thermoelectric. *Proc. Natl. Acad. Sci. USA* 93, 7436-7439 (**1996**).

[42] Humphrey, T. E. & Linke, H. Reversible thermoelectric nanomaterials. *Phys. Rev. Lett.* 94, 096601 (**2005**).

[43] Hicks, L. D. & Dresselhaus, M. S. Effect of quantum-well structures on the thermoelectric figure of merit. *Phys. Rev. B* 47, 12727-12731 (**1993**).

[44] Wang, R. Y., Segalman, R. A. & Majumdar, A. Room temperature thermal conductance of alkanedithiol self-assembled monolayers. *Appl. Phys. Lett.* 89, 173113 (**2006**).

[45] Choi, S. H., Kim, B. & Frisbie, C. D. Electrical resistance of long conjugated molecular wires. *Science* 320, 1482-1486 (**2008**).

[46] Jang, S. Y., Reddy, P., Majumdar, A. *et al.* Interpretation of stochastic events in single molecule conductance measurements. *Nano Lett.* 6, 2362-2367 (**2006**).

[47] Kim, Y., Hellmuth, T. J., Sysoiev, D. *et al.* Charge transport characteristics of diarylethene photoswitching single-molecule junctions. *Nano Lett.* 12, 3736-3742 (**2012**).

[48] Park, H., Lim, A. K. L., Alivisatos, A. P. *et al.* Fabrication of metallic electrodes with nanometer separation by electromigration. *Appl. Phys. Lett.* 75, 301-303 (**1999**).

[49] Pasupathy, A. N., Bialczak, R. C., Martinek, J. *et al.* The Kondo effect in the presence of ferromagnetism. *Science* 306, 86-89 (**2004**).

[50] Yu, L. H. & Natelson, D. The Kondo effect in C_{60} single-molecule transistors. *Nano Lett.* 4, 79-83 (**2004**).

[51] Song, H., Kim, Y., Jang, Y. H. *et al.* Observation of molecular orbital gating. *Nature* 462, 1039-1043 (**2009**).

[52] Kim, Y., Jeong, W., Kim, K. *et al.* Electrostatic control of thermoelectricity in molecular junctions. *Nature Nanotech.* (**2014**).

[53] Jeong, W., Kim, K., Kim, Y. *et al.* Characterization of nanoscale temperature fields during electromigration of nanowires. *Sci. Rep.* 4, 4975 (**2014**).

[54] Lee, W., Kim, K., Jeong, W. *et al.* Heat dissipation in atomic-scale junctions. *Nature* 498, 209-212 (**2013**).

[55] Majumdar, A. Scanning thermal microscopy. *Annu. Rev. Mater. Sci.* 29, 505-585 (**1999**).

[56] Luo, K., Herrick, R. W., Majumdar, A. *et al.* Scanning thermal microscopy of a vertical-cavity surface-emitting laser. *Appl. Phys. Lett.* 71, 1604-1606 (**1997**).

[57] Grosse, K. L., Bae, M. H., Lian, F. F. *et al.* Nanoscale Joule heating, Peltier cooling and current crowding at graphene-metal contacts. *Nature Nanotech.* 6, 287-290 (**2011**).

[58] Jo, I., Hsu, I. K., Lee, Y. J. *et al.* Low-frequency acoustic phonon temperature distribution in electrically biased graphene. *Nano Lett.* 11, 85-90 (**2011**).

[59] Kim, P., Shi, L., Majumdar, A. *et al.* Mesoscopic thermal transport and energy dissipation in carbon nanotubes. *Physica B* 323, 67-70 (**2002**).

[60] Shi, L., Plyasunov, S., Bachtold, A. *et al.* Scanning thermal microscopy of carbon nanotubes using batch-fabricated probes. *Appl. Phys. Lett.* 77, 4295-4297 (**2000**).

[61] Weaver, J. M. R., Walpita, L. M. & Wickramasinghe, H. K. Optical-absorption microscopy and spectroscopy with nanometer resolution. *Nature* 342, 783-785 (**1989**).

[62] Shi, L., Zhou, J. H., Kim, P. *et al.* Thermal probing of energy dissipation in current-carrying carbon nanotubes. *J. Appl. Phys.* 105, 104306 (**2009**).

[63] Christofferson, J. & Shakouri, A. Thermoreflectance based thermal microscope. *Rev. Sci. Instrum.* 76, 024903 (**2005**).

[64] Williams, C. C. & Wickramasinghe, H. K. Scanning thermal profiler. *Appl. Phys. Lett.* 49, 1587-1589 (**1986**).

[65] Kim, K., Chung, J., Hwang, G. *et al.* Quantitative measurement with scanning thermal microscope by preventing the distortion due to the heat transfer through the air. *ACS Nano* 5, 8700-8709 (**2011**).

[66] Sadat, S., Tan, A., Chua, Y. J. *et al.* Nanoscale thermometry using point contact thermocouples. *Nano Lett.* 10, 2613-2617 (**2010**).

[67] Shi, L. & Majumdar, A. Thermal transport mechanisms at nanoscale point contacts. *ASME J. Heat Transfer* 124, 329-337 (**2002**).

[68] Khan, A., Philip, J. & Hess, P. Young's modulus of silicon nitride used in scanning force microscope cantilevers. *J. Appl. Phys.* 95, 1667-1672 (**2004**).

[69] Lide, D. R. & Haynes, W. M. *CRC handbook of chemistry and physics*. 90th edn, (CRC Press, **2009**).

[70] Florin, E. L., Rief, M., Lehmann, H. *et al.* Sensing specific molecular-interactions with the atomic-force microscope. *Biosens. Bioelectron.* 10, 895-901 (**1995**).

[71] Hutter, J. L. & Bechhoefer, J. Calibration of atomic-force microscope tips. *Rev. Sci. Instrum.* 64, 1868-1873 (**1993**).

[72] Feynman, R. P., Leighton, R. B., Sands, M. L. *et al. The Feynman lectures on physics*. Definitive and extended edn, (Pearson/Addison-Wesley, **2006**).

[73] Groner, M. D., Fabreguette, F. H., Elam, J. W. *et al.* Low-temperature Al_2O_3 atomic layer deposition. *Chem. Mater.* 16, 639-645 (**2004**).

[74] Lee, S. M., Cahill, D. G. & Allen, T. H. Thermal-conductivity of sputtered oxide-films. *Phys. Rev. B* 52, 253-257 (**1995**).

[75] Meyer, G. & Amer, N. M. Novel optical approach to atomic force microscopy. *Appl. Phys. Lett.* 53, 1045-1047 (**1988**).

[76] Kim, K., Chung, J., Won, J. *et al.* Quantitative scanning thermal microscopy using double scan technique. *Appl. Phys. Lett.* 93, 203115 (**2008**).

[77] Roh, H. H., Lee, J. S., Kim, D. L. *et al.* Novel nanoscale thermal property imaging technique: The 2 omega method. I. Principle and the 2 omega signal measurement. *J. Vac. Sci. Technol. B* 24, 2398-2404 (**2006**).

[78] Roh, H. H., Lee, J. S., Kim, D. L. *et al.* Novel nanoscale thermal property imaging technique: The 2 omega method. II. Demonstration and comparison. *J. Vac. Sci. Technol. B* 24, 2405-2411 (**2006**).

[79] Sultan, R., Avery, A. D., Stiehl, G. *et al.* Thermal conductivity of micromachined low-stress silicon-nitride beams from 77 to 325 K. *J. Appl. Phys.* 105, 043501 (**2009**).

[80] Bergman, T. L. & Incropera, F. P. *Fundamentals of heat and mass transfer*. 7th edn, (John Wiley, **2011**).

[81] Zhang, X., Xie, H. Q., Fujii, M. *et al.* Thermal and electrical conductivity of a suspended platinum nanofilm. *Appl. Phys. Lett.* 86, 171912 (**2005**).

[82] Costa, P. M. F. J., Gautam, U. K., Bando, Y. *et al.* Direct imaging of Joule heating dynamics and temperature profiling inside a carbon nanotube interconnect. *Nature Commun.* 2, 421 (**2011**).

[83] Seol, J. H., Jo, I., Moore, A. L. *et al.* Two-dimensional phonon transport in supported graphene. *Science* 328, 213-216 (**2010**).

[84] Tao, C. G., Cullen, W. G. & Williams, E. D. Visualizing the electron scattering force in nanostructures. *Science* 328, 736-740 (**2010**).

[85] Nam, S. W., Chung, H. S., Lo, Y. C. *et al.* Electrical wind force-driven and dislocation-templated amorphization in phase-change nanowires. *Science* 336, 1561-1566 (**2012**).

[86] Strachan, D. R., Johnston, D. E., Guiton, B. S. *et al.* Real-time TEM imaging of the formation of crystalline nanoscale gaps. *Phys. Rev. Lett.* 100, 056805 (**2008**).

[87] Esen, G. & Fuhrer, M. S. Temperature control of electromigration to form gold nanogap junctions. *Appl. Phys. Lett.* 87, 263101 (**2005**).

[88] Durkan, C., Schneider, M. A. & Welland, M. E. Analysis of failure mechanisms in electrically stressed Au nanowires. *J. Appl. Phys.* 86, 1280-1286 (**1999**).

[89] Trouwborst, M. L., van der Molen, S. J. & van Wees, B. J. The role of Joule heating in the formation of nanogaps by electromigration. *J. Appl. Phys.* 99, 114316 (**2006**).

[90] Hoffmann, R., Weissenberger, D., Hawecker, J. *et al.* Conductance of gold nanojunctions thinned by electromigration. *Appl. Phys. Lett.* 93, 043118 (**2008**).

[91] Ward, D. R., Halas, N. J. & Natelson, D. Localized heating in nanoscale Pt constrictions measured using blackbody radiation emission. *Appl. Phys. Lett.* 93, 213108 (**2008**).

[92] Heersche, H. B., Lientschnig, G., O'Neill, K. *et al.* In-situ imaging of electromigration-induced nanogap formation by transmission electron microscopy. *Appl. Phys. Lett.* 91, 072107 (**2007**).

[93] Stahlmecke, B., zu Heringdorf, F. J. M., Chelaru, L. I. *et al.* Electromigration in self-organized single-crystalline silver nanowires. *Appl. Phys. Lett.* 88, 053122 (**2006**).

[94] Tu, K. N. Recent advances on electromigration in very-large-scale-integration of interconnects. *J. Appl. Phys.* 94, 5451-5473 (**2003**).

[95] Xiong, F., Liao, A. D., Estrada, D. *et al.* Low-power switching of phase-change materials with carbon nanotube electrodes. *Science* 332, 568-570 (**2011**).

[96] Osorio, E. A., O'Neill, K., Wegewijs, M. *et al.* Electronic excitations of a single molecule contacted in a three-terminal configuration. *Nano Lett.* 7, 3336-3342 (**2007**).

[97] Taychatanapat, T., Bolotin, K. I., Kuemmeth, F. *et al.* Imaging electromigration during the formation of break junctions. *Nano Lett.* 7, 652-656 (**2007**).

[98] Bolotin, K. I., Kuemmeth, F., Pasupathy, A. N. *et al.* From ballistic transport to tunneling in electromigrated ferromagnetic breakjunctions. *Nano Lett.* 6, 123-127 (**2006**).

[99] Ward, D. R., Corley, D. A., Tour, J. M. *et al.* Vibrational and electronic heating in nanoscale junctions. *Nature Nanotech.* 6, 33-38 (**2011**).

[100] Coppens, Z. J., Li, W., Walker, D. G. *et al.* Probing and controlling photothermal heat generation in plasmonic nanostructures. *Nano Lett.* 13, 1023-1028 (**2013**).

[101] Strachan, D. R., Smith, D. E., Johnston, D. E. *et al.* Controlled fabrication of nanogaps in ambient environment for molecular electronics. *Appl. Phys. Lett.* 86, 043109 (**2005**).

[102] Ashcroft, N. W. & Mermin, N. D. *Solid state physics*. (Brooks/Cole, **1976**).

[103] Zhang, Q. G., Zhang, X., Cao, B. Y. *et al.* Influence of grain boundary scattering on the electrical properties of platinum nanofilms. *Appl. Phys. Lett.* 89, 114102 (**2006**).

[104] Stoffler, D., Fostner, S., Grutter, P. *et al.* Scanning probe microscopy imaging of metallic nanocontacts. *Phys. Rev. B* 85, 033404 (**2012**).

[105] Chen, G. & Hui, P. Thermal conductivities of evaporated gold films on silicon and glass. *Appl. Phys. Lett.* 74, 2942-2944 (**1999**).

[106] Korhonen, M. A., Borgesen, P., Tu, K. N. *et al.* Stress evolution due to electromigration in confined metal lines. *J. Appl. Phys.* 73, 3790-3799 (**1993**).

[107] Kim, Y., Pietsch, T., Erbe, A. *et al.* Benzenedithiol: A broad-range single-channel molecular conductor. *Nano Lett.* 11, 3734-3738 (**2011**).

[108] Kim, Y., Garcia-Lekue, A., Sysoiev, D. *et al.* Charge transport in azobenzene-based single-molecule junctions. *Phys. Rev. Lett.* 109, 226801 (**2012**).

[109] Perrin, M. L., Verzijl, C. J. O., Martin, C. A. *et al.* Large tunable image-charge effects in single-molecule junctions. *Nature Nanotech.* 8, 282-287 (**2013**).

[110] Prins, F., Barreiro, A., Ruitenberg, J. W. *et al.* Room-temperature gating of molecular junctions using few-layer graphene nanogap electrodes. *Nano Lett.* 11, 4607-4611 (**2011**).

[111] Cuevas, J. C. & Scheer, E. *Molecular electronics*. (World Scientific Pub. Co., **2010**).

[112] Bergfield, J. P., Solomon, G. C., Stafford, C. A. *et al.* Novel quantum interference effects in transport through molecular radicals. *Nano Lett.* 11, 2759-2764 (**2011**).

[113] Widawsky, J. R., Darancet, P., Neaton, J. B. *et al.* Simultaneous determination of conductance and thermopower of single molecule junctions. *Nano Lett.* 12, 354-358 (**2012**).

[114] Evangeli, C., Gillemot, K., Leary, E. *et al.* Engineering the thermopower of C_{60} molecular junctions. *Nano Lett.* 13, 2141-2145 (**2013**).

[115] Guo, S. Y., Zhou, G. & Tao, N. J. Single molecule conductance, thermopower, and transition voltage. *Nano Lett.* 13, 4326-4332 (**2013**).

[116] Tan, A., Sadat, S. & Reddy, P. Measurement of thermopower and current-voltage characteristics of molecular junctions to identify orbital alignment. *Appl. Phys. Lett.* 96, 013110 (**2010**).

[117] Baheti, K., Malen, J. A., Doak, P. *et al.* Probing the chemistry of molecular heterojunctions using thermoelectricity. *Nano Lett.* 8, 715-719 (**2008**).

[118] Tan, A., Balachandran, J., Sadat, S. *et al.* Effect of length and contact chemistry on the electronic structure and thermoelectric properties of molecular junctions. *J. Am. Chem. Soc.* 133, 8838-8841 (**2011**).

[119] Ke, S. H., Yang, M., Curtarolo, S. *et al.* Thermopower of molecular junctions: An ab initio study. *Nano Lett.* 9, 1011-1014 (**2009**).

[120] Karlstrom, O., Linke, H., Karlstrom, G. *et al.* Increasing thermoelectric performance using coherent transport. *Phys. Rev. B* 84, 113415 (**2011**).

[121] Burkle, M., Viljas, J. K., Vonlanthen, D. *et al.* Conduction mechanisms in biphenyl dithiol single-molecule junctions. *Phys. Rev. B* 85, 075417 (**2012**).

[122] Bilan, S., Zotti, L. A., Pauly, F. *et al.* Theoretical study of the charge transport through C_{60}-based single-molecule junctions. *Phys. Rev. B* 85, 205403 (**2012**).

[123] Ulstrup, S., Frederiksen, T. & Brandbyge, M. Nonequilibrium electron-vibration coupling and conductance fluctuations in a C_{60} junction. *Phys. Rev. B* 86, 245417 (**2012**).

[124] Xiang, D., Jeong, H., Kim, D. *et al.* Three-terminal single-molecule junctions formed by mechanically controllable break junctions with side gating. *Nano Lett.* 13, 2809-2813 (**2013**).

[125] Tan, A., Balachandran, J., Dunietz, B. D. *et al.* Length dependence of frontier orbital alignment in aromatic molecular junctions. *Appl. Phys. Lett.* 101, 243107 (**2012**).

[126] Song, H., Kim, Y., Jeong, H. *et al.* Intrinsic charge transport of conjugated organic molecules in electromigrated nanogap junctions. *J. Appl. Phys.* 109, 102419 (**2011**).

[127] Lee, S. M. & Cahill, D. G. Heat transport in thin dielectric films. *J. Appl. Phys.* 81, 2590-2595 (**1997**).

[128] Yoshida, K., Hamada, I., Sakata, S. *et al.* Gate-tunable large negative tunnel magnetoresistance in Ni-C_{60}-Ni single molecule transistors. *Nano Lett.* 13, 481-485 (**2013**).

[129] Osorio, E. A., O'Neill, K., Stuhr-Hansen, N. *et al.* Addition energies and vibrational fine structure measured in electromigrated single-molecule junctions based on an oligophenylenevinylene derivative. *Adv. Mater.* 19, 281-285 (**2007**).

[130] Dell, E. J., Capozzi, B., DuBay, K. H. *et al.* Impact of molecular symmetry on single-molecule conductance. *J. Am. Chem. Soc.* 135, 11724-11727 (**2013**).

[131] Malen, J. A., Doak, P., Baheti, K. *et al.* Identifying the length dependence of orbital alignment and contact coupling in molecular heterojunctions. *Nano Lett.* 9, 1164-1169 (**2009**).

[132] Malen, J. A., Doak, P., Baheti, K. *et al.* The nature of transport variations in molecular heterojunction electronics. *Nano Lett.* 9, 3406-3412 (**2009**).

[133] Bohler, T., Edtbauer, A. & Scheer, E. Conductance of individual C_{60} molecules measured with controllable gold electrodes. *Phys. Rev. B* 76, 125432 (**2007**).

[134] Zotti, L. A., Kirchner, T., Cuevas, J. C. *et al.* Revealing the role of anchoring groups in the electrical conduction through single-molecule junctions. *Small* 6, 1529-1535 (**2010**).

[135] Capozzi, B., Chen, Q. S., Darancet, P. *et al.* Tunable charge transport in single-molecule junctions via electrolytic gating. *Nano Lett.* 14, 1400-1404 (**2014**).

[136] Bruot, C., Hihath, J. & Tao, N. J. Mechanically controlled molecular orbital alignment in single molecule junctions. *Nature Nanotech.* 7, 35-40 (**2012**).

[137] Tsutsui, M. & Taniguchi, M. Vibrational spectroscopy of single-molecule junctions by direct current measurements. *J. Appl. Phys.* 113, 084301 (**2013**).

[138] Hihath, J., Bruot, C., Nakamura, H. *et al.* Inelastic transport and low-bias rectification in a single-molecule diode. *ACS Nano* 5, 8331-8339 (**2011**).

[139] Kim, Y., Hellmuth, T. J., Burkle, M. *et al.* Characteristics of amine-ended and thiol-ended alkane single-molecule junctions revealed by inelastic electron tunneling spectroscopy. *ACS Nano* 5, 4104-4111 (**2011**).

[140] Taniguchi, M., Tsutsui, M., Yokota, K. *et al.* Inelastic electron tunneling spectroscopy of single-molecule junctions using a mechanically controllable break junction. *Nanotechnology* 20, 434008 (**2009**).

[141] Sergueev, N., Roubtsov, D. & Guo, H. Ab initio analysis of electron-phonon coupling in molecular devices. *Phys. Rev. Lett.* 95, 146803 (**2005**).

[142] Sergueev, N., Demkov, A. A. & Guo, H. Inelastic resonant tunneling in C_{60} molecular junctions. *Phys. Rev. B* 75, 233418 (**2007**).

[143] Guedon, C. M., Valkenier, H., Markussen, T. *et al.* Observation of quantum interference in molecular charge transport. *Nature Nanotech.* 7, 304-308 (**2012**).

[144] Xia, J. L., Capozzi, B., Wei, S. J. *et al.* Breakdown of interference rules in azulene, a nonalternant hydrocarbon. *Nano Lett.* 14, 2941-2945 (**2014**).

[145] Ward, D. R., Huser, F., Pauly, F. *et al.* Optical rectification and field enhancement in a plasmonic nanogap. *Nature Nanotech.* 5, 732-736 (**2010**).

[146] Fitzsimmons, M. R., Burkel, E. & Sass, S. L. Experimental measurement of the thermal displacive properties of a large-angle twist grain boundary in gold. *Phys. Rev. Lett.* 61, 2237-2240 (**1988**).

[147] Rowe, D. M. *CRC handbook of thermoelectrics*. (CRC Press, **1995**).

[148] Lin, S. F. & Leonard, W. F. Thermoelectric power of thin gold films. *J. Appl. Phys.* 42, 3634-3639 (**1971**).